The Astrophysical Journal, 912:159 (33pp), 2021 May 10 https://doi.org/10.3847/1538-4357/abee1e

Does the Magnetic Field Suppress Fragmentation in Massive Dense Cores?

Aina Palau[1], Qizhou Zhang[2], Josep M. Girart[3,4], Junhao Liu[2,5,6], Ramprasad Rao[2], Patrick M. Koch[7], Robert Estalella[8], Huei-Ru Vivien Chen[9], Hauyu Baobab Liu[7], Keping Qiu[5,6], Zhi-Yun Li[10], Luis A. Zapata[1], Sylvain Bontemps[11], Paul T. P. Ho[7], Henrik Beuther[12], Tao-Chung Ching[7], Hiroko Shinnaga[13], and Aida Ahmadi[14]
[1] Instituto de Radioastronomía y Astrofísica, Universidad Nacional Autónoma de México, P.O. Box 3-72, 58090, Morelia, Michoacán, Mexico
a.palau@irya.unam.mx
[2] Center for Astrophysics | Harvard & Smithsonian, 60 Garden Street, Cambridge, MA 02138, USA
[3] Institut de Ciències de l'Espai (CSIC-IEEC), Campus UAB, Carrer de Can Magrans S/N, E-08193 Cerdanyola del Vallès, Catalonia, Spain
[4] Institut d'Estudis Espacials de Catalunya, E-08030 Barcelona, Catalonia, Spain
[5] School of Astronomy and Space Science, Nanjing University, 163 Xianlin Avenue, Nanjing 210023, People's Republic of China
[6] Key Laboratory of Modern Astronomy and Astrophysics (Nanjing University), Ministry of Education, Nanjing 210023, People's Republic of China
[7] Institute of Astronomy and Astrophysics, Academia Sinica, No.1, Sec. 4, Roosevelt Road, Taipei 10617, Taiwan
[8] Departament de Física Quántica i Astrofísica, Institut de Ciències del Cosmos, Universitat de Barcelona, (IEEC-UB) Martí i Franquès, 1, E-08028 Barcelona, Spain
[9] Institute of Astronomy and Department of Physics, National Tsing Hua University, Hsinchu 30013, Taiwan
[10] Astronomy Department, University of Virginia, Charlottesville, VA 22904, USA
[11] Université de Bordeaux, Laboratoire d'Astrophysique de Bordeaux, CNRS/INSU, UMR 5804, BP 89, F-33271 Floirac Cedex, France
[12] Max Planck Institute for Astronomy, Königstuhl 17, D-69117 Heidelberg, Germany
[13] Department of Physics and Astronomy, Graduate School of Science and Engineering, Kagoshima University, Amanogawa Galaxy Astronomy Research Center, 1-21-35 Korimoto, Kagoshima 890-0065, Japan
[14] Leiden Observatory, Leiden University, P.O. Box 9513, 2300 RA Leiden, The Netherlands
Received 2020 June 9; revised 2021 January 23; accepted 2021 February 26; published 2021 May 17

Abstract

Theoretical and numerical works indicate that a strong magnetic field should suppress fragmentation in dense cores. However, this has never been tested observationally in a relatively large sample of fragmenting massive dense cores. Here, we use the polarization data obtained in the Submillimeter Array Legacy Survey of Zhang et al. to build a sample of 18 massive dense cores where both fragmentation and magnetic field properties are studied in a uniform way. We measured the fragmentation level, $N_{\rm mm}$, within the field of view common to all regions of $\sim$0.15 pc, with a mass sensitivity of $\sim$0.5 $M_\odot$, and a spatial resolution of $\sim$1000 au. In order to obtain the magnetic field strength using the Davis–Chandrasekhar–Fermi method, we estimated the dispersion of the polarization position angles, the velocity dispersion of the $H^{13}CO^+$(4–3) gas, and the density of each core, all averaged within 0.15 pc. A strong correlation is found between $N_{\rm mm}$ and the average density of the parental core, although with significant scatter. When large-scale systematic motions are separated from the velocity dispersion and only the small-scale (turbulent) contribution is taken into account, a tentative correlation is found between $N_{\rm mm}$ and the mass-to-flux ratio, as suggested by numerical and theoretical works.

Unified Astronomy Thesaurus concepts: Young star clusters (1833); Star formation (1569); Interstellar magnetic fields (845)

1. Introduction

How stellar clusters form and what determines their number of objects and stellar densities are long-standing questions, intimately related to the fragmentation properties of molecular clouds. It is thought that a number of properties of molecular clouds could influence and determine how clouds fragment. First, their density and temperature structures determine the balance between thermal support and gravity required for pure thermal Jeans fragmentation (e.g., Myhill & Kaula 1992; Burkert et al. 1997; Girichidis et al. 2011). There are a number of additional properties, however, which could play a crucial role as well. The most important ones are the properties of turbulence (solenoidal/compressive and Mach number; e.g., Vázquez-Semadeni et al. 1996; Padoan & Nordlund 2002; Schmeja & Klessen 2004; Federrath et al. 2008; Girichidis et al. 2011; Keto et al. 2020), stellar feedback (e.g., Myers et al. 2013; Cunningham et al. 2018), initial angular momentum (e.g., Boss & Bodenheimer 1979; Boss 1999; Hennebelle et al. 2004; Machida et al. 2005; Chen et al. 2012b, 2019; Forgan & Rice 2012), and magnetic fields.

A number of theoretical and numerical studies suggest that magnetic fields could be a key ingredient in the fragmentation process of molecular clouds because it is a form of support against gravitational contraction (e.g., Boss 2004; Vázquez-Semadeni et al. 2005, 2011; Ziegler 2005; Price & Bate 2007; Commerçon et al. 2011; Peters et al. 2011; Bailey & Basu 2012; Boss & Keiser 2013, 2014; Myers et al. 2013; Girichidis et al. 2018; Hennebelle & Inutsuka 2019). Therefore, it is expected that those cores with stronger magnetic fields should present a smaller degree of fragmentation, along with fragment masses larger than the pure thermal Jeans mass, compared to cores with weaker magnetic fields. This should hold at least for cores with similar densities and turbulence.

Massive dense cores are excellent targets to study the formation of stellar clusters. These are dense cores embedded within molecular clumps, with large masses ($\gtrsim$50 $M_\odot$) and typical sizes of 0.1–0.5 pc, which do not necessarily collapse into one star but can fragment into compact condensations and form a small cluster of stars[15] (Williams et al. 2000; Motte et al. 2007; Bontemps et al. 2010). This makes massive dense cores

[15] Strictly speaking, the entity that will contain the entire cluster should be the molecular clump (with sizes $\sim$1 pc), while probably the massive dense core will contain only the central or most embedded part of the stellar cluster (Zhang et al. 2009, 2015; Csengeri et al. 2011).

excellent candidates to study forming clusters, which are usually associated with intermediate-/high-mass stars. The fragmentation properties in samples of about ∼20 massive dense cores have been studied by a number of authors (e.g., Bontemps et al. 2010; Palau et al. 2014, 2015; Beuther et al. 2018; Fontani et al. 2018; Sanhueza et al. 2019; Svoboda et al. 2019). In these works, relations between the fragmentation level and density structure, turbulence, and initial angular momentum were searched for, but none of these works studied if there is the expected relation between the fragmentation level and the magnetic field strength from an observational point of view.

Observational studies of fragmentation versus magnetic fields are very scarce. Most of the studies approaching this key question are based on a comparison of observations of dust continuum emission to the outputs of magnetohydrodynamical simulations. For example, for the low-mass case, Maury et al. (2010) find that magnetohydrodynamical models agree much better with their observations. And for the intermediate-/high-mass case, Peretto et al. (2007) find difficulties matching the observed masses and number of fragments with the results of hydrodynamical simulations, suggesting that extra support such as protostellar feedback or magnetic fields is at play. This is supported by the more recent works of Palau et al. (2013) and Fontani et al. (2016, 2018), where the number, mass, and spatial distribution of the fragments of particular regions are consistent with simulations of fragmenting cores with different mass-to-flux ratios (Commerçon et al. 2011). However, the extreme fragmentation in the DR21OH core cannot be fully reproduced in these simulations because its measured mass-to-flux ratio is 20 times smaller than the one used in the simulations for the highly fragmenting cores (Girart et al. 2013).

Regarding studies reporting a direct measure of the magnetic field strength compared to fragmentation levels, Santos et al. (2016) present polarimetric data at optical and near-infrared wavelengths toward an infrared dark cloud with different fragmentation levels in two hubs (Busquet et al. 2016), and find no significant differences between the magnetic field at each hub at clump scales, while submillimeter polarization observations at core scales for the same two hubs reveal hints of a stronger magnetic field in the non-fragmenting case (Añez-López et al. 2020a). On the other hand, in the mini-starburst star-forming region W43, very recent Atacama Large Millimeter/submillimeter Array observations show similar magnetic field strengths for cores with different fragmentation levels (Cortes et al. 2019). Also, in the G34.43+00.24 region, the three cores studied by Tang et al. (2019) present different fragmentation levels, but they seem to result from an interplay between gravity, turbulence, and magnetic field, with no clear evidence for a unique role of the magnetic field. In a high-resolution polarimetric imaging study of a massive infrared dark cloud, Liu et al. (2020) find that magnetic fields play a role at the early stages of cluster formation, similar to the conclusion of Pillai et al. (2015). On the other hand, more sensitive recent works show that the magnetic field seems to be dragged by flows of material inflowing toward the hubs of hub–filament systems (e.g., Beuther et al. 2020; Pillai et al. 2020; Wang et al. 2020). However, all of the aforementioned observational works do not perform a uniform study in a relatively large sample of regions but focus only on a single or a handful of regions at most. Galametz et al. (2018) study the submillimeter polarized emission in a sample of 12 low-mass Class 0 protostars and find that the morphology of the magnetic field could be related to the rotational energy and the formation of single or multiple systems, with the magnetic field being aligned along the outflow direction for single sources. Actually, in a subsequent study of a sample of 20 low-mass protostellar cores, Galametz et al. (2020) found a positive correlation between the angular momentum in the envelope and the misalignment between the outflow axis and the magnetic field, indicating that the magnetic field could be regulating some of the processes of low-mass star formation. However, the Galametz works focus on the low-mass regime. Thus, a uniform study of the fragmentation and magnetic field properties in a relatively large sample of massive dense cores is lacking and therefore imperative.

Here we used the submillimeter polarization data of the Submillimeter Array (SMA) Legacy Survey of Zhang et al. (2014), together with regions from the literature with similar observational properties to build a sample of 18 massive dense cores. In Section 2, we describe the sample and observations; in Section 3, we present the continuum, polarization, and $H^{13}CO^+$ data; in Section 4, we analyze the polarization data, determine density profiles for all the sample, measure line widths, and perform the angular dispersion function (ADF) analysis to finally infer magnetic field strengths. In Section 5, a discussion of the results is presented, and in Section 6, our main conclusions are given.

2. The Sample

In Table 1, we present the sample of 18 massive dense cores[16] studied in this work. Among the 18 regions, the 0.87 mm polarization data of 11 were presented in the Submillimeter Array Legacy Survey of Zhang et al. (2014; see also Ching et al. 2017). The 0.87 mm polarization data of the remaining regions were taken from the literature or the SMA archive (see the last column of Table 1). We thus refer to these works for the details of the polarization observations. In general, the typical 1σ rms noise in the Stokes Q and U images is ∼2 mJy beam^{-1}. It is worth noting that we took special care to build a sample as uniformly as possible. Thus, to avoid biases with distance, we restricted our sample to regions in the range 1.4–2.6 kpc, i.e., there is less than a factor of 2 in distance for the sources of our sample. Two of the regions were observed down to similar rms noises as the other regions, but no signal of polarized emission was detected: N53 from Ching et al. (2017) and I20126 from H. Shinnaga et al. (2021, in preparation).

Regarding the continuum images used to assess the fragmentation level, Table 1 provides the properties of the images along with the references. For most of the regions, we used the 0.87 mm continuum emission observed with the SMA using the extended configuration only from Zhang et al. (2014). Only those marked with an asterisk in Table 1 were observed with the Plateau de Bure (PdBI)/NOrthern Extended Millimeter Array (NOEMA) at 1.3 mm. In order to build a uniform sample, we specifically checked to ensure that the *uv* coverage of both the SMA and PdBI/NOEMA are comparable (see

[16] The radii of our core/clumps estimated from the FWHM in the JCMT images is about 0.2–0.4 pc. Thus, they are structures in the transition between cores (∼0.1 pc) and clumps (∼1 pc). Because in this work we focus on the inner parts of these structures of 0.075 pc of radius, the term "core" has been chosen to emphasize that the study is at these scales.

Table 1
Properties of the Observations Used to Assess the Fragmentation Level in the Sample of Massive Dense Cores at 0.87 and 1.3 mm

Source[a] (1)	D (kpc) (2)	L_{bol}[b] ($L_\odot$) (3)	M_{core}[b] ($M_\odot$) (4)	rms[c] (mJy) (5)	M_{min}[c] ($M_\odot$) (6)	uv-range ($k\lambda$) (7)	Spat. Res.[d] (au) (8)	LAS[d] (au) (9)	References[e] (10)
1-W3IRS5	1.95	140000	510	2.4	0.31	22–210	1600	8050	1
2-W3H2O	1.95	36000	540	2.6*	1.22	55–585	682	3230	2,3
3-G192	1.52	2700	40	3.3	0.27	40–260	1070	3460	4,5
4-NGC 6334V	1.30	40000	370	7.0	0.42	25–210	1140	4730	4,6
5-NGC 6334A(IV)	1.30	1000	600	6.6	0.40	25–210	1200	4730	4
6-NGC 6334I	1.30	48000	300	12	0.72	25–210	1130	4730	4
7-NGC 6334In	1.30	1300	730	17	1.03	25–210	1190	4730	4
8-G34.4.0	1.57	2300	150	7.0	0.62	40–260	1110	3570	4
9-G34.4.1	1.57	1100	310	2.0	0.17	40–260	1160	3570	4
10-G35.2N	2.19	15000	1060	1.3	0.22	40–260	1620	4980	4
11-IRAS 20126+4104	1.64	8900	60	0.7*	0.46	48–551	629	3120	7,8
12-CygX-N3(DR17)	1.40	200	400	1.0*	0.26	20–200	1400	6370	9, 10
13-W75N(CygX-N30)	1.40	20000	270	2.6*	0.72	20–160	1650	6370	11
14-DR21OH(CygX-N44)	1.40	10000	490	4.7	0.33	40–260	1050	3150	4, 12
15-CygX-N48(DR21OHS)	1.40	4400	610	1.5*	0.39	20–200	1400	6370	9, 13
16-CygX-N53	1.40	300	240	1.9*	0.49	20–200	1400	6370	9, 13
17-CygX-N63(DR22)	1.40	470	70	3.0*	0.77	20–200	1400	6370	9, 10
18-NGC 7538S	2.65	12000	1120	0.4*	0.43	68–765	848	3520	2, 14

Notes.
[a] Complete name commonly used for each massive dense core. In the following tables and figures, a short version of the name will be used.
[b] L_{bol} is calculated with the flux densities used to build the spectral energy distribution for the model described in Section 4.1. M_{core} is calculated by integrating our modeled density structure for each core (Section 4.1) up to the observed radius with the JCMT.
[c] rms at 870 μm (from SMA observations) for all sources, except for those marked with an asterisk, for which the rms corresponds to the image at ∼1.3 mm (Plateau de Bure and/or NOEMA observations). M_{min}, the mass sensitivity, is taken at 6 times the rms noise of each image (identification threshold), assuming a dust temperature of 20 K and a dust (+gas) mass opacity coefficient at 0.87(1.3) mm of 0.0175(0.00899)cm^2 g^{-1} (column 6 of Table 1 of Ossenkopf & Henning 1994, corresponding to agglomerated dust grains with thin ice mantles at densities of 10^6 cm^{-3}).
[d] Spatial resolution taken from the synthesized beam of each image and the distance to the source. LAS stands for largest angular scale, estimated using the smallest uv distance given in column (7), and following Equation A5 of Palau et al. (2010). This corresponds to the maximum spatial scale the interferometer was able to recover.
[e] References for the continuum emission used to assess the fragmentation level N_{mm} and for the polarization data used to study the polarization angle dispersion: (1) H.-R. V. Chen et al. (2021, in preparation); (2) Beuther et al. (2018) and Ahmadi et al. (2018): this region is part of the CORE Large Project carried out with NOEMA; (3) Chen et al. (2012a); (4) Zhang et al. (2014); (5) Liu et al. (2013); (6) Juárez et al. (2017); (7) Cesaroni et al. (2014); (8) H. Shinnaga et al. (2021, in preparation); (9) Bontemps et al. (2010); (10) SMA archive; (11) F. O. Alves et al. (2021, in preparation); (12) Girart et al. (2013); (13) Ching et al. (2017); (14) Beuther et al. (2012).

column (6) of Table 1). This implied in some cases re-imaging using the visibilities only from the extended configuration. This will ensure not only a similar spatial resolution of ∼1000 au for all the regions but also that the largest angular scale filtered out by the interferometers is similar for all regions (see columns (7), (8) and (9) of Table 1). Finally, special care was also taken regarding the sensitivity, which was required to be around ∼0.5 $M_\odot$ (at 6σ) or better. For this purpose, we self-calibrated some of the regions, with the final rms noises listed also in the table. We note that six of the regions included in the present sample (W3IRS5, I20126, DR21OH, N48, N53, and N63) overlap with the sample of Palau et al. (2014).

3. Results

Figures 1(a) and (b) present the resulting continuum images (with extended configuration only) used to assess the fragmentation level. The fragmentation level is estimated by counting the number of submillimeter sources above a 6σ threshold and within a region of 0.15 pc in diameter, which corresponds to the smallest field of view in our sample (given by the primary beam of the PdBI/NOEMA observations and the distance for each region). Table 2 lists the fragmentation level N_{mm} estimated for each region. As can be seen from the table, the measured fragmentation level ranges from almost no fragmentation (1–2 fragments for G192, I20126, and N63) to highly fragmenting regions (with up to 18 fragments, such as DR21OH). A total number of 160 fragments were identified within the 18 massive dense cores. For each core, the mass and size (at the 3σ level) for each fragment was calculated (see details in Table 2), along with the average mass and size in each core, and their standard deviations. In addition, each massive dense core has been classified according to a "fragmentation type," following Tang et al. (2019): "clustered fragmentation" corresponds to cores with fragments distributed more or less homogeneously within the core (eight regions); "aligned fragmentation" corresponds to cores with fragments predominantly aligned along a particular direction (seven regions); "no fragmentation" corresponds to cores with only one or two fragments (three regions).

In order to ensure that the fragmentation level is not affected by biases with distance, sensitivity, or evolutionary stage, in Figure 13 of Appendix A, we present N_{mm} versus spatial resolution, mass and column density sensitivity, and the evolutionary indicator L_{bol}/M_{core} (Molinari et al. 2016, with L_{bol} being the bolometric luminosity of the massive dense core and M_{core} being its mass estimated from our modeling, see Section 4.1 and Table 1). The figure shows that there are no trends and thus the sample is well suited to compare the fragmentation properties between the different regions.

While the fragmentation level was assessed using only the SMA or PdBI/NOEMA extended configuration, yielding typical

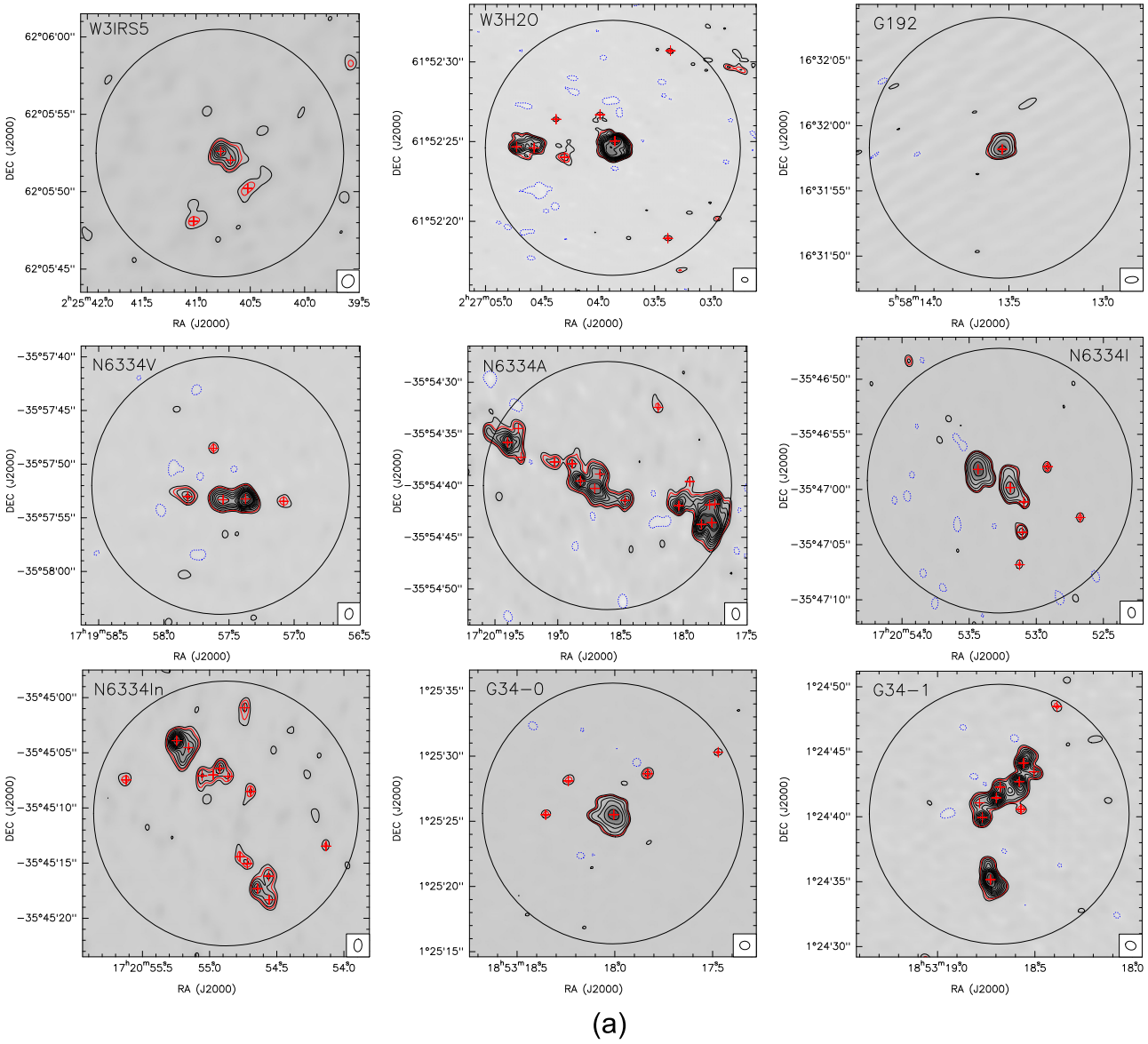

Figure 1. (a) 0.87 or 1.3 mm continuum high-angular-resolution maps. Contours for all regions are −4, 4, 8, 12, 16, 20, 24, 28, 36, 40, 50, 60, 70, 80, 100, and 120 times the rms noise, listed in Table 1, except for G192, N6334I, and G34-0, for which contours are −4, 4, 8, 16, 32, 64, and 128 times the rms noise. Synthesized beams are plotted in the bottom-right corner of each panel, and the black circle corresponds to a field of view of 0.15 pc diameter (the field of view common to all the regions, given their primary beams). In all panels, the red contour corresponds to the identification level of 6σ, and the plus signs correspond to the identified fragments. (b) 0.87 or 1.3 mm continuum high-angular-resolution maps. Contours for all regions are −4, 4, 8, 12, 16, 20, 24, 28, 36, 40, 50, 60, 70, 80, 100, and 120 times the rms noise, listed in Table 1, except for I20126, N63, and N7538S for which contours are −4, 4, 8, 16, 32, (48), 64, and 128 times the rms noise, and for G35, for which contours are −4, 4, 8, 12, 20, 28, 36, 44, 52, 60, 80, 100, 120, 150, and 200 times the rms noise. Synthesized beams are plotted in the bottom-right corner of each panel, and the black circle corresponds to a field of view of 0.15 pc diameter (the field of view common to all the regions, given their primary beams). In all panels, the red contour corresponds to the identification level of 6σ, and the plus signs correspond to the identified fragments.

synthesized beams below 1″ (∼0.″8) and filtering emission typically above ∼3″, the polarized emission was obtained using all available SMA configurations, including compact and/or subcompact configurations, and therefore, only emission about 14″–30″ was filtered out (Zhang et al. 2014). Thus, the polarized emission includes emission at much larger scales compared to the continuum emission used to study the fragmentation.

Figures 2(a) and (b) present the magnetic field segments overplotted on the images of continuum emission used to assess the fragmentation level. From these figures, it is clear that I20126 and N53 do not have enough detections to calculate their magnetic field strength and hence will not be considered further for the analysis of the polarization data.

In Figures 14(a) and (b) of Appendix A, we present the first-order moment of the $H^{13}CO^{+}$(4–3) (346.998344 GHz) transition for each region. The observations of the $H^{13}CO^{+}$(4–3) transition were carried out simultaneously with the submillimeter polarization data from the SMA, with a spectral resolution of 0.7 km s^{-1} for all cases, except for W3H2O and N7538S, for which the spectral resolution is 1.4 km s^{-1}. The images presented in Figures 14(a) and (b) correspond to images built using all SMA available configurations for each region, as for the polarized emission presented in Figures 2(a) and (b) (therefore again including compact and/or subcompact configurations). Figures 14(a) and (b) also show the outflow directions reported in the literature for each massive dense core. In general, velocity

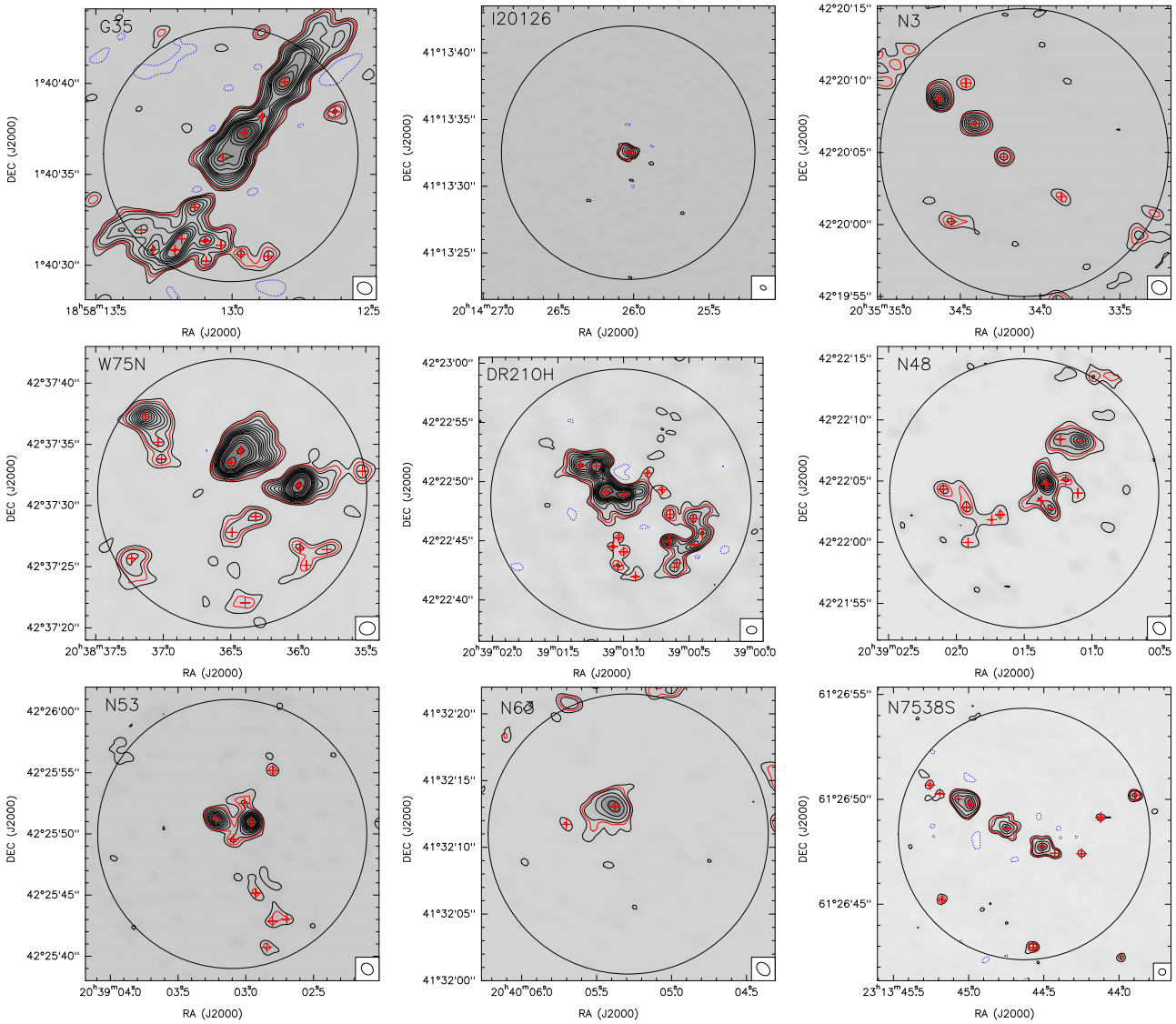

Figure 1. (Continued.)

gradients are present in all regions, indicating that they could have a nonnegligible contribution to the velocity line widths obtained from spectra averaged over the region, required to estimate the magnetic field strength. This is further discussed in Section 4.2.

4. Analysis

4.1. Determination of the Density Structure

In order to estimate the density averaged within 0.15 pc in diameter (the field of view where the fragmentation level was assessed), we inferred the radial density profile of each massive dense core. To do this, we followed the same approach described in Palau et al. (2014), where a model was developed to simultaneously fit the radial intensity profiles at 450 and 850 μm SCUBA images (from the James Clerk Maxwell Telescope) from di Francesco et al. (2008),[17] along with the spectral energy distribution (SED). The constraint imposed by the SED allows the degeneracy between temperature and density to the intensity of the source to be broken. The model assumes spherical symmetry, takes into account opacity effects (i.e., the emission is not assumed to be optically thin), does not assume the Rayleigh–Jeans approximation and considers that the density and temperature decrease with radius following power laws with indices p and q, respectively: $\rho = \rho_0(r/r_0)^{-p}$ and $T = T_0(r/r_0)^{-q}$, with ρ_0 and T_0 being the density and temperature values at a reference radius r_0 taken to be 1000 au. Regarding the dust opacity law, it was assumed to follow a power law of frequency with index β, $\kappa = \kappa_0(\nu/\nu_0)^{\beta}$, where ν_0 is an arbitrary reference frequency. The value of $\kappa_0 = 0.008991$ cm^2 g^{-1} at $\nu_0 = 230$ GHz was adopted (Ossenkopf & Henning 1994). Given a dust cloud heated radiatively by a central luminous source, it has been shown that β and q are related according to $q = 2/(4+\beta)$ (Scoville & Kwan 1976; Adams 1991; Chandler et al. 1998). Thus, there are four final free parameters of the model: the dust emissivity index, β; the envelope temperature at the reference radius r_0, T_0; the

[17] For the cases of N3 and N63, the SCUBA data are not available and the IRAM 30 m data at 1.2 mm from Motte et al. (2007) were used (Palau et al. 2014).

Table 2
Fragmentation Properties of the Massive Dense Cores

Source (1)	N_{mm}[a] (2)	Frag. type[b] (3)	$\langle R_{fragm}\rangle$[c] (au) (4)	$\sigma(R_{fragm})$[c] (au) (5)	$\langle M_{fragm}\rangle$[c] ($M_\odot$) (6)	$\sigma(M_{fragm})$[c] ($M_\odot$) (7)	$\langle n_{frag}\rangle$[c] (10^7 cm^{-3}) (8)	M_{Jeans}[d] ($M_\odot$) (9)	M_{crit}[d] ($M_\odot$) (10)
1-W3IRS5	4	cl	1490	70	0.1	0.1	0.2	1.3–19	0.8
2-W3H2O	8	cl	730	430	2.8	3.9	15	0.8–6.8	0.6
3-G192	1	no	1770	⋯	2.7	⋯	1.8	1.9–5.7	2.7
4-N6334V	5	cl	1310	460	1.1	1.3	1.1	0.9–4.1	1.6
5-N6334A	16	al	1270	370	1.3	1.1	2.0	0.9–2.6	1.0
6-N6334I	7	cl	1070	620	3.8	6.8	3.4	0.7–4.8	3.3
7-N6334In	15	al	1000	200	1.0	1.2	3.1	0.7–2.8	4.4
8-G34-0	5	cl	1090	840	2.9	5.8	3.2	0.9–3.3	1.4
9-G34-1	10	al	1170	440	0.7	1.1	1.0	1.0–2.0	3.4
10-G35	15	al	1820	690	2.8	4.3	0.9	1.0–3.6	3.6
11-I20126	1	no	⋯	⋯	⋯	⋯	⋯	1.4–7.2	⋯
12-N3	6	al	1220	270	0.7	0.7	1.1	1.2–1.4	0.4
13-W75N	14	cl	1980	660	2.1	2.5	0.7	0.9–5.5	3.5
14-DR21OH	18	cl	1250	440	1.2	1.3	1.7	0.6–1.9	1.7
15-N48	12	cl	1320	410	0.7	0.6	0.4	0.8–1.6	0.7
16-N53	9	al	⋯	⋯	⋯	⋯	⋯	0.9–1.1	⋯
17-N63	2	no	1950	1380	7.8	10	2.4	1.4–2.2	1.1
18-N7538S	12	al	1100	440	1.6	1.7	3.3	0.7–2.8	1.3

Notes.
[a] N_{mm} is the fragmentation level, estimated counting the number of millimeter sources above a 6σ threshold, covering at least half a beam at 4σ, and closing at least one contour, within the common field of view for all the regions of 0.15 pc in diameter.
[b] Fragmentation type according to Tang et al. (2019). "cl" corresponds to "clustered fragmentation"; "al" corresponds to "aligned fragmentation"; and "no" corresponds to "no fragmentation" (see Section 3).
[c] $\langle R_{fragm}\rangle$ and $\langle M_{fragm}\rangle$ correspond to the average radius and mass (at the 3σ level), respectively, of all fragments in a given massive dense core. $\sigma(R_{fragm})$ and $\sigma(M_{fragm})$ correspond to the standard deviation of the radius and mass of the fragments in each massive dense core. The mass of the fragments was calculated using the flux density within the 3σ contour, and considering the temperature corresponding to the temperature power-law derived in Section 4.1, using as distance the projected distance measured from the fragment to the peak of the single-dish submillimeter source. The opacity law used is the same as the opacity given in the notes of Table 1. $\langle n_{frag}\rangle$ is the average density of the fragments in each region. For each fragment, its density was calculated as $n_{frag} = M_{frag}/(\frac{4\pi}{3} R_{frag}^3)$.
[d] M_{Jeans} corresponds to the Jeans mass calculated following Equation (15) and using the values of $n_{0.15\ pc}$ listed in Table 3. The range of values corresponds to the range of temperatures assumed, 20 K (lower limit) or $T_{0.15\ pc}$ from Table 3 (upper limit). M_{crit} is the magnetic critical mass (the Jeans mass analog in the magnetic support case) calculated following Equation (16), using $\langle R_{fragm}\rangle$ and the magnetic field strength B_{stdev} (Table 5) scaled in density to the average density of all the fragments, of 3×10^7cm^{-3}, assuming that $B_{frag} = B_{stdev}\left[\frac{3\times10^7\ cm^{-3}}{n_{0.15\ pc}}\right]^{0.4}$ (Li et al. 2015).

envelope density at the reference radius r_0, ρ_0; and the density power-law index, p.

The fitting procedure was the same as the one described in Palau et al. (2014), with initial search ranges for the four parameters being $\beta = 1.5 \pm 1.5$, $T_0 = 300 \pm 300$ K, $\rho_0 = (1.0 \pm 1.0) \times 10^{-16}$ g cm^{-3}, and $p = 1.5 \pm 1.0$. The search range was reduced by a factor of 0.8 around the best-fit value found for each loop. In turn, each loop consisted of 2000 samples of the parameter space, and the final best-fit values were taken after 10 loops. Once the best-fit parameters were found, their uncertainties were estimated through the increase in χ^2. We refer to Palau et al. (2014) for further details of the model and the fitting procedure, and to Appendix C for additional details on the SED building for two particular regions of the sample. In Table 3 we list the best-fit values for the four free parameters of the model, along with the reduced χ^2, the temperature power-law index q, the mass within a region of 0.15 pc in diameter,[18] and the density averaged within the same region. The uncertainties associated with the averaged density and mass are obtained taking into account the uncertainty in the reference density ρ_0, which is about 10%–20% of the fitted value, while the uncertainty in the density power-law index p is always $< 5\%$ (Table 3) and is not considered. Our results for the density power-law index are consistent, within the errors, with very recent estimates at smaller scales (∼2000 au) from the CORE sample (W3H2O; Gieser et al. 2021). In Figures 3(b) and (c), the observational data and the best-fit model for each region are presented.

4.2. Determination of the Velocity Dispersion

One of the common techniques to estimate velocity dispersions is to fit a Gaussian to the line spectrum of the region. We extracted the $H^{13}CO^+$(4–3) spectrum averaged over a region of 0.15 pc in diameter (the field of view where fragmentation was assessed) and fitted one Gaussian for each region of our sample.[19] For the case of N6334I, there is

[18] The mass given in Table 3 is not the total mass of the core, but the mass only within a region of 0.15 pc in diameter. An estimate of the total mass of the core is given in Table 1 and results from integrating the density of our model up to the observed radius for each region as seen with the JCMT. This yields values typically about a factor of 4–10 larger than the mass within 0.15 pc in diameter.

[19] The $H^{13}CO^+$(4–3) spectrum of W3H2O clearly presents two well-separated velocity components. The blueshifted component was found to be very well associated with the polarized emission while the redshifted component was found to be much more extended. For this reason, in this case, two Gaussians had to be fitted and the line width of the blueshifted component was used for our analysis. The first-order moment shown in Figure 14(a) for W3H2O corresponds also to the blueshifted velocity component.

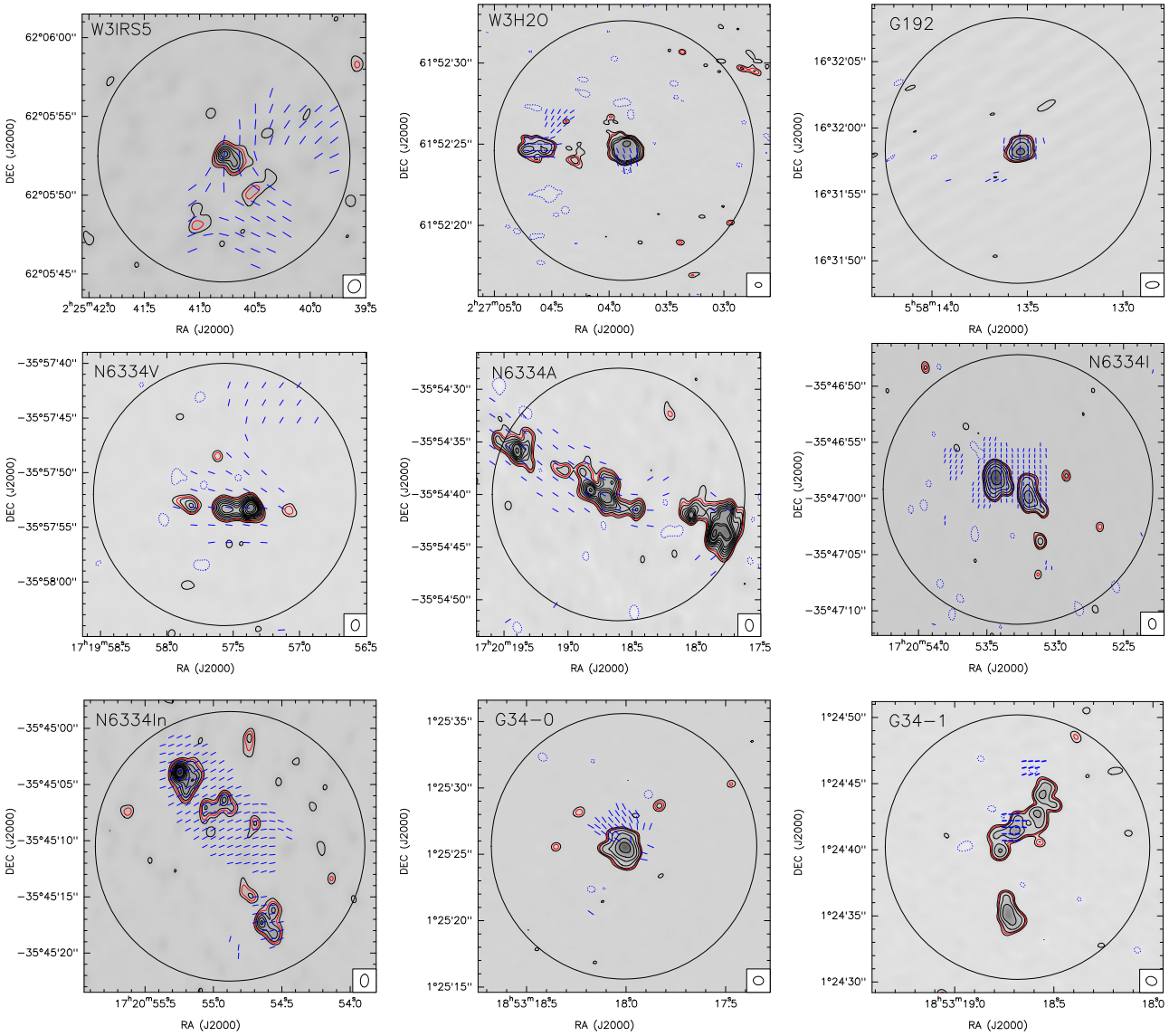

Figure 2. (a) 0.87 or 1.3 mm continuum high-angular-resolution maps with the magnetic field segments overplotted in blue. Contours for all regions are −4, 4, 8, 12, 16, 20, 24, 28, 36, 40, 50, 60, 70, 80, 100, and 120 times the rms noise, listed in Table 1, except for G192, N6334I, G34-0, and G34-1, for which contours are −4, 4, 8, 16, 32, 64, and 128 times the rms noise. For W3H2O, contours are −4, 4, 8, 16, 24, 32, 64, and 120 times the rms noise. Synthesized beams are plotted in the bottom-right corner of each panel, and the black circle corresponds to the common field of view of 0.15 pc diameter. (b) 0.87 or 1.3 mm continuum high-angular-resolution maps with the magnetic field segments overplotted in blue. Contours for all regions are −4, 4, 8, 12, 16, 20, 24, 28, 36, 40, 50, 60, 70, 80, 100, and 120 times the rms noise, listed in Table 1, except for I20126, W75N, N53, N63, and N7538S, for which contours are −4, 4, 8, 16, 32, 64, and 128 times the rms noise, and for G35, for which contours are −4, 4, 8, 12, 20, 28, 36, 44, 52, 60, 80, 100, 120, 150, and 200 times the rms noise. Synthesized beams are plotted in the bottom-right corner of each panel, and the black circle corresponds to the common field of view of 0.15 pc diameter.

absorption toward the two strongest continuum sources and some emission from 5 to 10 km s^{-1} (velocities given with respect to the local standard of rest), but these features are very compact. The main emission is found in the velocity range from −15 to 0 km s^{-1}, and the Gaussian was fitted in this velocity range.

The spectra and the corresponding fits are shown in Figure 4, and the velocity line widths, $\Delta v_{0.15\,\mathrm{pc}}$, are listed in Table 4. As can be seen from the figure, most spectra appear to be well fitted with only one Gaussian.

The velocity dispersion associated with turbulence is estimated assuming that it is a factor Q of the nonthermal dispersion. The nonthermal dispersions, σ_{nonth}, are listed in Table 4 and were calculated by assuming the average temperature reported in Table 3, $T_{0.15\,\mathrm{pc}}$. As can be seen from Table 4, in our case, the nonthermal dispersions are essentially the same as the total velocity dispersions. Thus, we estimate that the 1D (along the line of sight) turbulent dispersion is

$$\sigma_{\mathrm{turb,spec}} = Q\,\Delta\,v_{0.15\,\mathrm{pc}}/\sqrt{8\ln 2}\,, \quad (1)$$

where the subindex "spec" is written to remind that this estimate makes use of the line width inferred from the spectrum. In this equation, we assumed that $Q \sim 0.5$. The Q factor, defined here as $Q \equiv \sigma_{\mathrm{turb}}/\sigma_{\mathrm{nonth}}$, is required to take into account the fact that systematic large-scale motions could be

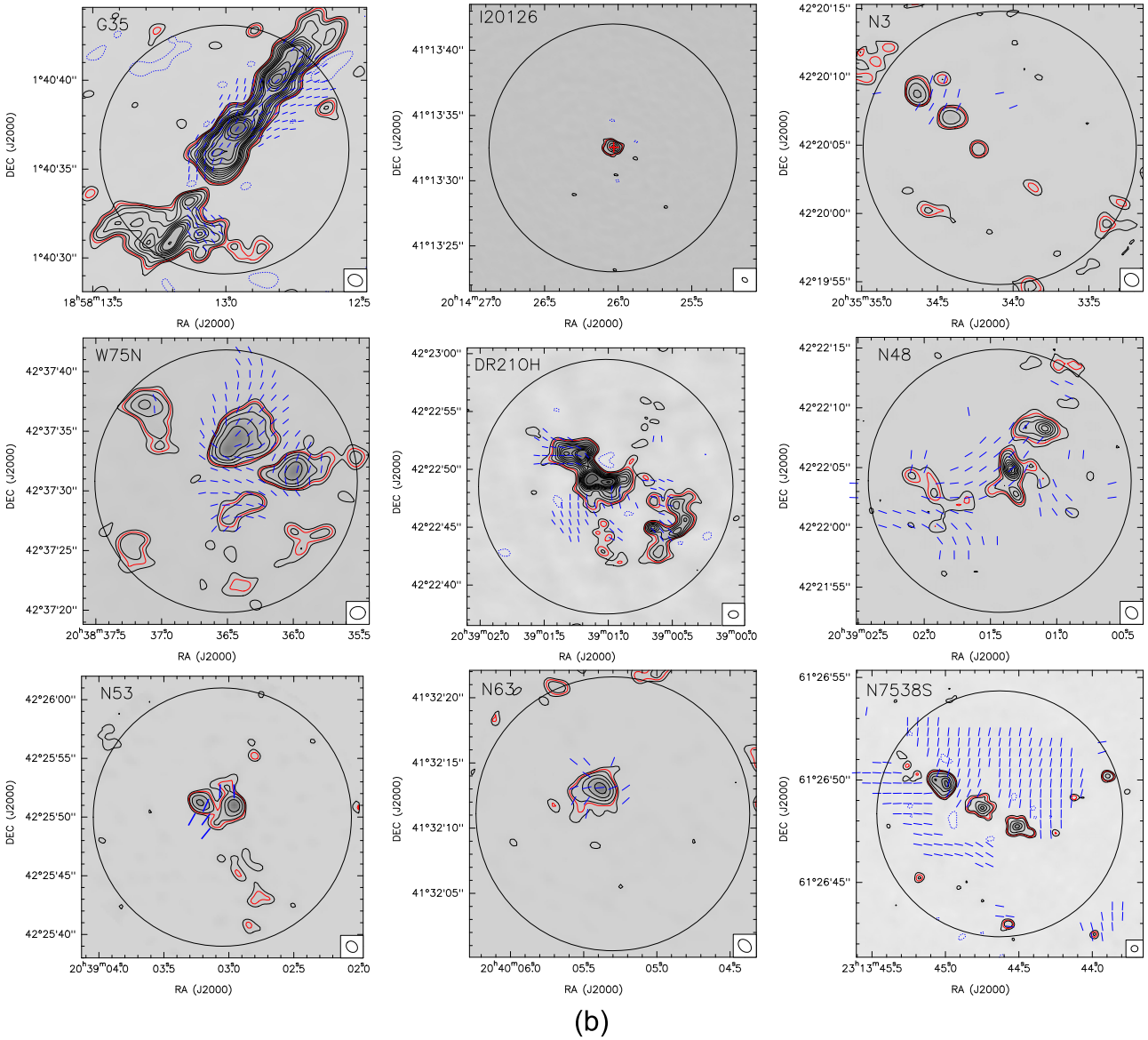

Figure 2. (Continued.)

contributing a nonnegligible part of the total nonthermal dispersion, as shown by recent simulations of gravitational contraction of turbulent cores (e.g., Guerrero-Gamboa & Vázquez-Semadeni 2020). An uncertainty of ∼10% is assumed for $\sigma_{\rm turb,spec}$ (e.g., Guerrero-Gamboa & Vázquez-Semadeni 2020).

A first estimate of the Q factor was performed from our $H^{13}CO^{+}$(4–3) first-order moment maps of Figures 14(a) and (b). These figures show that velocity gradients are clearly present in our regions. In an attempt to separate the turbulent component of the kinetic energy, $E_{\rm turb}$, from the total kinetic energy, $E_{\rm kin}$, which could be dominated by large-scale motions (e.g., rotation, infall), velocity dispersion functions (VDFs) were built for the same regions for which the ADF were also calculated in Section 4.4. The VDFs were calculated as

$$\langle[\Delta V(\ell)]^2\rangle^{1/2} \equiv \sqrt{\frac{1}{N(\ell)}\sum_{i=1}^{N(\ell)}[V(\boldsymbol{x}) - V(\boldsymbol{x}+\ell)]^2}\,, \qquad (2)$$

where V is the velocity along the line of sight at each position of our maps. We refer the reader to Section 4.4 for further details on the dispersion function. The results are shown in Figure 5 and $\sigma_{\rm turb,VDF}$, listed in Table 4, was estimated from the intercept value. Table 4 also reports the ratio $\sigma_{\rm turb}/\sigma_{\rm nonth}$ or Q. With the exception of W3IRS5 and N6334I, $\sigma_{\rm turb}/\sigma_{\rm nonth}$ averages to 0.4, with a standard deviation of 0.2, very consistent with the value measured in the simulations of Guerrero-Gamboa & Vázquez-Semadeni (2020). The two regions with $\sigma_{\rm turb}/\sigma_{\rm nonth} \sim 2$ could be affected by small-scale rotation or infalling motions, as found in previous works (e.g., Zhang et al. 1998, 2002). Actually, the spectrum of N6334I presents an absorption signature due to infall (Figure 4). Thus, our adopted value of $Q \sim 0.5$ seems reasonable.

For completeness, Table 4 also lists the values of the Mach number, $\mathcal{M}$, ranging from 3 to 11, and the values of the total kinetic energy $E_{\rm kin}$, the turbulent kinetic energy $E_{\rm turb}$, their ratio, and the gravitational energy $E_{\rm grav}$.

Table 3
Fitted Parameters of the Density and Temperature Structure of the Massive Dense Cores and Inferred Properties

ID-Source (1)	β[a] (2)	T_0[a] (K) (3)	ρ_0[a] (g cm^{-3}) (4)	p[a] (5)	χ_r[a] (6)	q[b] (7)	$M_{0.15\ pc}$[b] ($M_\odot$) (8)	$n_{0.15\ pc}$[b] (10^5 cm^{-3}) (9)	$T_{0.15\ pc}$[b] (K) (10)
1-W3IRS5	1.04 ± 0.12	260 ± 30	$(2.4 \pm 0.3) \times 10^{-17}$	1.46 ± 0.04	0.602	0.40	22 ± 3	1.8 ± 0.2	118
2-W3H2O	1.30 ± 0.16	152 ± 16	$(1.5 \pm 0.2) \times 10^{-16}$	1.90 ± 0.05	0.532	0.38	59 ± 8	4.8 ± 0.6	82
3-G192	1.36 ± 0.23	66 ± 6	$(4.1 \pm 0.6) \times 10^{-17}$	2.13 ± 0.08	0.338	0.37	11 ± 2	0.9 ± 0.1	42
4-N6334V	2.19 ± 0.25	96 ± 11	$(1.3 \pm 0.3) \times 10^{-16}$	1.89 ± 0.08	0.334	0.32	51 ± 12	4.2 ± 1.0	56
5-N6334A	2.18 ± 0.15	78 ± 8	$(4.6 \pm 0.7) \times 10^{-17}$	1.42 ± 0.05	0.455	0.33	46 ± 7	3.8 ± 0.6	40
6-N6334I	2.55 ± 0.22	111 ± 12	$(2.3 \pm 0.4) \times 10^{-16}$	2.02 ± 0.05	0.461	0.31	73 ± 13	6.0 ± 1.0	70
7-N6334In	2.10 ± 0.19	98 ± 12	$(8.8 \pm 1.5) \times 10^{-17}$	1.46 ± 0.05	0.518	0.32	81 ± 14	6.6 ± 1.0	52
8-G34-0	1.96 ± 0.24	63 ± 6	$(2.0 \pm 0.4) \times 10^{-16}$	2.26 ± 0.09	0.483	0.34	44 ± 9	3.6 ± 0.7	46
9-G34-1	1.39 ± 0.23	63 ± 7	$(8.2 \pm 1.5) \times 10^{-17}$	1.76 ± 0.08	0.488	0.37	42 ± 8	3.4 ± 0.6	33
10-G35	1.86 ± 0.15	90 ± 7	$(4.4 \pm 0.6) \times 10^{-17}$	1.53 ± 0.03	0.463	0.34	36 ± 5	3.0 ± 0.4	46
11-I20126	1.82 ± 0.24	86 ± 9	$(8.4 \pm 1.6) \times 10^{-17}$	2.21 ± 0.11	0.607	0.34	20 ± 4	1.6 ± 0.3	59
12-N3[c]	1.69 ± 0.31	45 ± 4	$(4.0 \pm 0.5) \times 10^{-17}$	1.58 ± 0.04	0.648	0.35	29 ± 4	2.4 ± 0.3	23
13-W75N	2.04 ± 0.18	112 ± 12	$(1.4 \pm 0.2) \times 10^{-16}$	1.99 ± 0.05	0.729	0.33	48 ± 7	4.0 ± 0.5	67
14-DR21OH	1.60 ± 0.26	73 ± 7	$(3.1 \pm 0.6) \times 10^{-16}$	1.98 ± 0.08	0.808	0.36	110 ± 20	8.6 ± 1.7	42
15-N48	1.88 ± 0.18	58 ± 5	$(1.0 \pm 0.2) \times 10^{-16}$	1.71 ± 0.05	0.459	0.34	56 ± 11	4.6 ± 0.9	31
16-N53[c]	1.55 ± 0.22	45 ± 4	$(9.7 \pm 1.8) \times 10^{-17}$	1.76 ± 0.07	0.487	0.36	49 ± 9	4.0 ± 0.7	24
17-N63[c]	1.80 ± 0.33	45 ± 3	$(6.5 \pm 1.1) \times 10^{-17}$	2.03 ± 0.07	0.570	0.34	20 ± 3	1.7 ± 0.3	27
18-N7538S	1.74 ± 0.19	93 ± 10	$(1.3 \pm 0.2) \times 10^{-16}$	1.72 ± 0.05	0.304	0.35	72 ± 5	5.9 ± 0.5	49

Notes.
[a] Free parameter fitted by the model: β is the dust emissivity index; T_0 and ρ_0 are the temperature and density at the reference radius, 1000 au; p is the density power-law index; χ_r is the reduced χ as defined in Equation (6) of Palau et al. (2014).
[b] Parameters of the massive dense cores inferred from the modeled density and temperature structures. q is the temperature power-law index. $M_{0.15\ pc}$ is the mass inside a region 0.15 pc in diameter computed according to $M_{0.15\ pc} = M(R = 0.075\text{pc}) = 4\pi\ \rho_0\ r_0^p\ \frac{R^{3-p}}{3-p}$; $n_{0.15\ pc}$ and $T_{0.15\ pc}$ correspond to the average H_2 density and temperature inside a region 0.15 pc in diameter. $T_{0.15\ pc}$ was estimated as $T_R = \frac{\int_0^R T(r)\rho(r)r^2dr}{\int_0^R \rho(r)r^2dr}$, where $T(r)$ and $\rho(r)$ were calculated as power laws with temperature at the reference radius given in column (3), temperature power-law index given in column (7), density at reference radius given in column (4) and density power-law index given in column (5) of this table. The final expression is $T_R = \frac{T_0(3-p)}{3-p-q}\left(\frac{r}{r_0}\right)^{-q}$.
[c] Sources for which only the radial intensity profile at 1.2 mm was fitted.

4.3. Determination of the Magnetic Field Strength: The Davis–Chandrasekhar–Fermi Method

Polarization observations of thermal dust emission at submillimeter wavelengths constitute a powerful tool to estimate the magnetic field strength onto the plane of the sky, B_{pos}. In order to estimate this, the Davis–Chandrasekhar–Fermi method (DCF, Davis 1951; Chandrasekhar & Fermi 1953) has been widely used. In this method, it is assumed that the turbulent kinetic energy and the turbulent magnetic energy are equal and that the turbulent gas induces the observed dispersion in the polarization position angles (PAs). Therefore, higher PA dispersions correspond to weak magnetic fields such that the turbulent gas can drag the field lines. Following Chandrasekhar & Fermi (1953), the magnetic field strength of the ordered component of the magnetic field, B_0, can be estimated from the following relation, once the density, ρ, turbulent velocity dispersion along the line of sight, σ_{turb}, and PA dispersion, σ_{PA}, are known:

$$B_0 \sim B_{pos} = \sqrt{4\pi\rho}\ \frac{\sigma_{turb}}{\delta B/B_0} \sim f\ \sqrt{4\pi\rho}\ \frac{\sigma_{turb}}{\sigma_{PA}}, \quad (3)$$

where it is assumed that $\delta B/B_0 \sim \sigma_{PA}$, with δB being the perturbed magnetic field on the top of B_0. In this equation, f is a numerical correction factor usually adopted to be 0.5 (Ostriker et al. 2001). This numerical factor was derived for cases where Equation (3) is valid, mainly for $\sigma_{PA} \lesssim 25°$. For larger dispersions, σ_{PA} should be replaced by $\tan \sigma_{PA}$ (Falceta-Gonçalves et al. 2008), and there is no need to apply the numerical correction factor f. The tangent correction is required in our case because our measured σ_{PA} are in some regions large (see below), up to 50°, and thus $\tan \sigma_{PA}$, which is what strictly corresponds to $\delta B/B_0$, cannot be approximated to σ_{PA}.

In the following subsections, we present two different approaches for estimating σ_{PA} following the DCF method.

4.3.1. Polarization PA Dispersion from Standard Deviation

In order to estimate a dispersion in polarization PA, we extracted the PA values, Φ, from each PA image, for the same region where fragmentation was assessed (0.15 pc in diameter), and rejected those angles with an error larger than ∼10° (11° for G34-1, and 15° for G192[20]), which corresponds to a signal-to-noise ratio smaller than 3 for the signal in polarization (Zhang et al. 2014). Three PA points per beam were extracted for each region.

A first approach to estimate σ_{PA} is based on the calculation of the standard deviation of the weighted mean. However, given the fact that the PA values have an error associated, it is desirable to subtract the contribution of the PA error to σ_{PA}.

[20] Only for the case of G192 did we include PA with errors ∼15° because an inspection of the PA values showed that there were two PA components, one around 20° and the other around 85°. The component around 20° is the one with large errors in the PA, but the different values of this component are very similar, making this component more significant (see Figure 2(a)). 15° of PA error corresponds to a signal-to-noise ratio ∼ 2.

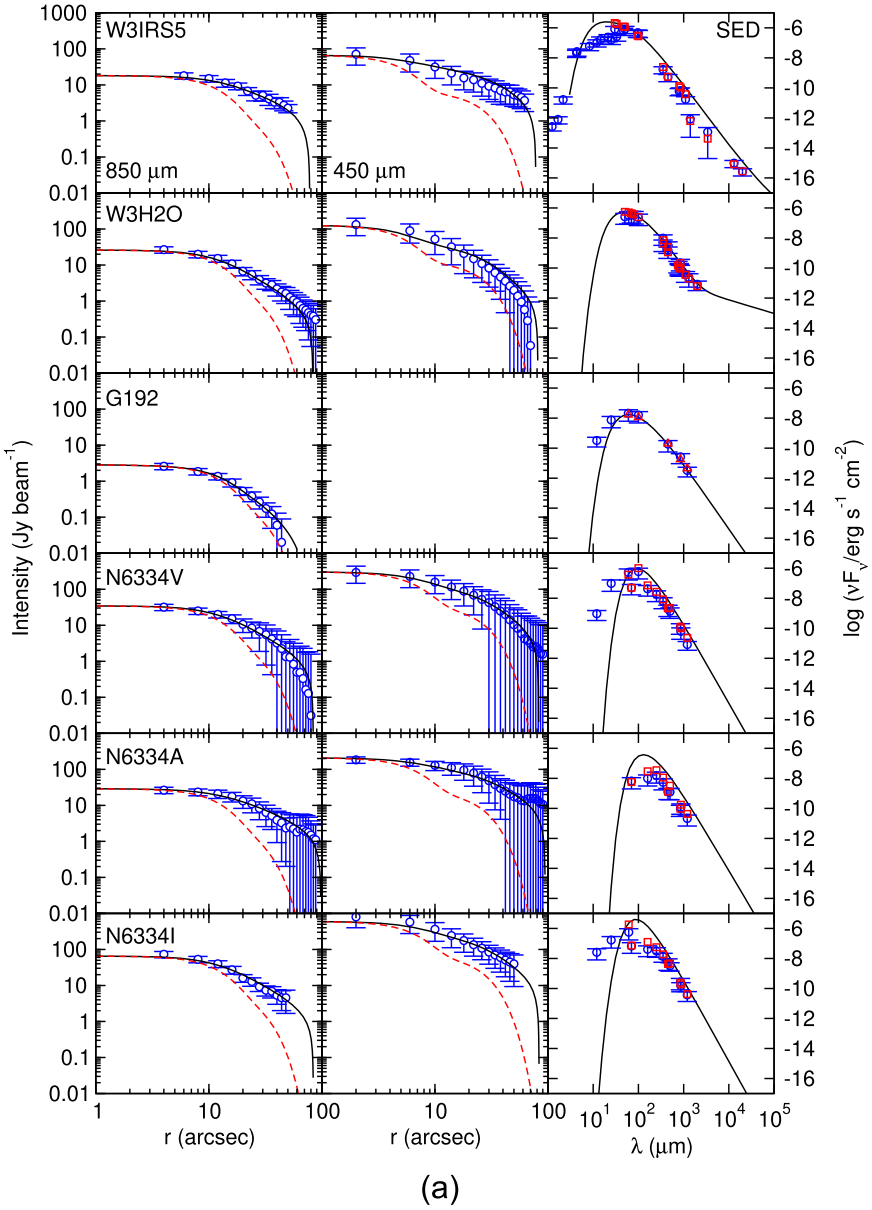

Figure 3. Best fits for six regions of the sample (see Table 3 for the exact fitted parameters). Each row corresponds to one core, the left (middle) panel shows the radial intensity profile at 850 (450) μm, with the empty blue circles corresponding to the data, the black solid line corresponding to the model, and the dashed red line showing the beam profile; panels on the right show the SED, with blue empty circles indicating the observed fluxes, the black solid line showing the model for a fixed aperture, and the red squares corresponding to the model for the same aperture where each flux was measured.

Thus, given a number N of PAs measured in a certain region, we have used the following expression:

$$\sigma_{\rm PA,stdev} = \sqrt{\frac{N\sum_{i=1}^{N} w_i(\Phi_i - \overline{\Phi}_w)^2}{(N-1)\sum_{i=1}^{N} w_i} - \frac{N}{\sum_{i=1}^{N} w_i}}, \quad (4)$$

where $\overline{\Phi}_w = \frac{\sum_{i=1}^{N} w_i\,\Phi_i}{\sum_{i=1}^{N} w_i}$ is the weighted mean of PAs, and the second term within the square root corresponds to the contribution of the PA errors to the dispersion (Equation A2 of Añez-López et al. 2020b). In these equations, w_i are the weights of each PA Φ_i, $w_i = 1/\delta\Phi_i^2$, with $\delta\Phi_i$ the PA error of each PA measurement. This final $\sigma_{\rm PA,stdev}$ can be considered as an intrinsic standard deviation because the contribution from the PA errors has been removed. The magnetic field strength in the plane of the sky following this approach is calculated as

$$B_{\rm stdev} = \sqrt{4\pi\rho}\,\frac{\sigma_{\rm turb}}{\tan\sigma_{\rm PA,stdev}}, \quad (5)$$

where $\sigma_{\rm turb}$ has been obtained from Equation (1) adopting $Q \sim 0.5$ (Section 4.2).

The obtained values of $\sigma_{\rm PA,stdev}$ and $B_{\rm stdev}$ for each region are listed in Table 5. $\sigma_{\rm PA,stdev}$ ranges from 6° to 50°, and their associated uncertainties were estimated from Monte Carlo simulations, to take into account the sparse sampling in our PA images (see Appendix D for further details). The uncertainties in $B_{\rm stdev}$ were estimated by propagating the uncertainties in the density, velocity dispersion, and $\sigma_{\rm PA,stdev}$.

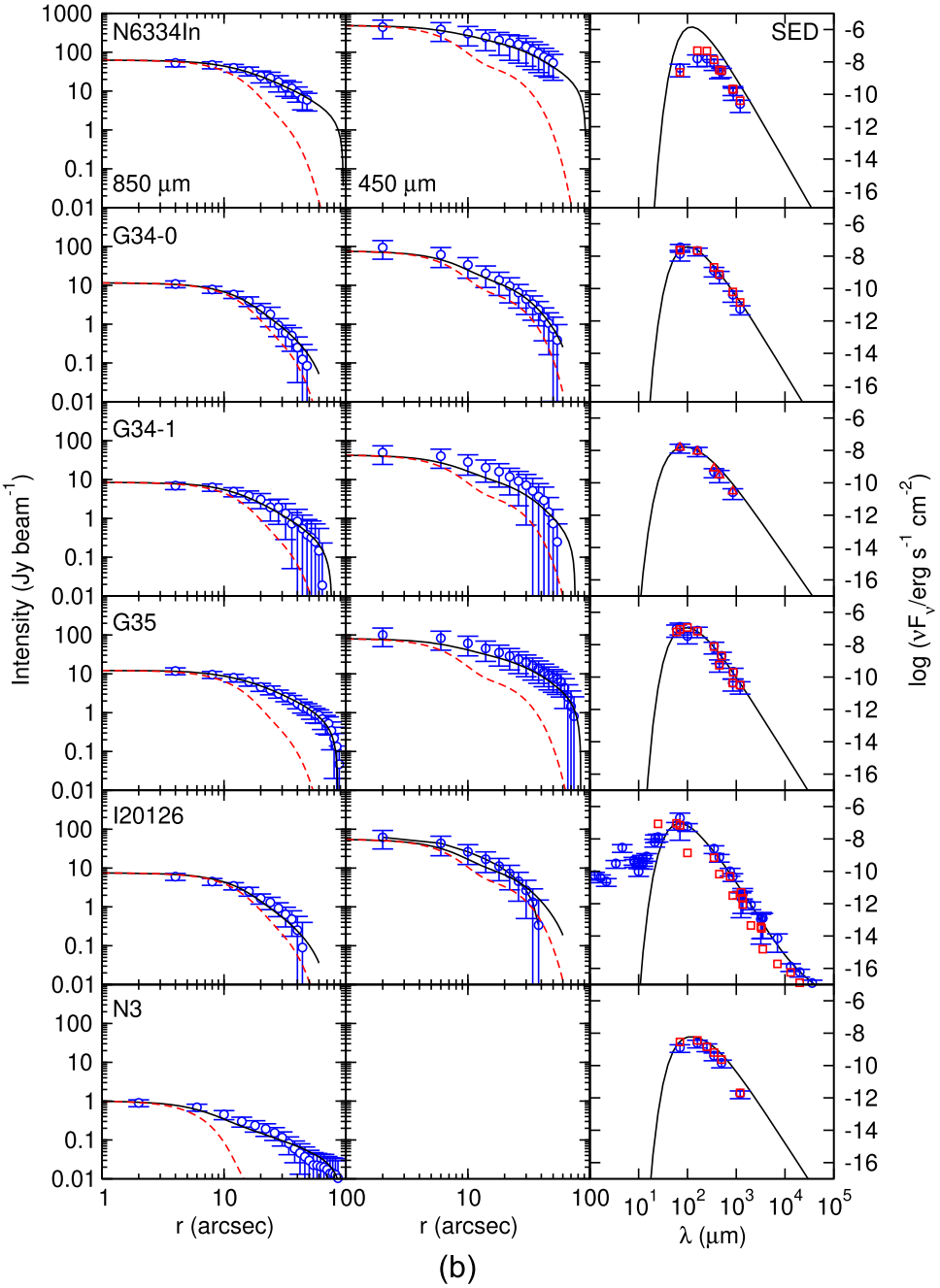

Figure 3. (Continued.)

4.3.2. Polarization PA Dispersion from Multiple Gaussian Fittings

In the previous section, $\sigma_{\rm PA}$ was estimated by calculating the standard deviation of the PAs. However, the dispersion values calculated from Equation (4) would systematically overestimate the dispersion in the cases where multiple components of the magnetic field are present. Thus, another approach to estimate the $\sigma_{\rm PA}$ is to fit Gaussians to the histogram of PAs. The number of bins was determined using the "auto" option of the "histogram" function of Python, and the resulting histograms are presented in Figure 6. For the cases of G192, N3 and N63, ∼4 points per beam were extracted from the PA image to allow a more robust fit of the histogram. In some cases, the histogram could be fitted with one single Gaussian component. In other cases, two (three) components were clearly separated in the PA histogram, and each component was fitted with a different Gaussian. However, there were cases clearly deviating from one single Gaussian but still with the two components merged so that it is ambiguous whether there are two (narrower) components or one (broader) component. In general, we considered separated PA components if the second peak of the tentative component is separated in *y*-axis by more than half of the peak of the strongest component while still being significant in number of points (around five). This implied fitting two components for the ambiguous cases of N6334I, DR21OH, and N63,[21] and three components for W75N.

[21] For the case of N63, we also tried to fit three PA components. This implied a stronger magnetic field by less than a factor of 2.

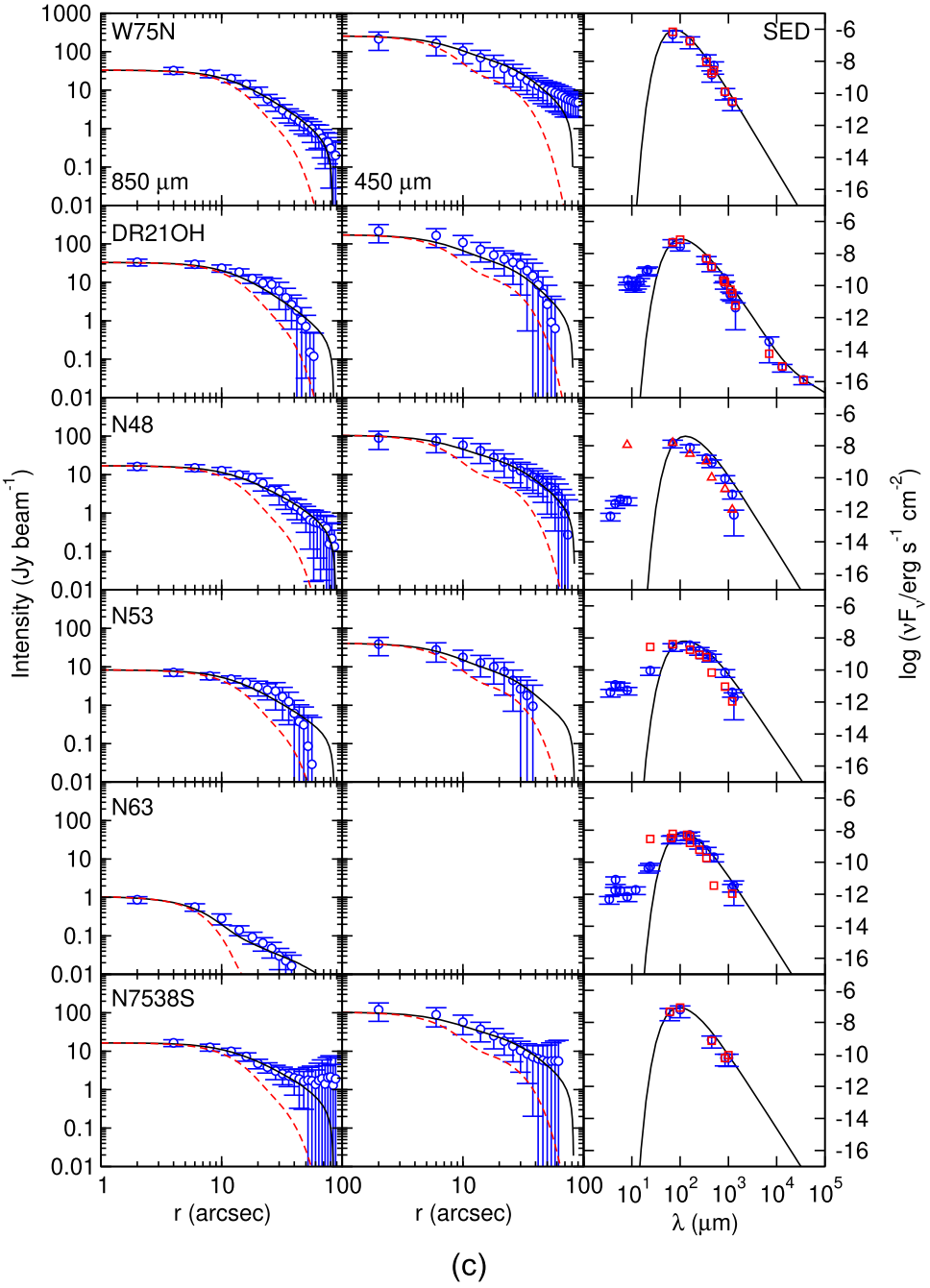

Figure 3. (Continued.)

The final PA dispersions following this approach, $\sigma_{\rm PA,gauss}$, were computed as the average width of the different components, weighted by the area of each Gaussian, and range from 6° to 24°. The magnetic field strength in the plane of the sky following this approach is calculated as

$$B_{\rm gauss} = \sqrt{4\pi\rho}\,\frac{\sigma_{\rm turb}}{\tan\sigma_{\rm PA,gauss}}, \quad (6)$$

where $\sigma_{\rm turb}$ has been obtained from Equation (1) adopting $Q \sim 0.5$ (Section 4.2).

The results are presented in Figure 6 and listed in Table 5. The uncertainty in $\sigma_{\rm PA,gauss}$ was estimated from Monte Carlo simulations as in the previous section (see Appendix D for further details).

4.4. Determination of the Magnetic Field Strength: The ADF Method

The previous approaches to estimate the PA dispersion could be introducing biases. First, the "standard deviation" approach could be overestimating $\sigma_{\rm PA}$ because it is ignoring the fact that there could be different magnetic field components within the same region and takes into account the large-scale variations of the PA. Second, the "multiple Gaussian" approach might be biased because of the decision of how many Gaussian components should be used. Both the "standard deviation" and the "multiple Gaussian" approaches might also be biased for broad PA distributions where PAs separated about 180° actually correspond to the same

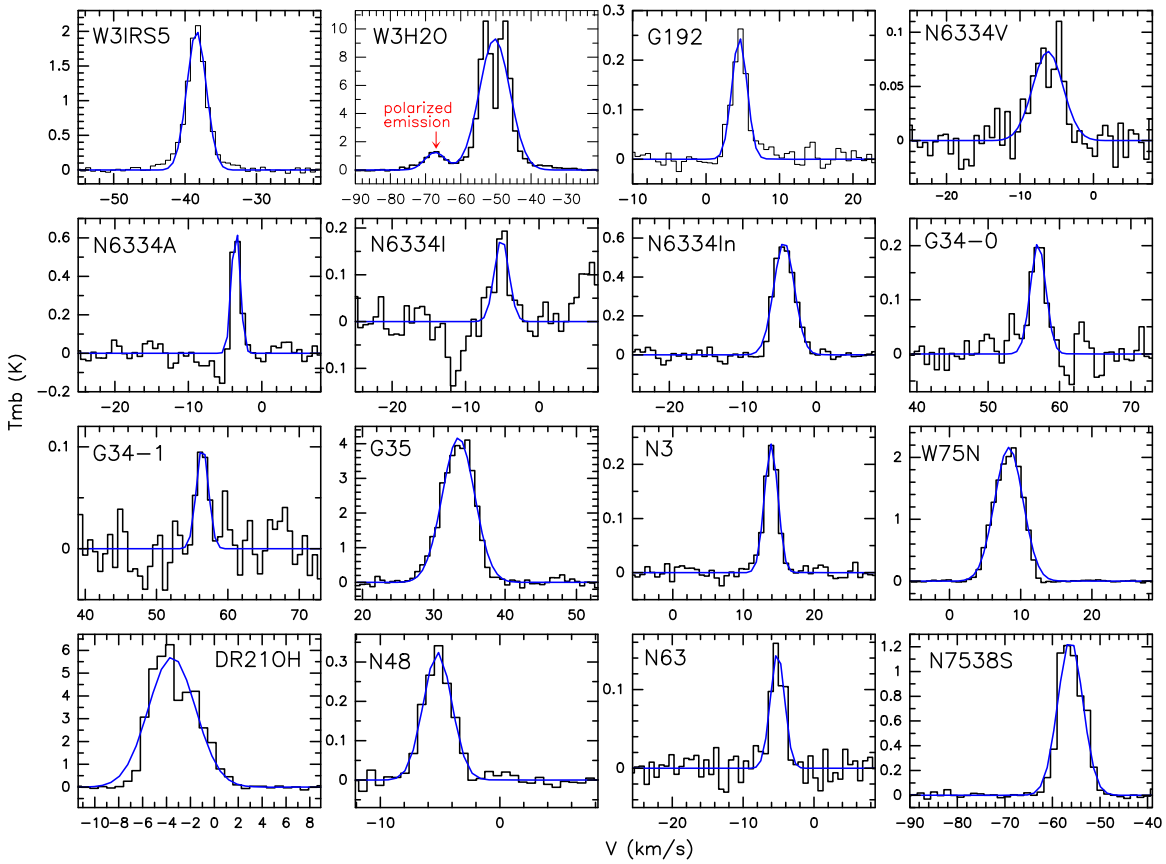

Figure 4. $H^{13}CO^{+}$(4–3) spectra (black) with the Gaussian fits (blue curves) performed to estimate the velocity dispersion in each region. For the case of W3H2O, the velocity component associated with the polarized emission is marked with a red arrow.

direction. Figure 6 shows that for 12 out the 16 regions studied here, the different PA components are separated by less than 90° and should not be strongly affected by this problem. Only four regions present very broad distributions, W3H2O, W75N, N48, and N63, with W3H2O being the most striking case (see also Table 5).

A possible way to estimate $\sigma_{\rm PA}$ or $\delta B/B_0$ more robustly is the statistical method proposed by Hildebrand et al. (2009) and Houde et al. (2009). This method is based on the calculation of the ADF, defined as

$$\langle[\Delta\Phi(\ell)]^2\rangle^{1/2} \equiv \sqrt{\frac{1}{N(\ell)}\sum_{i=1}^{N(\ell)}[\Phi(\boldsymbol{x}) - \Phi(\boldsymbol{x}+\ell)]^2}\,, \qquad (7)$$

where $\boldsymbol{x}$ is the position vector in the plane of the sky, $\ell \equiv |\ell|$, and $N(\ell)$ is the number of pairs of vectors separated by the displacement ℓ. The square of Equation (7) is also referred to as the structure function of the second order, but the structure function does not have angle units, and for this reason we refer to $\langle[\Delta\Phi(\ell)]^2\rangle^{1/2}$ as the ADF. The ADF can be calculated for those regions with a large number of detections of polarization PA so that calculating an average for each distance bin is feasible. For our sample, we applied this approach only to 11 regions, which are those with more than 45 PA detections. Figure 7 presents the ADF for these 11 regions. The ADF can be used in two different approaches to estimate $\delta B/B_0$.

4.4.1. The ADF at the Smallest (Beam) Scales

From the ADF, one can directly measure the PA dispersion at the smallest resolved scale in our observations, naturally separating the large-scale component of the magnetic field from the small-scale perturbations (Hildebrand et al. 2009). We define $\sigma_{\rm PA,\ ADFbeam}$ as the value of the ADF at scales equal to half the spatial scale of the beam, $\ell_{\rm B}$:

$$\sigma_{\rm PA,ADFbeam} \equiv \langle[\Delta\Phi(\ell_{\rm B}/2)]^2\rangle^{1/2}. \qquad (8)$$

The obtained values of $\sigma_{\rm PA,\ ADFbeam}$ along with the magnetic field strength in the plane of the sky following this approach,

$$B_{\rm ADFbeam} = \sqrt{4\pi\rho}\,\frac{\sigma_{\rm turb}}{\tan\sigma_{\rm PA,ADFbeam}}, \qquad (9)$$

are listed in Table 5. Here, $\sigma_{\rm turb}$ has been obtained from Equation (1) adopting $Q \sim 0.5$ (Section 4.2). We refer to this approach as the "ADF beam" approach.

4.4.2. Fitting the ADF Following Houde et al. (2009)

Another approach to estimate $\delta B/B_0$ using the ADF was introduced by Houde et al. (2009). This approach takes into account the smoothing effect due to finite resolutions and the integration along the line of sight. In addition, it separates the contribution of large-scale magnetic fields to angle dispersions because it assumes that there are two statistically independent components of the magnetic field. One component is related to the large-scale, ordered, magnetic field, B_0, and the other component corresponds to a perturbed or turbulent magnetic field, $B_{\rm t}$ (or δB). With this assumption, Houde et al. (2009)

Table 4
Kinematic Properties of the Sample from the $H^{13}CO^+$(4–3) SMA Data

Source	$\Delta v_{0.15\ pc}$ [a]	σ_{tot} [a]	σ_{nonth} [a]	$\sigma_{turb,VDF}$ [b]			E_{kin} [c]	E_{turb} [c]	E_{grav} [d]	
	(km s^{-1})	(km s^{-1})	(km s^{-1})	(km s^{-1})	$\mathcal{M}$ [a]	$\frac{\sigma_{turb}}{\sigma_{nonth}}$ [b]	(10^{45} erg) [c]	(10^{45} erg) [c]	(10^{45} erg) [c]	$\frac{E_{turb}}{E_{kin}}$
(1)	(2)	(3)	(4)	(5)	(6)	(7)	(8)	(9)	(10)	(11)
1-W3IRS5	3.20	1.36	1.35	2.63	3.6	1.95	1.24	4.62	0.34	3.7
2-W3H2O	6.72	2.85	2.84	1.30	9.1	0.46	14	2.96	2.36	0.2
3-G192	2.43	1.03	1.03	⋯	4.6	⋯	0.35	⋯	0.08	⋯
4-N6334V	4.87	2.07	2.06	1.05	8.0	0.51	6.59	1.69	1.81	0.3
5-N6334A	1.34	0.57	0.56	0.54	2.6	0.97	0.45	0.40	1.47	0.9
6-N6334I	2.31	0.98	0.97	2.87	3.4	2.96	2.11	18	3.65	8.5
7-N6334In	3.28	1.39	1.39	0.48	5.6	0.35	4.71	0.56	4.48	0.1
8-G34-0	2.54	1.08	1.07	⋯	4.6	⋯	1.53	⋯	1.31	⋯
9-G34-1	1.98	0.84	0.84	⋯	4.2	⋯	0.89	⋯	1.20	⋯
10-G35	5.34	2.27	2.26	0.64	9.7	0.28	5.57	0.44	0.90	0.1
11-I20126	⋯	⋯	⋯	⋯	⋯	⋯	⋯	⋯	0.26	⋯
12-N3	2.22	0.94	0.94	⋯	5.7	⋯	0.78	⋯	0.59	⋯
13-W75N	4.70	2.00	1.99	0.50	7.0	0.25	5.78	0.36	1.60	0.1
14-DR21OH	4.66	1.98	1.98	0.52	8.8	0.26	12.3	0.85	7.55	0.1
15-N48	2.87	1.22	1.22	0.47	6.3	0.39	2.50	0.37	2.16	0.2
16-N53	⋯	⋯	⋯	⋯	⋯	⋯	⋯	⋯	1.67	⋯
17-N63	2.36	1.00	1.00	⋯	5.5	⋯	0.61	⋯	0.28	⋯
18-N7538S	6.18	2.62	2.62	0.70	11	0.27	15	1.05	3.50	0.1

Notes.

[a] $\Delta v_{0.15\ pc}$ is the line width obtained from fitting a Gaussian to the $H^{13}CO^+$(4–3) spectrum averaged over a region 0.15 pc in diameter. $\sigma_{tot} = \Delta v_{0.15\ pc}/\sqrt{8\ \ln(2)}$ corresponds to the 1D total (thermal+nonthermal) velocity dispersion. $\sigma_{nonth} = \sqrt{\sigma_{tot}^2 - \sigma_{th}^2}$, with $\sigma_{th} = \sqrt{k_B\ T/(\mu\ m_H)}$ (k_B being the Boltzmann constant, μ the molecular weight(30 for $H^{13}CO^+$), m_H the mass of the hydrogen atom, and T the temperature of the region, taken from column (10) of Table 3). The Mach number $\mathcal{M}$ is calculated as $\sigma_{3D,nth}/c_s$, with c_s being the sound speed calculated as $c_s = \sqrt{k_B\ T/(\mu\ m_H)}$, using $\mu = 2.3$, and $\sigma_{3D,nth} = \sqrt{3}\ \sigma_{nonth}$.

[b] $\sigma_{turb,VDF}$ is taken from the velocity dispersion function at the smallest scale (Section 4.2) and thus should be free of large-scale systematic motions. $\frac{\sigma_{turb}}{\sigma_{nonth}}$ is calculated using $\sigma_{turb,VDF}$ and corresponds to Q in Section 4.2 and Equation (1).

[c] E_{kin} is the total kinetic energy calculated as $\frac{3}{2}M_{0.15\ pc}\sigma_{tot}^2$, E_{turb} is the turbulent kinetic energy calculated as $\frac{3}{2}M_{0.15\ pc}\sigma_{turb,VDF}^2$, and E_{grav} is the gravitational energy calculated as $\frac{3}{5}G\ M_{0.15\ pc}^2/R$, with $R = 0.15/2 = 0.075$ pc, and $M_{0.15\ pc}$ taken from Table 3.

calculated the ADF to study the change of polarization PA differences with ℓ and related the output of this statistical analysis to the ratio of B_t energy to B_0 energy, $b \equiv \langle B_t^2\rangle/\langle B_0^2\rangle$, which corresponds to $(\delta B/B_0)^2$ and can thus be used in Equation (3). We refer the reader to Houde et al. (2009) for further details on this approach. In short, Houde et al. (2009) calculate the ADF in the form

$$1 - \langle \cos[\Delta\Phi(\ell)]\rangle \simeq \frac{b}{N}(1 - e^{-\ell^2/(2\delta^2+4W^2)}) + a_2'\,\ell^2, \quad (10)$$

where δ is the magnetic field turbulent correlation length, W is the "beam radius" ($W = \mathrm{FWHM}/\sqrt{8\ln 2}$), a_2' is the coefficient of the parabolic approximation for the uniform part of the magnetic field in the ADF,[22] and N is the number of turbulent cells:

$$N \equiv \Delta'(\delta^2 + 2W^2)/(\sqrt{2\pi}\,\delta^3), \quad (11)$$

with Δ' being the effective thickness of the cloud, expected to be slightly smaller than the cloud thickness.[23] Here we assume that Δ' is equal to the core's thickness, taken as the diameter of the dense core in the plane of the sky as measured with the SMA (Koch et al. 2010). Thus, Equation (10) can be decomposed into a correlated component ($-\frac{b}{N}e^{-\ell^2/(2\delta^2+4W^2)}$), blue line in the bottom panels of Figure 8) and the contribution of the large-scale uniform magnetic field ($b/N + a_2'\,\ell^2$, red dashed line in the top panels of Figure 8).

By fitting Equation (10) to the observational data, the values for the three free parameters, b/N, δ, and a_2', are obtained. Only distances smaller than the physical distance of the largest angular scale of the SMA polarization observations ($\sim 12''$[24]) were taken into account to perform the fit. The b/N free parameter was allowed to vary from 0.025 to 5 in steps of 0.005, the δ free parameter was allowed to vary from 5 mpc to half the effective cloud thickness[25] (Table 6), and the a_2' free parameter was allowed to vary from -120 to 120 pc^{-2} in steps of 1 pc^{-2}. The fitted parameters were determined by minimizing χ^2.

Table 6 lists the three fitted parameters, δ, b/N, and a_2', along with the adopted value for Δ' (estimated from the SMA continuum images combining all available configurations), and

[22] The fact that the contribution of the uniform magnetic field in the ADF is approximated by a parabola does not necessarily mean that the morphology of the magnetic field follows a parabola, it rather corresponds to keeping the first ℓ^2 term in the Taylor expansion of Equation (42) of Houde et al. (2009), which is acceptable if $\ell$is less than a few times the beam radius W (Houde et al. 2009).

[23] As explained in Section 3.2 of Houde et al. (2009), Δ' can be interpreted as the width of the large-scale autocorrelation function, and can be thought as the proportion of the cloud that contains the bulk of the polarized flux. Thus, it necessarily needs to be smaller than the physical cloud thickness.

[24] For the particular cases of N6334V and N6334A, the largest distance considered for the fit is $\sim 20''$, because these two regions have slightly larger beams, of $\sim 5''$, than the beams for the other regions, $\sim 2''$–$3''$, and we require that at least a distance of four times the beam is covered. For W3H2O and N6334I, the largest distance considered for the fit was set to 0.06 pc because there were no data for larger distances.

[25] In the method described by Houde et al. (2009), δ is assumed to be much smaller than the thickness of the cloud. For this reason, we require that the upper limit of δ must be about half the effective thickness of the cloud Δ'.

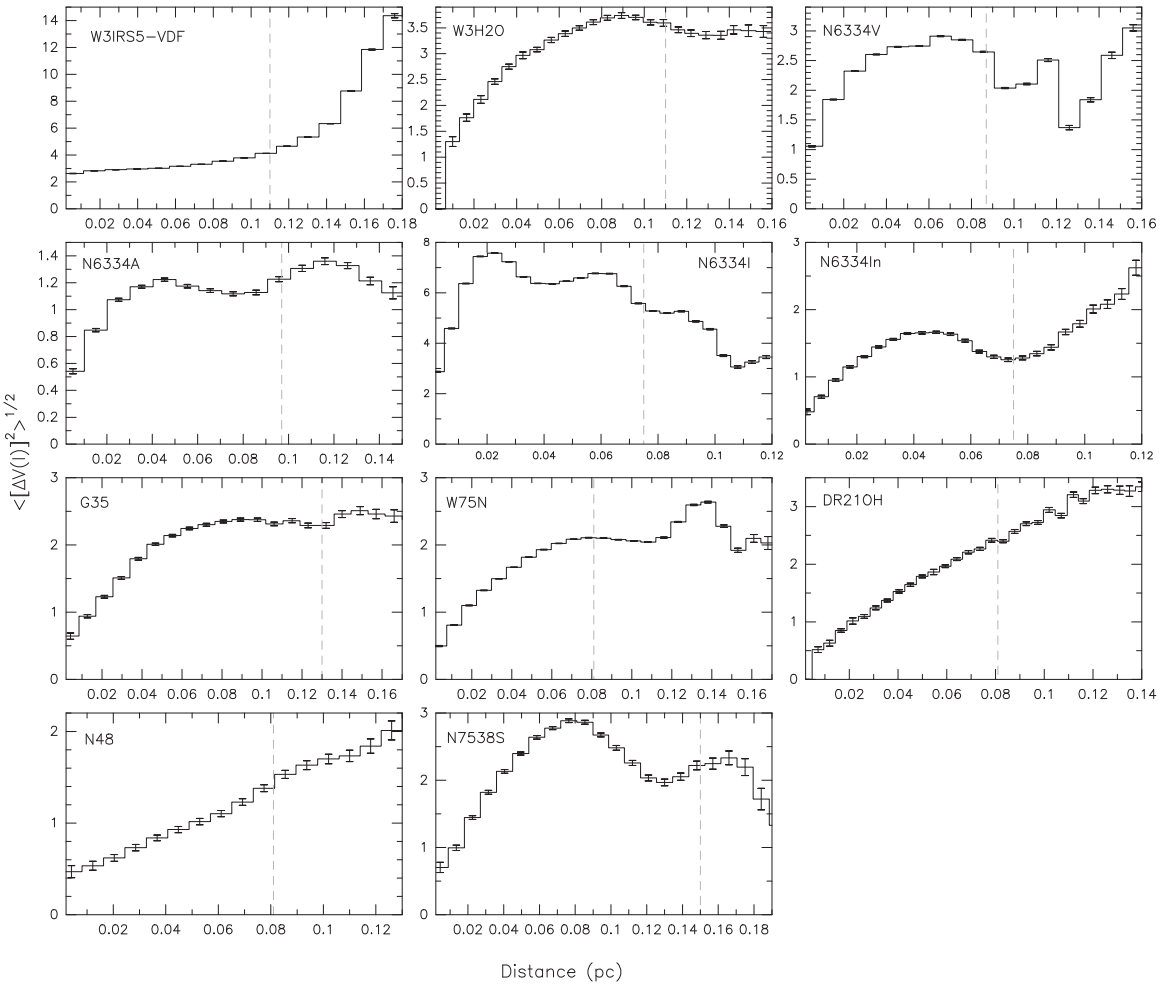

Figure 5. Velocity dispersion functions in km s^{-1} (i.e., $\langle[\Delta V(\ell)]^2\rangle^{1/2}$, as defined in Equation (2)), for the regions for which the ADF (Section 4.4) was also calculated, measured using the $H^{13}CO^+$(4–3) first-order moment maps of Figures 14(a) and (b). The dashed gray vertical line indicates the largest angular scale that the SMA is able to recover for the $H^{13}CO^+$(4–3) emission.

the corresponding values for N. $\langle B_t^2\rangle/\langle B_0^2\rangle$ and $B_{\rm ADFH09} \equiv \langle B_0^2\rangle^{1/2}$ are given in Table 5 to ease the comparison with the other methods/approaches used in this work. $B_{\rm ADFH09}$ has been calculated following equation (57) of Houde et al. (2009):

$$B_{\rm ADFH09} \equiv \langle B_0^2\rangle^{1/2} = \sqrt{4\pi\rho}\,\frac{\sigma_{\rm turb}}{\sqrt{\langle B_t^2\rangle/\langle B_0^2\rangle}}, \qquad (12)$$

where $\langle B_t^2\rangle/\langle B_0^2\rangle = b$. $\sigma_{\rm turb}$ has been obtained from Equation (1) by adopting $Q \sim 0.5$ (Section 4.2). We refer to this approach as the "ADF H09" approach. The uncertainty of the free parameter b/N controlling $\langle B_t^2\rangle/\langle B_0^2\rangle$ has been estimated from Monte Carlo simulations as described in Appendix D (where we followed Liu et al. 2019).

A discussion of how these values compare to the previous methods/approaches is presented below.

4.5. A Comparison between the DCF and ADF Methods

In Sections 4.3.1, 4.3.2, 4.4.1, and 4.4.2, $\delta B/B_0$ was estimated using two different methods (DCF, ADF), with two approaches for each method. We then calculated the magnetic field strength following Equations (5), (6), (9), and (12), and using the density and velocity dispersion inferred in Sections 4.1 and 4.2 (Equation (1)), with all quantities averaged within 0.15 pc in diameter. It is important to emphasize that while the fragmentation level is measured in SMA/PdBI/NOEMA images obtained using only extended configurations, thus filtering out typically angular scales larger than $\sim 3''$ (Table 1), the polarized and $H^{13}CO^+$ emissions are obtained from images including also subcompact and/or compact SMA configurations, thus filtering out much larger scales, of 14″–30″. The density is obtained from the modeling of the radial intensity profiles and SEDs obtained from single-dish data with angular resolutions $\gtrsim 11''$. Thus, the magnetic field strength is calculated using data sensitive to the core scale and averaged within this same scale (0.15 pc in diameter), while the fragmentation level is obtained using data sensitive only to much smaller scales (<0.03 pc).

Now we would like to compare the results of the four different approaches followed to estimate $\delta B/B_0$ in Equation (3). The "ADF H09" approach should be more robust than the "standard deviation" and the "multiple Gaussian" approaches because it decomposes the total magnetic field into the perturbed and the uniform parts taking into account the effects of the beam smoothing and the average along the line of sight (although it also has large uncertainties associated, as shown by Liu et al. 2019). The "ADF beam" approach should also provide a very good estimate of the PA dispersion at small scales (turbulent component of the magnetic

Table 5
Magnetic Field Properties Derived Using the DCF and ADF Methods

ID	$\sigma^{\rm PA}_{\rm stdev}$ [a]	$\sigma^{\rm PA}_{\rm gauss}$ [b]	$\sigma^{\rm PA}_{\rm ADFbeam}$ [c]	$\frac{\langle B_t^2\rangle}{\langle B_0^2\rangle}$ [c]	$B_{\rm stdev}$ [a]	$B_{\rm gauss}$ [b]	$B_{\rm ADFbeam}$ [c]	$B_{\rm ADFH09}$ [c]	$B_{\rm lit}$ [d]	$\mu_{\rm stdev}$ [a]	$\mu_{\rm gauss}$ [b]	$\mu_{\rm ADFbeam}$ [c]	$\mu_{\rm ADFH09}$ [c]	$\mu^{\rm S21}_{\rm gauss}$ [b]
	(°)	(°)	(°)		(mG)	(mG)	(mG)	(mG)	(mG)					
(1)	(2)	(3)	(4)	(5)	(6)	(7)	(8)	(9)	(10)	(11)	(12)	(13)	(14)	(15)
1	50 ± 7	23 ± 4	18 ± 2	1.37 ± 0.93	0.2 ± 0.1	0.5 ± 0.1	0.7 ± 0.1	0.2 ± 0.1	⋯	1.8 ± 0.6	0.6 ± 0.2	0.5 ± 0.1	1.8 ± 0.8	1.4
2	41 ± 11	9 ± 3	16 ± 2	1.01 ± 0.69	0.9 ± 0.4	4.7 ± 1.5	2.7 ± 0.5	0.8 ± 0.3	4.6	1.0 ± 0.5	0.2 ± 0.1	0.3 ± 0.1	1.2 ± 0.5	0.7
3	18 ± 6	8 ± 8	⋯	⋯	0.4 ± 0.1	0.8 ± 0.9	⋯	⋯	⋯	0.5 ± 0.2	0.2 ± 0.2	⋯	⋯	0.7
4	35 ± 6	12 ± 5	14 ± 1	0.66 ± 0.54	0.7 ± 0.2	2.4 ± 1.2	2.1 ± 0.5	0.6 ± 0.3	0.7	1.1 ± 0.5	0.3 ± 0.2	0.4 ± 0.2	1.2 ± 0.7	1.0
5	16 ± 6	7 ± 3	11 ± 2	0.16 ± 0.03	0.5 ± 0.2	1.1 ± 0.5	0.7 ± 0.2	0.3 ± 0.1	⋯	1.5 ± 0.7	0.6 ± 0.3	1.0 ± 0.4	2.1 ± 0.7	2.5
6	7 ± 3	8 ± 3	6 ± 1	0.04 ± 0.01	2.6 ± 1.4	2.1 ± 1.0	2.9 ± 0.7	1.4 ± 0.3	2.8	0.4 ± 0.3	0.5 ± 0.3	0.4 ± 0.1	0.8 ± 0.3	2.0
7	6 ± 3	7 ± 4	5 ± 1	0.08 ± 0.01	4.1 ± 2.3	3.3 ± 2.1	4.7 ± 1.3	1.6 ± 0.3	3.2	0.3 ± 0.2	0.4 ± 0.2	0.3 ± 0.1	0.8 ± 0.3	1.4
8	17 ± 6	18 ± 7	⋯	⋯	0.8 ± 0.4	0.8 ± 0.4	⋯	⋯	0.5	0.8 ± 0.4	0.9 ± 0.5	⋯	⋯	2.1
9	6 ± 2	6 ± 5	⋯	⋯	1.8 ± 0.7	1.8 ± 1.5	⋯	⋯	1.1	0.4 ± 0.2	0.4 ± 0.3	⋯	⋯	1.6
10	33 ± 5	23 ± 3	9 ± 2	0.32 ± 0.11	0.7 ± 0.2	1.1 ± 0.2	2.9 ± 0.6	0.8 ± 0.2	1.4	0.7 ± 0.2	0.5 ± 0.1	0.2 ± 0.1	0.7 ± 0.2	1.1
11	⋯	⋯	⋯	⋯	⋯	⋯	⋯	⋯	1.8	⋯	⋯	⋯	⋯	⋯
12	47 ± 16	9 ± 7	⋯	⋯	0.2 ± 0.1	1.2 ± 0.9	⋯	⋯	0.3	2.6 ± 1.6	0.4 ± 0.3	⋯	⋯	1.4
13	35 ± 16	24 ± 13	21 ± 1	2.08 ± 0.91	0.7 ± 0.4	1.1 ± 0.7	1.2 ± 0.2	0.3 ± 0.1	⋯	1.1 ± 0.7	0.7 ± 0.4	0.6 ± 0.2	2.2 ± 0.8	1.4
14	32 ± 13	22 ± 12	19 ± 2	1.21 ± 0.30	1.1 ± 0.6	1.7 ± 1.0	2.1 ± 0.4	0.6 ± 0.1	1.8	1.4 ± 0.9	0.9 ± 0.6	0.8 ± 0.3	2.5 ± 1.0	2.0
15	43 ± 12	19 ± 9	20 ± 2	2.73 ± 0.54	0.3 ± 0.2	0.9 ± 0.5	0.9 ± 0.2	0.2 ± 0.1	0.5	2.5 ± 1.4	0.9 ± 0.6	1.0 ± 0.4	4.4 ± 1.6	2.2
16	⋯	⋯	⋯	⋯	⋯	⋯	⋯	⋯	0.8	⋯	⋯	⋯	⋯	⋯
17	46 ± 20	25 ± 14	⋯	⋯	0.2 ± 0.1	0.3 ± 0.2	⋯	⋯	⋯	2.0 ± 1.5	0.9 ± 0.7	⋯	⋯	1.9
18	38 ± 4	8 ± 2	6.0 ± 1	0.51 ± 0.60	1.0 ± 0.2	5.2 ± 1.5	7.3 ± 2.0	1.1 ± 0.7	⋯	1.1 ± 0.4	0.2 ± 0.1	0.2 ± 0.1	1.0 ± 0.7	0.8

Notes.

[a] $\sigma^{\rm PA}_{\rm stdev}$ corresponds to the PA dispersion calculated within a region 0.15 pc in diameter and using the "standard deviation" approach as described in Section 4.3.1. $B_{\rm stdev}$ is calculated using the DCF method and following Equation (5), for which $n_{0.15\ \rm pc}$ is taken from Table 3 and $\Delta v_{0.15\ \rm pc}$ is taken from Table 4. $\mu_{\rm stdev}$ is the observed mass-to-flux ratio over the critical value, calculated following Equation (14) (Section 4.6) and using $B_{\rm stdev}$.

[b] $\sigma^{\rm PA}_{\rm gauss}$ corresponds to the PA dispersion calculated within a region 0.15 pc in diameter and using the "multiple Gaussian" approach as described in Section 4.3.2. $B_{\rm gauss}$ is calculated using the DCF method and following Equation (6). $\mu_{\rm gauss}$ is the observed mass-to-flux ratio over the critical value, calculated following Equation (14) and using $B_{\rm gauss}$. $\mu^{\rm S21}_{\rm gauss}$ corresponds to the observed mass-to-flux ratio over the critical calculated following Skalidis & Tassis (2021), see Section 5.1.4).

[c] $\sigma^{\rm PA}_{\rm ADFbeam}$ corresponds to the PA dispersion calculated within a region 0.15 pc in diameter and using the "ADF beam" approach as described in Section 4.4.1. $B_{\rm ADFbeam}$ is calculated following Equation (9). $\mu_{\rm ADFbeam}$ is the observed mass-to-flux ratio over the critical value, calculated following Equation (14) and using $B_{\rm ADFbeam}$. $\langle B_t^2\rangle/\langle B_0^2\rangle$ is the ratio of the perturbed magnetic field energy versus the ordered magnetic field energy. $B_{\rm ADFH09}$ is calculated using the "ADF H09" approach following Equation (12). $\mu_{\rm ADFH09}$ is the corresponding observed mass-to-flux ratio over the critical.

[d] $B_{\rm lit}$ is the magnetic field strength for each region as reported in the literature (see Section 5.1.5). The references and the method used in each case are as follows: W3H2O: Chen et al. (2012a, DCF); N6334V: Juárez et al. (2017, ADF); N6334I and N6334In: Li et al. (2015, force equilibrium between gravity, magnetic tension, and magnetic pressure); G34-0 and G34-1: Tang et al. (2019, ADF for single dish); G35: Qiu et al. (2013, ADF); I20126: Edris et al. (2005, Zeeman effect of OH masers); N3 and N53: Hezareh et al. (2013, ion–neutral); DR21OH: Girart et al. (2013, ADF) and Hezareh et al. (2010, ion–neutral); N48: Ching et al. (2017, ADF).

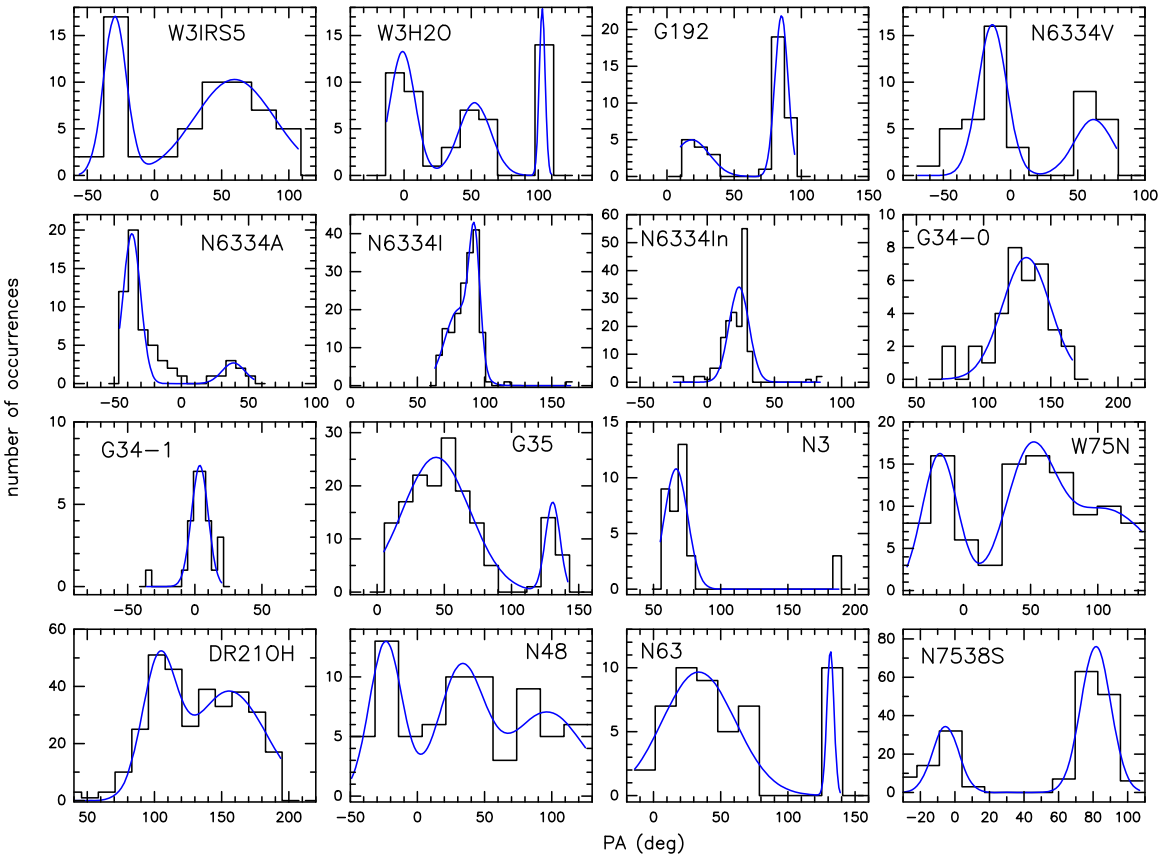

Figure 6. Polarization angle histograms (black) with the Gaussian fits (blue curves) performed in Python to estimate $\sigma_{\rm PA,gauss}$ in each region. In all panels, the full range of 180° is shown.

field) because it requires no assumptions with respect to the large-scale field. However, both the "ADF beam" and the "ADF H09" approaches could be applied only to 11 regions of our sample, while the other two approaches ("standard deviation" and "multiple Gaussian") could be applied to 16 regions. If $\sigma_{\rm PA,stdev}$ or $\sigma_{\rm PA,gauss}$ were shown to correlate to $\sigma_{\rm PA,ADFbeam}$ or $\langle B_{\rm t}^2\rangle/\langle B_0^2\rangle$, this would suggest that such a determination of $\sigma_{\rm PA}$ is a reasonable approach.

In Figure 9, we present plots comparing the four different approaches used in this work to estimate $\delta B/B_0$ ($\sigma_{\rm PA,stdev}$, $\sigma_{\rm PA,gauss}$, $\langle B_{\rm t}^2\rangle/\langle B_0^2\rangle$, and $\sigma_{\rm PA,ADFbeam}$). In each panel of the figure, the p value is listed (probability that the null hypothesis is true, i.e., that the correlation is due to a random process). As can be seen from the figure, the p values are in all cases $\lesssim 0.01$ (with the exception of the $\sigma_{\rm PA,stdev}$ versus $\sigma_{\rm PA,ADFbeam}$ plot). This comparison reveals that (i) $\sigma_{\rm PA,ADFbeam}$ is very well correlated with the $\langle B_{\rm t}^2\rangle/\langle B_0^2\rangle$ of the "ADF H09" approach. This was expected because the Houde et al. (2009) method is precisely aimed at separating the PA dispersion at the small scales from the large-scale ordered field. However, $\langle B_{\rm t}^2\rangle/\langle B_0^2\rangle$ systematically deviates more for increasing $\sigma_{\rm PA,ADFbeam}$. (ii) $\sigma_{\rm PA,gauss}$ correlates quite well with $\sigma_{\rm PA,ADFbeam}$, and actually, their relation is very close to the one-to-one relation. This indicates that the "multiple Gaussian" approach is achieving a reasonable estimate of the PA dispersion at the smallest scales. (iii) While all of the approaches correlate to each other, the tighter correlation is found between $\sigma_{\rm PA,stdev}$ and $\langle B_{\rm t}^2\rangle/\langle B_0^2\rangle$, with a p value of 0.0046. $\sigma_{\rm PA,stdev}$ might be better related to $\langle B_{\rm t}^2\rangle/\langle B_0^2\rangle$ than $\sigma_{\rm PA,gauss}$ because of the uncertainty in the decision of how many Gaussians should be fitted to the PA histograms to finally obtain $\sigma_{\rm PA,gauss}$. (iv) The relation between $\sigma_{\rm PA,stdev}$ and $\langle B_{\rm t}^2\rangle/\langle B_0^2\rangle$ is very close to the one-to-one relation, meaning that the $\langle B_{\rm t}^2\rangle/\langle B_0^2\rangle$ probably includes "intermediate-scale" dispersion perhaps due to deviations from the parabolic approximation.

This comparison suggests that the determination of $\sigma_{\rm PA,stdev}$ is a reasonably good approach to $\sigma_{\rm PA}$ because it presents the lowest p value and the best correlation with the results of the ADF method. In the following, we will consider the value of $\sigma_{\rm PA,stdev}$ as the reference value for $\delta B/B_0$. A consistency check was performed by plotting $B_{\rm stdev}$ versus $n_{0.15\ {\rm pc}}$ in Figure 15 of Appendix E. The figure shows that there is a relation between these two quantities, as expected from Equation (3). Diagrams of the fragmentation level $N_{\rm mm}$ versus $B_{\rm pos}$ for the four approaches used here are presented in Figure 10.

4.6. The Mass-to-magnetic Flux Ratio μ

The ratio of the observed mass-to-magnetic flux over the critical mass-to-magnetic flux, μ, was calculated by following Equation (1) of Crutcher et al. (2004), which reads:

$$\mu \equiv \frac{(M/\Phi_{\rm B})_{\rm observed}}{(M/\Phi_{\rm B})_{\rm crit}} = \frac{m\,N(H_2)A/B_{\rm tot}A}{1/2\pi G^{1/2}}, \qquad (13)$$

where A refers to the area over which the mass M and the magnetic flux $\Phi_{\rm B}$ are measured, $m = 2.8m_{\rm H}$, with $m_{\rm H}$ the mass

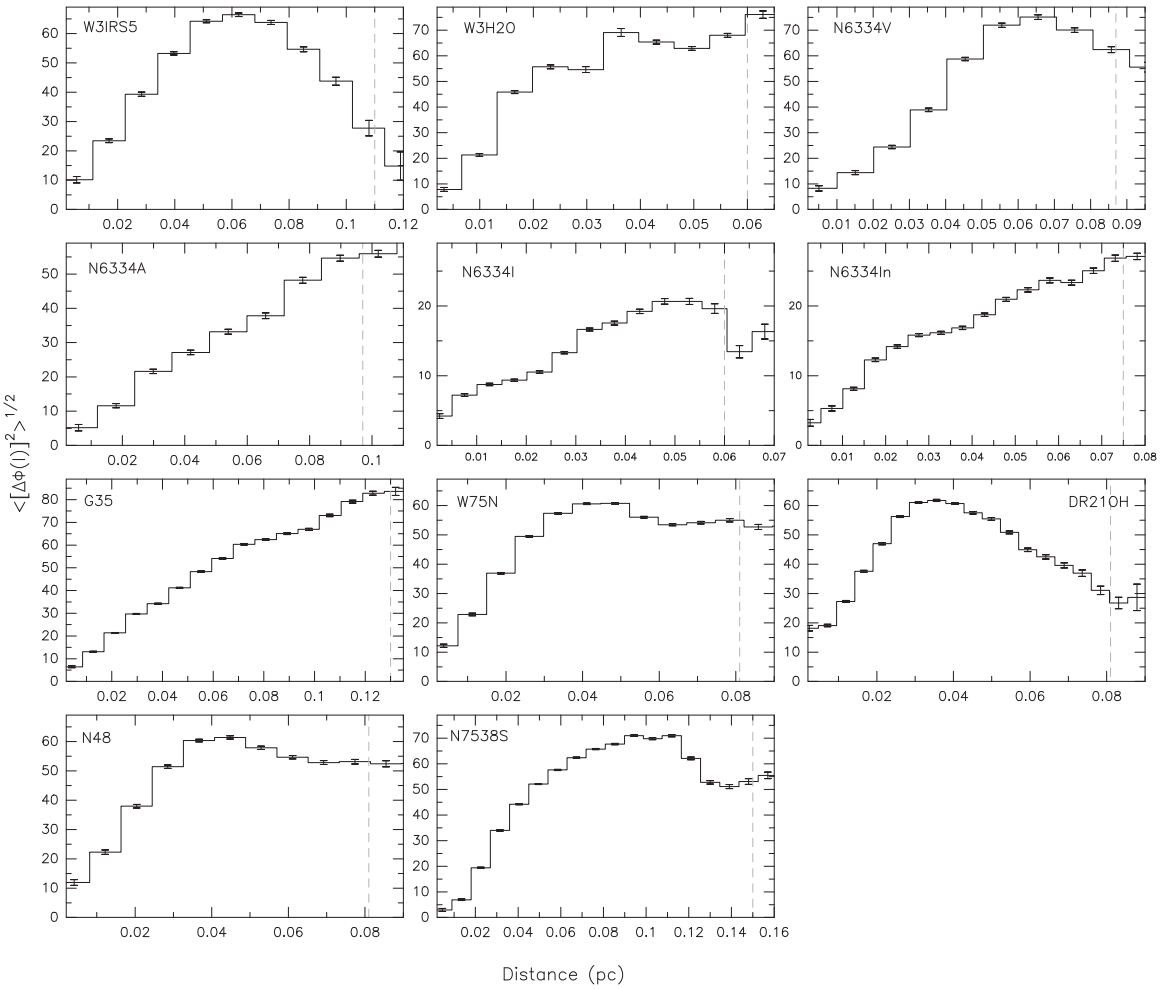

Figure 7. ADF (i.e., $\langle[\Delta\Phi(\ell)]^2\rangle^{1/2}$, as defined in Equation (7)) for each region with enough polarization detections. The dashed gray vertical line indicates the largest angular scale that the SMA is able to recover for the polarized emission.

of the hydrogen atom and $B_{\rm tot}$ the total (deprojected) magnetic field strength. In practical units, and writing the equation in terms of the magnetic field strength in the plane of the sky, for which its statistical average value is $B_{\rm pos} = \frac{\pi}{4} B_{\rm tot}$ (Crutcher et al. 2004), Equation (13) reads as

$$\mu = 5.969 \times 10^{-24} \frac{N(\mathrm{H_2})}{B_{\rm pos}}, \qquad (14)$$

with $B_{\rm pos}$ given in mG. $N(\mathrm{H_2})$ was calculated as $M_{0.15\,\rm pc}/\pi R^2 = n_{0.15\,\rm pc} R\,4/3$ for $R = 0.15/2 = 0.075$ pc.

The results are given in Table 5, and the right-hand panels of Figure 10 show $N_{\rm mm}$ versus μ for the four approaches used here. The figure reveals no apparent relation between $N_{\rm mm}$ and $B_{\rm pos}$, or $N_{\rm mm}$ and μ, for any of the methods/approaches used here.

In Figure 10, the cores classified as presenting "aligned fragmentation" (Table 2) are marked with blue squares. In general, these cores with "aligned fragmentation" present high fragmentation levels, and in most cases (four out of six), the magnetic field follows the direction perpendicular to the filamentary structure, which is fragmented. These cores span a wide range of magnetic field strengths and μ.

5. Discussion

5.1. Uncertainties in the Determination of the Magnetic Field Strength and Mass-to-flux Ratio μ

In previous sections, we estimated the magnetic field strength in the plane of sky following the DCF and ADF methods, and searched for a possible trend of this quantity with the fragmentation level. We found no clear trend between these two quantities. Before discussing the physical implications of this result, we should consider how robust our determination of the magnetic field strength is. In Figure 10 we plotted the magnetic field strength and μ with the corresponding uncertainties after taking into account the uncertainties in the density (Section 4.1), velocity dispersion (Section 4.2),and polarization PA dispersion (Appendix D).

5.1.1. Uncertainty in the Density

The estimate of the density uncertainty was described in Section 4.1 and was obtained by increasing the χ^2 in our model. However, an additional uncertainty could come from the different spatial filtering of single dishes (used to assess density) versus interferometers (used to assess velocity and PA dispersions). To assess how much the different spatial filtering

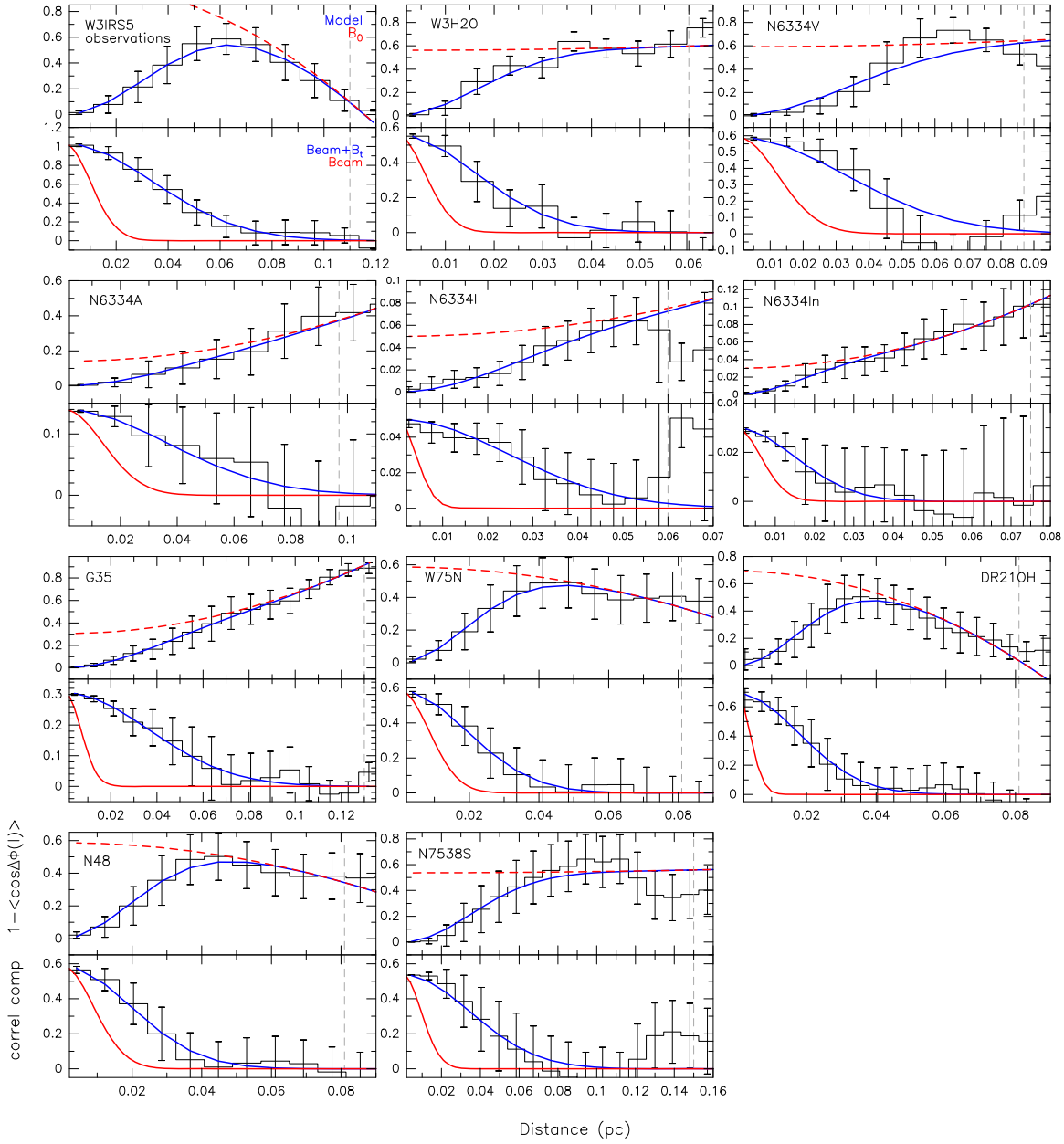

Figure 8. Results of the "ADF H09" approach (Section 4.4.2) for each region with enough polarization detections. For each region, the top panel corresponds to the $(1 - \langle \cos[\Delta\Phi(l)] \rangle)$ function, and the bottom panel corresponds to the correlated component (exponential term of Equation (10)). In both upper and lower panels, the black solid line and error bars correspond to the mean and standard deviation of all pairs in each bin. The red dashed line corresponds to the large-scale uniform magnetic field (i.e., it does not contain the correlated component of the function and is $b/N + a_2' l^2$). In the upper panel, the blue line shows the fit to the data using Equation (10), and in the bottom panel, the blue line shows the correlation due to the beam and the turbulent component of the magnetic field, while the solid red line corresponds to the correlation due to the beam alone. The dashed gray vertical line indicates the largest angular scale that the SMA is able to recover for the polarized emission, below which the fit was performed.

of each telescope could affect our determination of the magnetic field strength, the average density was estimated using the SMA continuum flux densities, including all of the configurations available as in the case of the polarization and $H^{13}CO^+$ data. For each region, we estimated the total mass recovered by the SMA (Appendix F) and found that the amount of mass filtered out by the SMA is on average only ∼25% of the mass inferred from the modeling of the single-dish data presented in Section 4.1. In Figure 16 of Appendix F, we present a plot of the SMA average density versus single-dish average density, showing a relation close to one to one, with the SMA densities only slightly below the single-dish densities. Therefore, the slightly different spatial filtering between the single dish and the SMA is not heavily affecting our results. The figure also indicates that the deviation from the spherical assumption of our model should not strongly affect our results either. The advantage of using single-dish telescopes to infer the density structure is that the temperature structure can be better determined, thanks to the simultaneous fitting of the SED and the radial intensity profiles.

5.1.2. Uncertainty in the Velocity Dispersion

Regarding the estimate of the velocity dispersion, the $H^{13}CO^+$(4–3) transition was used. This is a good tracer of

Table 6
Magnetic Field Properties Derived Using the ADF with the Houde et al. (2009) Approach "ADF H09"

Source (1)	δ^{a} (mpc) (2)	$\frac{b}{N}^{a}$ (3)	$a_2'^{a}$ (pc^{-2}) (4)	Δ'^{a} (mpc) (5)	N^{a} (6)
1-W3IRS5	31 ± 1	1.03 ± 0.69	-77 ± 1	85 ± 24	1.3 ± 0.1
2-W3H2O	14 ± 1	0.56 ± 0.38	10 ± 1	47 ± 14	1.8 ± 0.2
4-N6334V	28 ± 1	0.59 ± 0.47	7 ± 1	57 ± 29	1.1 ± 0.1
5-N6334A	31 ± 1	0.14 ± 0.03	25 ± 1	63 ± 32	1.1 ± 0.1
6-N6334I	24 ± 1	0.05 ± 0.01	7 ± 1	50 ± 10	0.9 ± 0.1
7-N6334In	12 ± 1	0.03 ± 0.01	13 ± 1	50 ± 15	2.6 ± 0.3
10-G35	35 ± 1	0.31 ± 0.10	36 ± 1	85 ± 16	1.0 ± 0.1
13-W75N	15 ± 1	0.59 ± 0.25	-38 ± 1	81 ± 20	3.5 ± 0.4
14-DR21OH	17 ± 1	0.69 ± 0.16	-100 ± 1	68 ± 10	1.8 ± 0.2
15-N48	15 ± 1	0.59 ± 0.10	-37 ± 1	102 ± 21	4.6 ± 0.5
18-N7538S	32 ± 1	0.54 ± 0.63	1 ± 1	64 ± 23	0.9 ± 0.1

Note.
[a] δ, b/N, and a_2' are the three free parameters of the "ADF H09" approach (Section 4.4.2). δ is the magnetic field turbulent correlation length, b/N is the value of the correlated component at the origin, and a_2' is the coefficient of the uniform parabolic approximation adopted in Equation (10). Δ' is the effective thickness of the cloud, estimated from the size of the SMA continuum emission obtained using all configurations. N is the number of turbulent cells along the line of sight. See Section 4.4.2 for further details on each parameter. The uncertainty in δ and a_2' are taken to be equal to the step of the explored parameter space, the uncertainty in Δ' is taken equal to one beam, and the uncertainty in N is assumed to be 10%. The uncertainty in b/N is estimated from Monte Carlo simulations performed to take into account the sparse sampling in our observations (Appendix D).

dense regions, which should correlate well with the polarized emission, as shown in Figures 14(a) and (b) of Appendix B. However, both the velocity dispersion and the PA dispersion could still be affected by the presence of outflows. As shown in Figures 14(a) and (b), the magnetic field is, for most of the cases, perpendicular to the outflows directions, with the only clear exception of N6334In and N7538S. Other cases where the polarized emission seems to follow the outflow directions are DR21OH and N48. In none of the regions is there evidence of the magnetic field segments being especially perturbed along the outflow directions. Thus, it is unlikely that the velocity and PA dispersions are strongly affected by outflows. It should also be noticed that both the velocity dispersion and the PA dispersion could be affected by large-scale systematic motions such as gas inflows. We discuss this possible effect in Section 5.4 and in Appendix G.

5.1.3. Uncertainty in the PA Dispersion

Here we list the main contributions to the PA dispersion uncertainty.

Sparse sampling of the data/poor sensitivity—In many cases, the polarized emission is detected only in certain portions of the entire continuum emission, preventing us from fully sampling it. This could be due to, for example, a lack of sensitivity. Poor sensitivity would hinder the detection of the polarized emission from low-density gas, which would probably add to the PA dispersion because the turbulent power should be larger in larger scales (Heitsch et al. 2001). This typically tends to overestimate the magnetic field strength. As already mentioned above, our adopted uncertainties take into account the sparse sampling effect (Appendix D).

Beam smoothing, average along the line of sight—Both effects imply an overestimation of the magnetic field strength because they tend to blur out the PA dispersion (Heitsch et al. 2001). In our case, both effects are taken into account in the "ADF H09" approach and it was shown in Section 4.5 that $\sigma_{\rm PA,stdev}$ correlates very well with $\langle B_t^2\rangle/\langle B_0^2\rangle$. Thus, it does not seem likely that our inferred values of the magnetic field strength are strongly affected by this.

Small-angle approximation—Given that some of our PA dispersions are large, the correction by Falceta-Gonçalves et al. (2008) was applied (Section 4.3), but there are other alternatives in the literature such as the one proposed by Heitsch et al. (2001). We applied Equation (12) of Heitsch et al. (2001) for the "standard deviation" case, and in general, the values of the B-field strength are smaller by 10%, except in a few cases, implying an average magnetic field with the Heitsch +01 equation, which is about 40% smaller than the average value with Falceta-Gonçalves equation. Other corrections have been proposed (Hildebrand et al. 2009; Houde et al. 2009, 2011; Franco et al. 2010; Koch et al. 2010), but they typically imply a factor well below 4 (see Cortes et al. 2016, 2019 for a comparison among the values obtained using the different corrections).

Very strong ordered magnetic fields—The superposition of δB with a strong and uniform large-scale field could produce an underestimation of the small-scale turbulent dispersion because the weight of almost no large-scale dispersion will effectively reduce the small-scale turbulent dispersion. Such extremely ordered configurations are not typical in our sample.

Very weak magnetic fields—In the "ADF H09" approach, $\langle B_t^2\rangle/\langle B_0^2\rangle$ could be underestimated for the cases of very weak magnetic fields. In these cases, the magnetic field could be so strongly perturbed that it could resemble a random field with no important changes with distance, implying an overestimation of the large-scale ordered field. However, such an extremely disordered and random-like magnetic field is not seen in our observations (Figures 2(a) and (b)).

5.1.4. Intrinsic Uncertainty of the Methods Applied

In addition to all the specific uncertainties mentioned above, a number of caveats have been raised in the literature regarding the use of Equation (3), summarized below.

Additional MHD modes to Alfvén modes—A recent work by Skalidis & Tassis (2021) suggests a new equation to estimate the magnetic field strength to take into account not only the Alfvén modes but also other additional magnetosonic compressive modes, which must be present in molecular clouds. This requires a modification of Equation (3) to $B_{\rm pos} = \sqrt{2\pi\rho}\,\frac{\sigma_{\rm turb}}{\sqrt{\sigma_{\rm PA}}}$. We applied this new equation using $\sigma_{\rm PA,gauss}$ (the dispersion from the approach yielding largest magnetic field strengths) and the average magnetic field in our sample decreased by a factor of 3 (from 1.8 to 0.6 mG) while μ increased by the same factor. The new values of $\mu_{\rm gauss}$ after applying this method are listed in the last column of Table 5 for comparison.

Deviation from equipartition—One of the basic assumptions of Equation (3) could be violated if the perturbed magnetic field with energy $E_{\delta\,\rm B}$ is not in equipartition with the turbulent kinetic energy, $E_{\rm turb}$. In this case, the magnetic field should be multiplied by a factor (equal to the square root of $E_{\delta B}/E_{\rm turb}$) ranging from 0.4 to 1 in the simulations of Heitsch et al. (2001) and μ could increase up to a factor of 2.5. There could also be

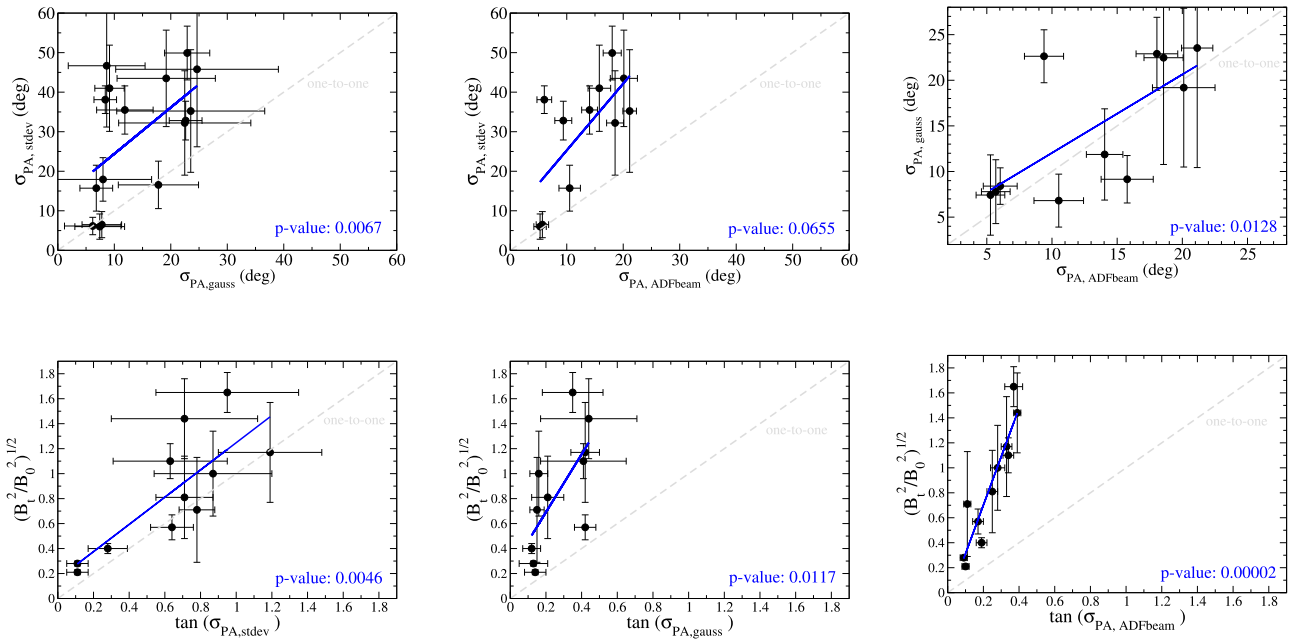

Figure 9. Comparison of the four different approaches used here to estimate $\delta B/B_0$ (Sections 4.3.1, 4.3.2, 4.4.1, and 4.4.2), with the results of the linear regression fits (blue line) and the p values (probability that the null hypothesis is true) listed in each panel. The gray dashed line indicates the one-to-one relation.

deviations from equipartition if the total kinetic energy of the gas, $E_{\rm kin}$, typically assumed to be equal to $E_{\rm turb}$, has a nonnegligible contribution from systematic motions such as inflow/infall motions, i.e., the gravitational energy is not negligible. This could easily be the case in our cores because bulk motions of gas flowing toward the center of massive dense cores have been observed (e.g., Csengeri et al. 2011; Lee et al. 2013; Battisti & Heyer 2014; Liu et al. 2015; Motte et al. 2018; Schwörer et al. 2019). Actually, the morphology of the magnetic field segments in several regions studied here suggests such kinds of motions (see, for example, the cases of W3IRS5, N6334V,W75N, DR21OH, N48, and N7538S in Figures 2(a) and (b)). In these cases, it would be required to separate not only the turbulent component of the magnetic field out of the large-scale uniform field but the systematic motions should also be separated from the line width to finally have the true turbulent kinetic energy $E_{\rm turb}$. Because in many cases it is assumed that $E_{\rm turb} \sim E_{\rm kin}$, there is an overestimation of the magnetic field strength and an underestimation of μ. In our case we used the $Q \equiv \sigma_{\rm turb}/\sigma_{\rm nonth}$ factor to take this into account. However, assuming the same Q factor for all regions might not be correct, and we further discuss this in Section 5.4. A comparison with simulations for one of our regions that presents converging flows (N6334V; Juárez et al. 2017) is given in Appendix G, showing that the "standard deviation" approach yields results comparable to those in the simulations.

Averaged quantities—Our measured magnetic field strengths and μ are averaged values: within the studied area, densities can change by orders of magnitudes and the magnetic field also scales with density to some power. However, while the density structure is much better resolved and the mass can be more accurately estimated, the DCF and ADF methods give statistically average values for the magnetic field strength for which uncertainties are not easy to quantify. Actually, in a recent paper by Añez-López et al. (2020a) it was found $\mu < 1$ in a star-forming massive core. But for the same core, the technique of Koch et al. (2012a) was applied to locally assess the force ratio between the magnetic field and gravity, revealing specific portions within the initially studied area that clearly were supercritical (while the average μ was below 1).

5.1.5. Comparison to Other Determinations of the Magnetic Field Strength in the Literature

A final way to test the robustness of our determination of the magnetic field strength is to compare it to other values reported in the literature, especially when completely independent methods are used, such as the "ion–neutral drift" technique. In Table 5, the magnetic field strengths obtained in other works in the literature are reported (see table notes of Table 5 for a reference to the different methods), and in Appendix H, more details are given about the comparison between the values determined here and the values obtained for the same regions in previous works.

Figure 17 of Appendix H shows a plot of the magnetic field strength reported in the literature and the strengths derived in this work. The figure reveals a relation quite close to a one-to-one relation. The cases of N6334I, N6334In, DR21OH, and N3 are particularly significant, as the methods used in the literature for these regions are independent of the method used here. This figure indicates that the method used here to infer the magnetic field strength seems to be reasonable.

5.1.6. Uncertainty in μ

In Table 5, μ has values very close to 1 or even < 1, especially for the "multiple Gaussians" and "ADF beam" approaches. This is kind of unexpected because all the cores in our sample are known to undergo active star formation and should thus be supercritical. However, our calculation of μ is obviously affected by all the aforementioned uncertainties associated with the calculation of the magnetic field strength, which in some cases would imply a factor of 2.5 or even 3 larger μ. In addition, the absolute value of the column density might also be affected by the fact of not taking into account the

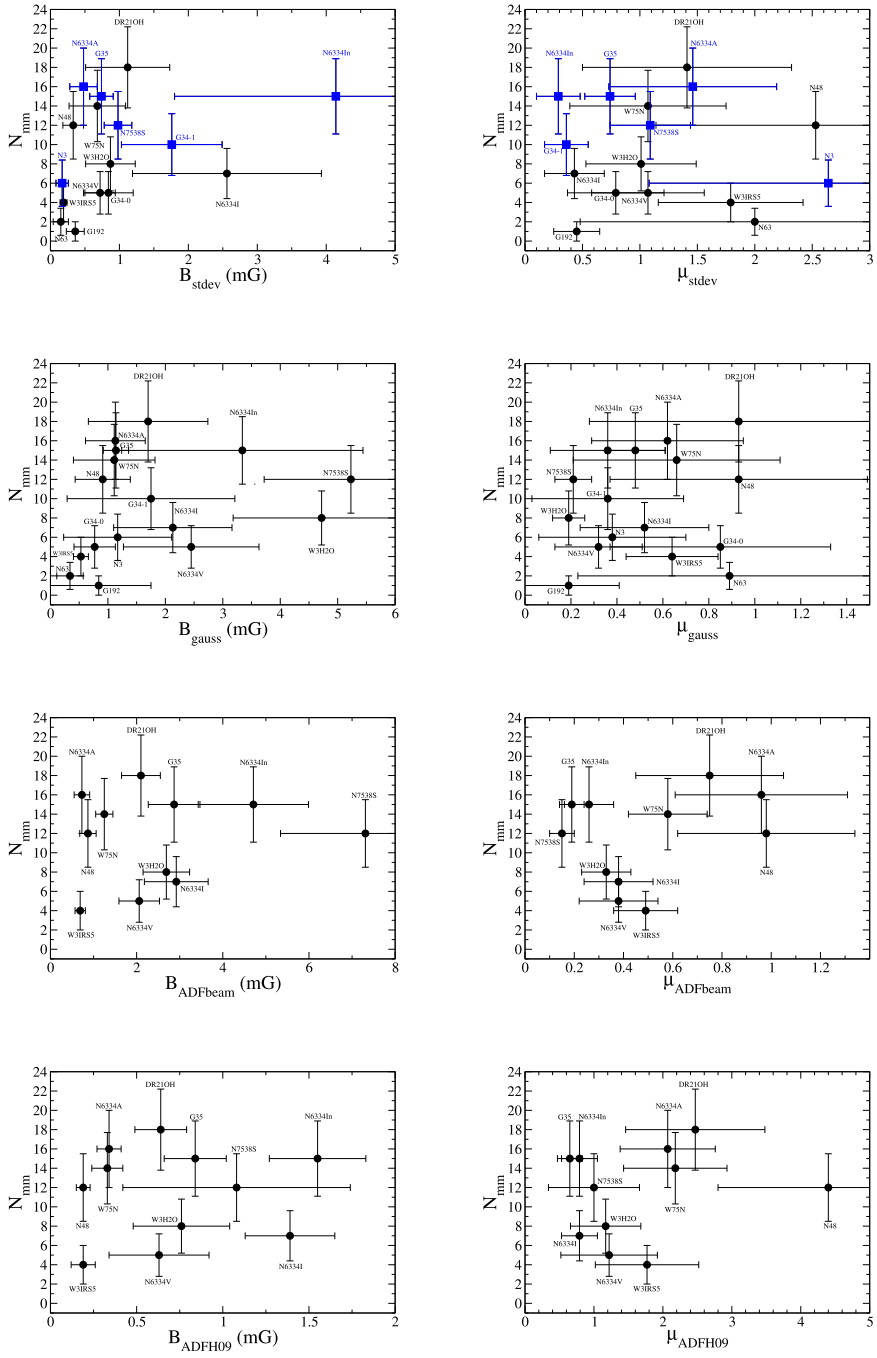

Figure 10. The four panels on the left show the plots of $N_{\rm mm}$ vs. the magnetic field strength for the different approaches used in this work: "standard deviation" ($B_{\rm stdev}$), "multiple Gaussian" ($B_{\rm gauss}$), "ADF beam" ($B_{\rm ADFbeam}$), and "ADF H09" ($B_{\rm ADFH09}$). The four panels on the right show the plots of $N_{\rm mm}$ vs. the ratio of mass-to-flux to critical mass-to-flux, μ, for the same four approaches. In the top panels, the blue squares correspond to the cores classified as presenting "aligned fragmentation" in Table 2.

mass already blocked in stars. The core masses within 0.15 pc in diameter, used to estimate the column density in Equation (14), range from 20 to 100 $M_\odot$ (Table 3). If half of this mass is considered to be in stars, this would imply an additional factor of 1.5 larger μ (see also Section 5.7 in Girart et al. 2013). Therefore, the absolute values of μ reported in Table 5 would be probably shifted to higher values if the aforementioned caveats could be quantified and taken into account. While providing accurate absolute values of μ is well beyond the scope of this paper, the relative values of μ between the regions of our sample should not be that strongly affected and are probably a good measure of this quantity.

Finally, it is worth noting that measuring μ smaller than 1 does not necessarily imply that the magnetic field is dominating over gravity because μ can actually depend on the spatial scale where it is measured (e.g., Koch et al. 2012b). For example, in Gómez et al. (2021; see Section 4.3), it is shown that if the density is a power law of the radius "r," and the magnetic field strength follows a power law of the density with index 2/3, then $\mu(r) \sim r^{1-p/3}$, where p is the density power-law index.

Thus, for the values of p reported in this work, which average to $p \sim 1.8$, $\mu(r) \sim r^{0.4}$, and thus μ should decrease for smaller radii. Such a decrease of μ for smaller radii has actually been measured by Crutcher et al. (2009), Tang et al. (2019), and Arzoumanian et al. (2021). In addition to this, there is still the fact that the superficial terms in the virial theorem have been ignored in the standard definition of μ, while these could yield up to a factor of 2 smaller critical masses and therefore a factor of 2 larger μ (Strittmatter 1966).

5.1.7. Summary of Uncertainties

In spite of all the caveats mentioned in this section, the crucial aspect of the analysis presented here is that it is performed uniformly for the entire sample, measuring each parameter using exactly the same method and within the same field of view for all the regions. For the validity of Equation (3), one of the most crucial aspects probably is the separation of the perturbed/turbulent component of the velocity dispersion, $\sigma_{\rm turb}$, and of the magnetic field, δB, from the ordered or large-scale component, B_0, and this can be specifically done using the ADF method (any of the two approaches presented in Section 4.4) as it allows to calculate the PA dispersion as a function of distance. The fact that $\sigma_{\rm PA,stdev}$ was found to correlate well with $\langle B_{\rm t}^2\rangle/\langle B_0^2\rangle$ (Figure 9) is indicative that this separation was successfully done in terms of relative variations of $\delta B/B_0$ in our sample.

Given the goal of our work, it is important to use $B_{\rm stdev}$ instead of $B_{\rm ADF}$ because $B_{\rm stdev}$ could be calculated for 16 regions while $B_{\rm ADF}$ was only calculated to 11 regions, and this allowed us to improve the statistics to test the $N_{\rm mm}$ versus $B_{\rm pos}$ or $N_{\rm mm}$ versus μ relations. Therefore, far from intending to provide accurate absolute values, our reported values of the magnetic field strength and μ should be useful to assess the relative variation of these quantities in this sample.

5.2. A Strong Correlation of Fragmentation Level with Density within 0.15 pc

In the top panel of Figure 11, we present a plot of the fragmentation level versus the density averaged within 0.15 pc. As can be seen from this plot, a correlation between the fragmentation level and the averaged density is apparent. Because we determined the density for a fixed size, such a relation with density is equivalent to a relation with mass. A linear regression fit gives a correlation coefficient of 0.71, while the Spearman's rank correlation coefficient ρ is 0.65 and the p value is 0.0035. The relation is consistent with previous observational studies (e.g., Gutermuth et al. 2011; Palau et al. 2014; Lee et al. 2015; Liu et al. 2016; Nguyen-Luong et al. 2016; Pokhrel et al. 2016, 2018, 2020; Mercimek et al. 2017; Alfaro & Román-Zúñiga 2018; Mendigutía et al. 2018; Murillo et al. 2018; Li et al. 2019; Lin et al. 2019; Orkisz et al. 2019; Sanhueza et al. 2019; Sokol et al. 2019; Svoboda et al. 2019; Zhang et al. 2019) and theoretical/numerical studies (Burkhart 2018; Guszejnov et al. 2018; Dobbs et al. 2019) reporting an important role of density in determining fragmentation of massive dense cores and is expected for the case of thermal Jeans fragmentation.

5.3. Interplay between Density and the Magnetic Field Strength

The lack of correlation between the fragmentation level and the magnetic field strength or μ could be due to the fact that our sample includes massive dense cores with too broad a range of densities. In other words, because density and magnetic field could both affect the fragmentation level simultaneously, we consider here whether a relation is found when only regions with very similar densities are considered. Looking at the top panel of Figure 11, the range (3–6) $\times 10^5$ cm^{-3} includes a large number of regions and could be good to perform the aforementioned test.

In the middle-left panel of Figure 11, we present a plot of $N_{\rm mm}$ versus $B_{\rm stdev}$, only for the regions within the narrow density range given above. In the bottom-left panel of the same figure, the plot of $N_{\rm mm}$ versus $\mu_{\rm stdev}$ is also shown. While statistically these samples are too small (implying p values larger than 0.09) and the uncertainties are high, a possible connection between $N_{\rm mm}$ and the magnetic field strength or μ cannot be ruled out. What we find here is in full agreement with a recent work toward the infrared dark cloud G14.225−0.506, where the two main hubs of the cloud have very similar densities, and their different fragmentation levels can be explained by the different measured magnetic field strengths (Añez-López et al. 2020a).

5.4. A Tentative Trend of Fragmentation Level with Mass-to-flux Ratio

In the measurements of $B_{\rm pos}$ and μ calculated so far, a constant factor $Q \sim 0.5$, was adopted. Q was defined in Section 4.2 as $Q \equiv \sigma_{\rm turb}/\sigma_{\rm nonth}$. However, in the same Section 4.2, the Q factor was also estimated from the VDFs for the same regions where the ADFs were calculated in Section 4.4.1. We consider here the fact that Q might actually vary from one region to the other (as shown in Table 4) and recalculated $B_{\rm pos}$ and μ for the "ADF beam" approach. We chose the "ADF beam" approach because this is the approach for which $\sigma_{\rm PA}$ is calculated with exactly the same technique as $\sigma_{\rm turb,VDF}$, taking the value of the dispersion function (structure function) at the smallest scales, both in velocity and polarization PA. By doing this, the effects of large-scale motions (e.g., due to gravity) should be avoided, and Equation (3) (DCF) should be fully valid.

In the right panels of Figure 11, we present the result for $N_{\rm mm}$ versus $B_{\rm pos}$ and μ following this technique, and the figure reveals a tentative trend for the case of $N_{\rm mm}$ versus μ, with a p value of ∼0.03, where $N_{\rm mm}$ increases for regions with larger μ, as expected from numerical simulations and theoretical work. According to this figure, the magnetic field in our sample seems to play a nonnegligible role in the determination of the fragmentation level of massive dense cores.

If confirmed with new more sensitive observations carried out in larger samples, our work would strongly indicate that, when the DCF method is applied (Equation (3)), it is crucial to properly separate the large-scale motions from the small-scale turbulent motions in the velocity dispersion, and that the velocity dispersions inferred from averaging spectra could have a nonnegligible part due to systematic motions. Thus, the common assumption made in the literature that the nonthermal velocity dispersions are due entirely to turbulence is not probably correct, at least in our sample.

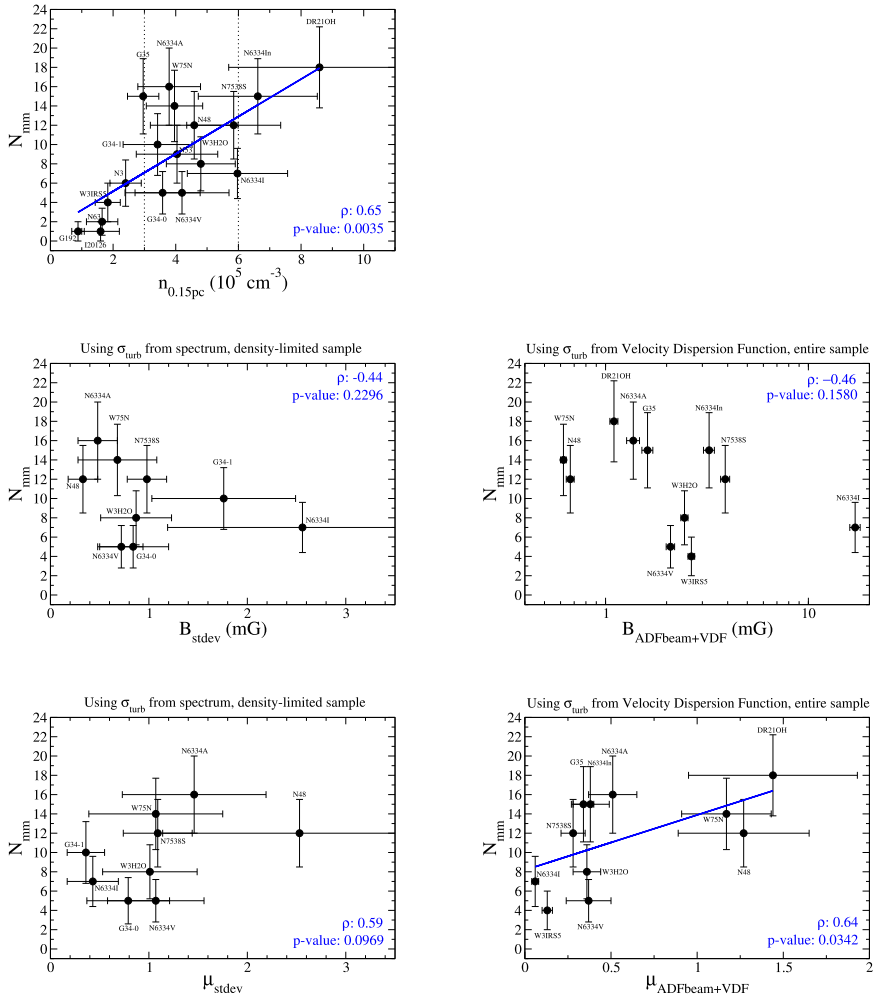

Figure 11. Top: fragmentation level vs. density averaged within the same field of view where fragmentation, line width, and PA dispersion were assessed (0.15 pc in diameter). The blue line indicates the result of a linear regression of the form $N_{\rm mm} = (1 \pm 2) + (1.9 \pm 0.5)\left[\frac{n_{0.15\ {\rm pc}}}{10^5\ {\rm cm}^{-3}}\right]$, with a correlation coefficient of 0.71. Middle left and bottom left: fragmentation level vs. $B_{\rm stdev}$ (middle) and vs. $\mu_{\rm stdev}$ (bottom) for regions with similar density (in the range (3–6) $\times$ 10^5 cm^{-3}, marked with vertical dotted lines in the top panel) and using the $\sigma_{\rm turb} = \sigma_{\rm turb,spec}$ calculated from a Gaussian fit to the $H^{13}CO^+$(4–3) spectrum following Equation (1). Middle right and bottom right: fragmentation level vs. $B_{\rm ADFbeam+VDF}$ (middle) and vs. $\mu_{\rm ADFbeam+VDF}$ (bottom) for all the regions in our sample where ADF was applied, and using $\sigma_{\rm turb} = \sigma_{\rm turb,VDF}$ calculated from the velocity dispersion function (column (5) of Table 4), thus separating in velocity the small-scale turbulent motions from the systematic large-scale motions. The blue line indicates the result of a linear regression of the form $N_{\rm mm} = (8 \pm 2) + (6 \pm 3)\mu_{\rm ADFbeam+VDF}$, with a correlation coefficient of 0.58. In all panels, the Spearman's rank correlation coefficient ρ and the p value are annotated in the bottom/top-right corner.

5.5. Comparison of Average Fragment Masses with Jeans and Magnetic Critical Masses

The fact that the $N_{\rm mm}$ versus $n_{0.15\ {\rm pc}}$ relation is stronger than the $N_{\rm mm}$ versus $B_{\rm stdev}$ relation suggests that thermal Jeans fragmentation has a nonnegligible role in the fragmentation of our sample. If this is the case, the mass of the fragments should be comparable to the Jeans mass. Using the density averaged within 0.15 pc reported in Table 3, we calculated the Jeans mass following Equation (6) of Palau et al. (2015):

$$\left[\frac{M_{\rm Jeans}}{M_\odot}\right] = 0.6285\left[\frac{T}{10\ {\rm K}}\right]^{3/2}\left[\frac{n_{\rm H_2}}{10^5\ {\rm cm}^{-3}}\right]^{-1/2}. \quad (15)$$

The values of the Jeans mass for each massive dense core, $M_{\rm Jeans}$, are reported in Table 2. The table gives a range of $M_{\rm Jeans}$ corresponding to the range of temperatures assumed, from 20 K (lower limit) to $T_{0.15\ {\rm pc}}$ (Table 3, upper limit). As can be seen from this table, $M_{\rm Jeans}$ is of the order of 1–5 $M_\odot$, very similar to the average mass of the fragments in each core.

In order to assess whether the measured magnetic field in each region is able to prevent the collapse of the detected fragments, the critical masses for magnetic support were calculated following Equation (16) of McKee & Ostriker (2007):

$$M_{\rm crit} \equiv c_\Phi \frac{\Phi_{\rm B}}{G^{1/2}}, \quad (16)$$

where G is the gravitational constant, $\Phi_{\rm B}$ is the magnetic field flux threading the core, and c_Φ is a numerical coefficient adopted as $c_\Phi = 1/2\pi$, which corresponds to the value for an infinite cold sheet and is nearly identical to the value for a core with a poloidal field and a constant mass-to-flux ratio (McKee & Ostriker 2007). The magnetic flux was calculated as $\Phi_{\rm B} = \pi R^2 B_{\rm pos}$, yielding the equation:

$$M_{\rm crit} = \frac{R^2 B_{\rm pos}}{2 G^{1/2}}. \quad (17)$$

In this equation, R was taken equal to $\langle R_{\rm fragm}\rangle$ (Table 2), and $B_{\rm pos}$ was estimated by scaling $B_{\rm stdev}$ (Table 5) in density to the

average density of all the fragments, of 3×10^7 cm^{-3} (Table 2), assuming that $B_{\rm frag} = B_{\rm stdev}\left[\frac{3 \times 10^7 \,{\rm cm}^{-3}}{n_{0.15\,{\rm pc}}}\right]^{0.4}$ (Li et al. 2015).

The resulting values of $M_{\rm crit}$ are listed in Table 2 and are within the range calculated for $M_{\rm Jeans}$. Therefore, in general, the fragments studied in our sample have enough masses to overcome both the thermal and the magnetic support.

5.6. Fragment Sizes versus Magnetic Field Strength

We explore here whether there is any relation between the sizes or masses of the fragments and the magnetic field strength of their parental core. Figure 12 presents a plot with the masses (top) and 3σ radii (bottom) for all 160 detected fragments versus the magnetic field strength. Both panels indicate that there could be an upper envelope with the more massive/largest fragments tending to occur where the magnetic field is weaker. In addition, the scatter in the masses and sizes of the fragments appears to decrease with growing field strength. For the largest field strength (corresponding to N6334In), the scatter appears to be very small (although statistics are not very large—see the standard deviations of the fragment sizes for each region in Table 2). Assuming that a fragment under a strong magnetic field is not accreting material from its surroundings as efficiently as a fragment under a weak magnetic field (because the magnetic field should slow the collapse down), the smaller sizes observed for regions with larger magnetic fields could indicate that the magnetic field is preventing these fragments from growing fast in both mass and size, consistent with theoretical work (e.g., Hennebelle & Inutsuka 2019).

In addition, two of the regions with the strongest magnetic field, N6334In and G34-1, have their fragments aligned along a prevailing direction, and as such, they were classified as undergoing "aligned fragmentation" in Table 2. This finding is fully consistent with the work of Fontani et al. (2018), who also report that a filamentary distribution of the fragments is favored for strong magnetic fields. For these cases, the magnetic field morphology is rather uniform and perpendicular to the axis of the aligned fragments. With such a geometry, and with a relatively strong magnetic field strength, the fragmentation process should happen along the field lines, with material moving more easily along the field lines from the outer regions toward a midplane. This could explain the relatively small scatter in size for such a configuration. Note that G35 also presents "aligned fragmentation," but has the magnetic field along the main axis of the filamentary structure, its magnetic field strength is relatively low, and it presents a large scatter in the fragment masses and sizes (Table 2), thus also fitting within this picture. In summary, the magnetic field strength, the small scatter in the sizes of the fragments, and the field morphology all suggest that the magnetic field in these cases is regulating at least partially the fragmentation process.

5.7. Implications of Our Results

As mentioned in the introduction, a number of theoretical and numerical studies suggest that magnetic fields could be crucial to determine the fragmentation level of molecular clumps and cores, because strong magnetic fields should suppress fragmentation. In a recent review about the role of magnetic fields in the formation of molecular clouds, Hennebelle & Inutsuka (2019) present the assumptions leading to ideal MHD equations, taking into account ion–neutral drift.

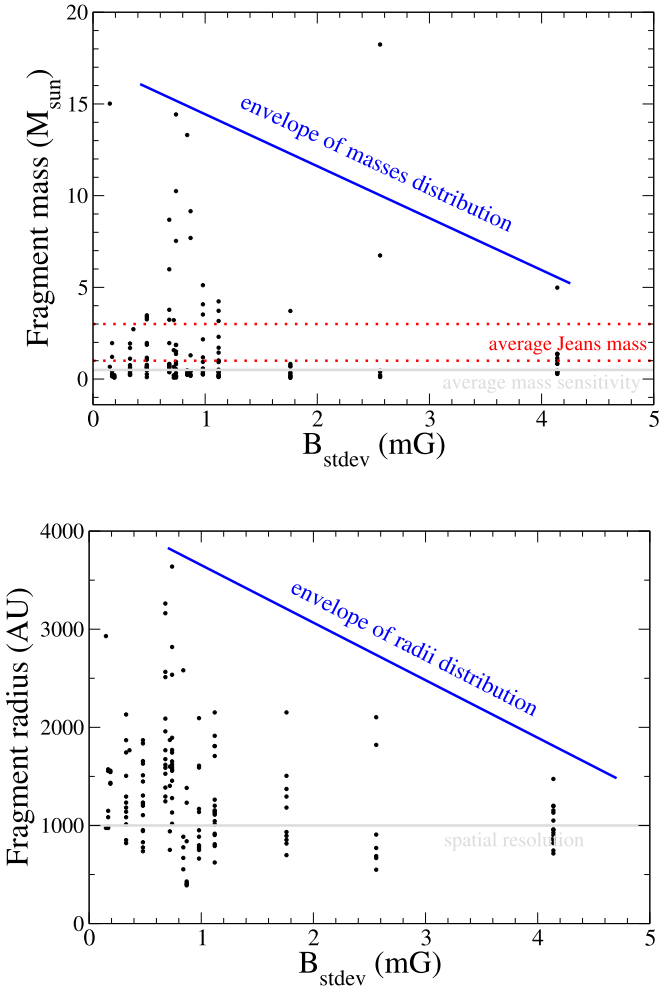

Figure 12. Top: masses of the fragments identified within each massive dense core vs. $B_{\rm stdev}$. The horizontal red dotted lines indicate the range of average $M_{\rm Jeans}$ found for our sample assuming $T = 20$ K and $T = T_{0.15\ {\rm pc}}$ (Table 2). The horizontal gray line indicates the typical mass sensitivity of our observations (Table 1). Bottom: radii (at the 3σ contour) of the fragments identified within each massive dense core vs. $B_{\rm stdev}$. The horizontal gray line indicates the typical spatial resolution of our observations (Table 1). Oblique lines are drawn to guide the eye.

They consider the influence that the magnetic field may have on the interstellar filaments and the molecular clouds, and its role on the formation of stellar clusters. They argue that the magnetic field could be responsible for reducing the star formation rate and the numbers of clumps, cores and stars.

In this paper, we aimed at testing this from direct observations. From our uniform analysis of the entire sample of 18 massive dense cores at ∼0.15 pc scales, a correlation between fragmentation level and density (within 0.15 pc) is clear from our analysis (Section 5.2 and Figure 11), indicating that the fragmentation process in our sample is mainly dominated by gravity. This is consistent with very recent numerical simulations from Krumholz & Federrath (2019), who find that the magnetic field strength should not strongly affect the star formation rate or initial mass function in star-forming clouds at their earliest stages of formation.

The lack of a strong correlation of the fragmentation level with the magnetic field strength or μ could arise from the decoupling (diffusion) of the magnetic field at the scales studied in this work. However, this is difficult to assess because there is little work in the literature reporting signs of diffusion

on the scales and densities studied in this work. On one hand, Yen et al. (2018) looked at the ion–neutral drift velocity in the B335 Class 0 protostar which should result from ambipolar diffusion. Although these authors concentrated on much smaller scales (100 au) and higher densities than the ones studied in this work, where ambipolar diffusion is supposed to be efficient (Tassis & Mouschovias 2007), no clear drift velocity was detected, suggesting that the magnetic field is still well coupled to the gas even on these small and dense scales. On the other hand, for the case of DR21OH, Girart et al. (2013, Section 5.5) suggest that magnetic flux diffusion or dissipation is taking place at the scales studied here via fast magnetic reconnection in the presence of turbulence (Lazarian & Vishniac 1999; Santos-Lima et al. 2010). Clearly this needs to be further explored.

It is worth mentioning that the magnetic field strengths inferred in this work cover a range of about one order of magnitude (from 0.2 to 4 mG, or μ from 0.3 to 2.5) and are also subject to a number of uncertainties (see Section 5.1), while simulations showing very different fragmentation levels correspond to setups differing by two orders of magnitude in μ (e.g., from 2 to 130; Commerçon et al. 2011; Hennebelle et al. 2011). This suggests that the typical magnetic fields in the massive dense cores of our sample probably do not cover a sufficiently large range to leave a clear trace on the fragmentation level and that this is rather determined by other environmental factors such as density.

However, finer details of our observational data set seem to be consistent with the magnetic field affecting the fragmentation process at least partially. First, when large-scale systematic motions are separated from the velocity dispersion and only the small-scale (turbulent) contribution is taken into account, a tentative correlation is found between $N_{\rm mm}$ and the mass-to-flux ratio, as expected theoretically and numerically. This could explain the significant scatter found in the $N_{\rm mm}$ versus density relation. Second, regions with strongest magnetic field (N6334In and G34-1) undergo fragmentation along a preferential direction, which is perpendicular to the magnetic field lines. Third, regions with strong magnetic fields are also the regions with small fragments and with almost all fragments with similar sizes. These three findings suggest that the magnetic field, at least in these cases, is somehow affecting the fragmentation process. It is therefore necessary to test this in a larger sample to strengthen the hints found here.

6. Conclusions

We have compiled a sample of 18 massive dense cores for which submillimeter polarization observations from the Legacy Program of the SMA (Zhang et al. 2014), as well as submillimeter continuum images at high angular resolution were available. The sample was built to strictly fulfill constraints of spatial resolution of $\sim$1000 au and mass sensitivities (from the submillimeter continuum) around $\sim$0.5 $M_\odot$, so that a fragmentation level can be measured in a uniform and reliable way (and within the same field of view of 0.15 pc) for all cores. The polarization images were analyzed to infer polarization PA dispersions using four different approaches. In addition, $H^{13}CO^+$(4–3) data from the SMA observations were used to infer velocity dispersions for each core. Finally, the temperature and density structure were modeled for each massive dense core using submillimeter continuum emission from single-dish telescopes and the spectral energy distribution, following Palau et al. (2014). All of the quantities were measured in a uniform way and within the same field of view of 0.15 pc. The aforementioned inferred properties of the massive dense cores allowed us to calculate magnetic field strengths using the DCF and ADF methods, and search for possible trends between the fragmentation level and any of the derived properties of the parental cores. Our main conclusions can be summarized as follows:

1. A total of 160 fragments have been identified within the 18 massive dense cores. We have assigned a fragmentation level within a field of view of 0.15 pc, $N_{\rm mm}$, to each massive dense core. We found a variety of fragmentation levels, with 17% of the cores presenting almost no fragmentation, and 39% of the cores presenting a high fragmentation level. Additionally, cores were classified according to their fragmentation type, mainly "aligned fragmentation" (seven cores), "clustered fragmentation" (eight cores), and "no fragmentation" (three cores).
2. The inferred power-law indices for the density of the massive dense cores range from 1.46 to 2.26. The densities, masses, and temperatures, all (averaged) within 0.15 pc, range from 1.1 to 10.5 $\times$ 10^5 cm^{-3}, from 11 to 105 $M_\odot$, and from 23 to 120 K, respectively.
3. The line widths of the $H^{13}CO^+$(4–3) transition measured in each core range from 1.3 to 6.7 km s^{-1}, and no clear trend was found between $N_{\rm mm}$ and these line widths.
4. Four approaches were used to estimate polarization PA dispersions. First, the PA dispersion was estimated from the standard deviation of the PA corrected for the PA uncertainties. Second, different Gaussians were fitted to the PA histograms. Additionally, the ADF analysis was performed following Houde et al. (2009), and the PA dispersion was estimated from the smallest value (beam scale) of the ADF. It was found that the PA dispersion, inferred from the standard deviation, correlates with the corresponding quantity from the ADF analysis, and the first one was used as a reference to calculate the magnetic field strengths. In combination with the line widths and average densities, this yielded magnetic field strengths ranging from 0.2 to 4.1 mG.
5. When considering the entire sample, a strong correlation of $N_{\rm mm}$ with density averaged within 0.15 pc is found although with significant scatter. In addition, $N_{\rm mm}$ seems to tentatively correlate with the mass-to-flux ratio, once the large-scale systematic motions are properly separated from the velocity dispersion in the magnetic field strength calculation. These findings clearly need to be studied in larger and more sensitive samples.
6. The separation of the large-scale systematic motions from the small-scale (turbulent) motions was performed through the analysis of the VDF, allowing us to calculate that the turbulent velocity dispersion is typically 40% of the nonthermal velocity dispersion.
7. The sizes and masses of each fragment were measured. The average masses of the fragments ranged from 2 to 4 $M_\odot$ in most cases, comparable to the thermal Jeans mass. Regarding the sizes of the fragments, hints of more compact and less massive fragments for stronger magnetic fields were found, suggesting that in the cases of strong magnetic fields, this might slow down the accretion process compared to the nonmagnetic case. In addition, for the strong magnetic field cases,

fragmentation seems to take place along a preferred direction perpendicularly to the magnetic field.

In summary, our entire sample of massive dense cores presents a strong correlation of the fragmentation level with the density of the parental core and a tentative trend of the fragmentation level with the mass-to-flux ratio. In addition, hints were found of the magnetic field influencing the fragmentation process (size and mass of the fragments) for the cores with strongest magnetic fields. Overall, the observed properties of our sample are consistent with thermal Jeans fragmentation, and the magnetic field seems to act as a modulating process required to explain the finer details of the fragmenting cores.

The authors are deeply grateful to the anonymous referee, whose insightful comments have undoubtedly improved the quality of this paper. A.P. is grateful to Javier Ballesteros-Paredes, Raphael Skalidis, Konstantinos Tassis, and Enrique Vázquez-Semadeni for stimulating and thoughtful discussions; to Manuel Zamora-Avilés for calculating the magnetic field strength within a region 0.15 pc in diameter in the simulations of Juárez et al. (2017) of N6334V; and to Daniel J. Díaz González for his support with Python. A.P. acknowledges financial support from CONACyT and UNAM-PAPIIT IN113119 grant, México. J.M.G. and R.E. are supported by the Spanish grant AYA2017-84390-C2-R (AEI/FEDER, UE). J.L. and K.Q. are supported by the National Key R&D Program of China No. 2017YFA0402600. J.L. and K.Q. acknowledge the support from National Natural Science Foundation of China (NSFC) through grants U1731237, 11590781 and 11629302. P.M.K. acknowledges support from Ministry of Science and Technology (MoST) grants MOST 108-2112-M-001-012 and MOST 109-2112-M-001-022 in Taiwan, and from an Academia Sinica Career Development Award. H.B.L. is supported by the Ministry of Science and Technology (MoST) of Taiwan (grant Nos. 108-2112-M-001-002-MY3). Z.Y.L. is supported in part by NSF AST-1716259 and 1815784. L.A.Z. is grateful to CONACyT, México, and DGAPA, UNAM for their financial support. H.B. acknowledges support from the European Research Council under the European Community's Horizon 2020 framework program (2014–2020) via the ERC Consolidator Grant "From Cloud to Star Formation (CSF)" (project number 648505). H.B. also acknowledges funding from the Deutsche Forschungsgemeinschaft (DFG) via the Collaborative Research Center (SFB 881) "The Milky Way System" (subproject B1).

Part of the data used in this paper were obtained in the SMA legacy project: Filaments, Magnetic Fields, and Massive Star Formation (PI: Qizhou Zhang). This research made use of Astropy,[26] a community-developed core Python package for Astronomy (Astropy Collaboration et al. 2013; Astropy Collaboration et al. 2018), and in particular, numpy (van der Walt et al. 2011). The Karma software was used for part of the analysis of this paper (Gooch 1996).

Facilities: SMA, PdBI, NOEMA, JCMT(SCUBA).

Software: astropy (Astropy Collaboration et al. 2013), GILDAS, Karma.

Appendix A
Tests for Biases of the Fragmentation Level $N_{\rm mm}$

Figure 13 presents the plots of $N_{\rm mm}$ (Section 3) versus the mass sensitivity, column density sensitivity, the evolutionary indicator $L_{\rm bol}/M_{\rm core}$ (Molinari et al. 2016), and the spatial resolution for each region (Table 1). If $N_{\rm mm}$ were biased with the mass sensitivity or the spatial resolution, one would expect a large $N_{\rm mm}$ for smaller (better) mass sensitivities, and a large $N_{\rm mm}$ for smaller (better) spatial resolutions. As can be seen from the figure, none of the relations is appreciable for $N_{\rm mm}$ with any of the tested quantities.

[26] http://www.astropy.org

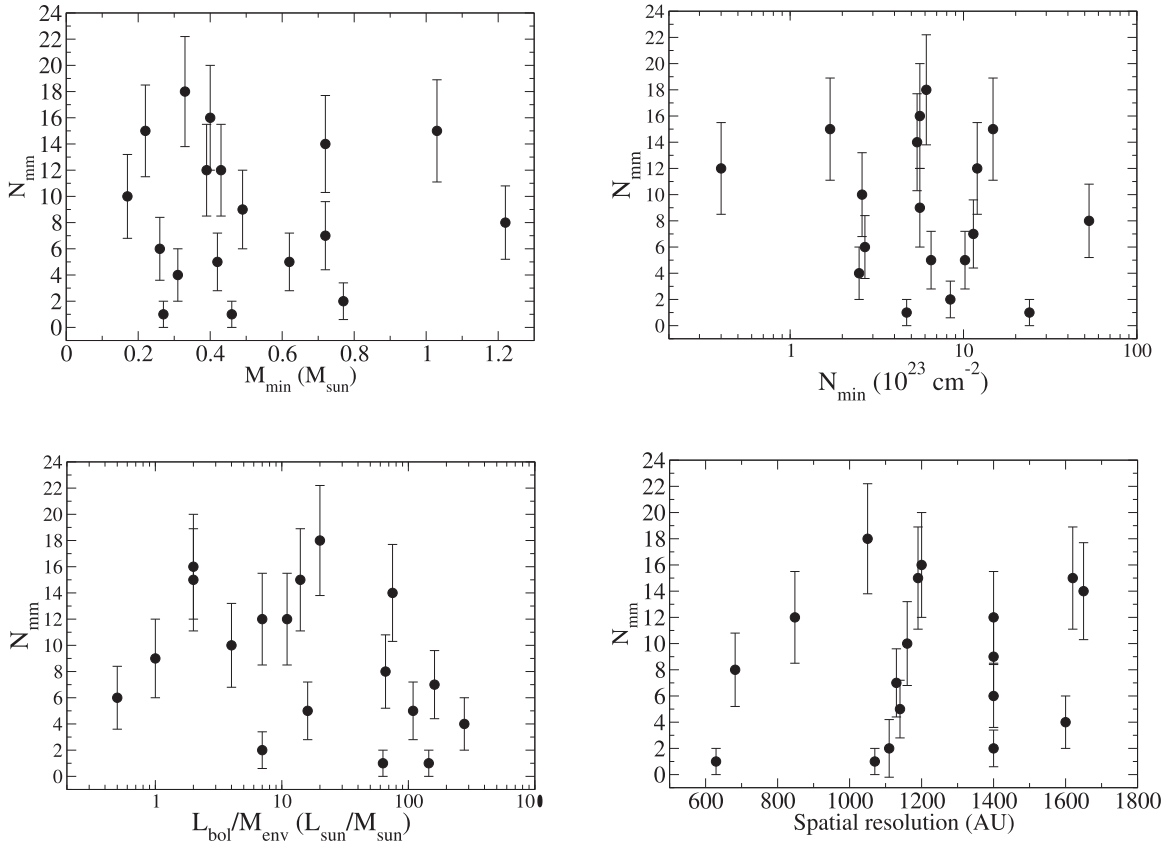

Figure 13. Top left: fragmentation level $N_{\rm mm}$ vs. mass sensitivity for each massive dense core of our sample. Top right: fragmentation level $N_{\rm mm}$ vs. column density sensitivity (calculated from the mass sensitivity and the beam of our observations). Bottom left: fragmentation level $N_{\rm mm}$ vs. $L_{\rm bol}/M_{\rm core}$. Bottom right: fragmentation level $N_{\rm mm}$ vs. spatial resolution. These figures show that there are no biases of $N_{\rm mm}$ with respect to any of these observational parameters.

Appendix B
First-order Moments for $H^{13}CO^{+}$(4–3) Data

Figures 14(a) and (b) show the first-order moments of the $H^{13}CO^{+}$(4–3) transition in color scale, with the magnetic field segments overplotted as well as arrows for the known outflows in each core (taken from the literature).

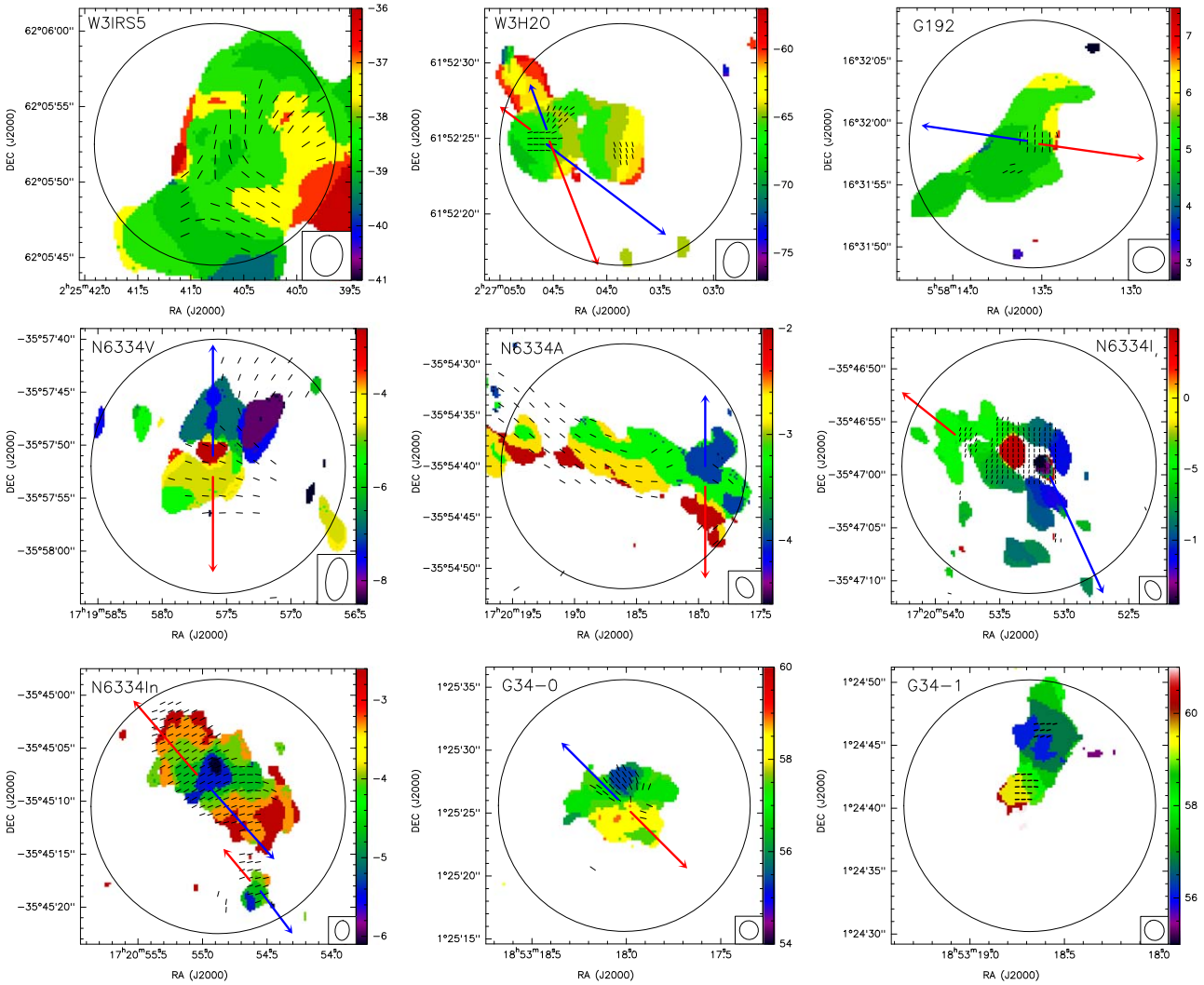

Figure 14. (a) First-order moments for $H^{13}CO^{+}$(4–3) data with the magnetic field segments (black) overplotted. Red and blue arrows indicate the approximate orientations of the redshifted and blueshifted outflow emission according to Zapata et al. (2011) and Zhang et al. (2014). The synthesized beam is shown in the bottom-right corner. The circle corresponds to the field of view 0.15 pc in diameter used in this work to assess the magnetic field strength. Wedge units are km s^{-1}. (b) First-order moments for $H^{13}CO^{+}$(4–3) data with the magnetic field segments (black) overplotted. Red and blue arrows indicate the approximate orientations of the redshifted and blueshifted outflow emission according to Naranjo-Romero et al. (2012), Duarte-Cabral et al. (2013, 2014), Girart et al. (2013), and Zhang et al. (2014). The synthesized beam is shown in the bottom-right corner. The circle corresponds to the field of view 0.15 pc in diameter used in this work to assess the magnetic field strength. Wedge units are km s^{-1}.

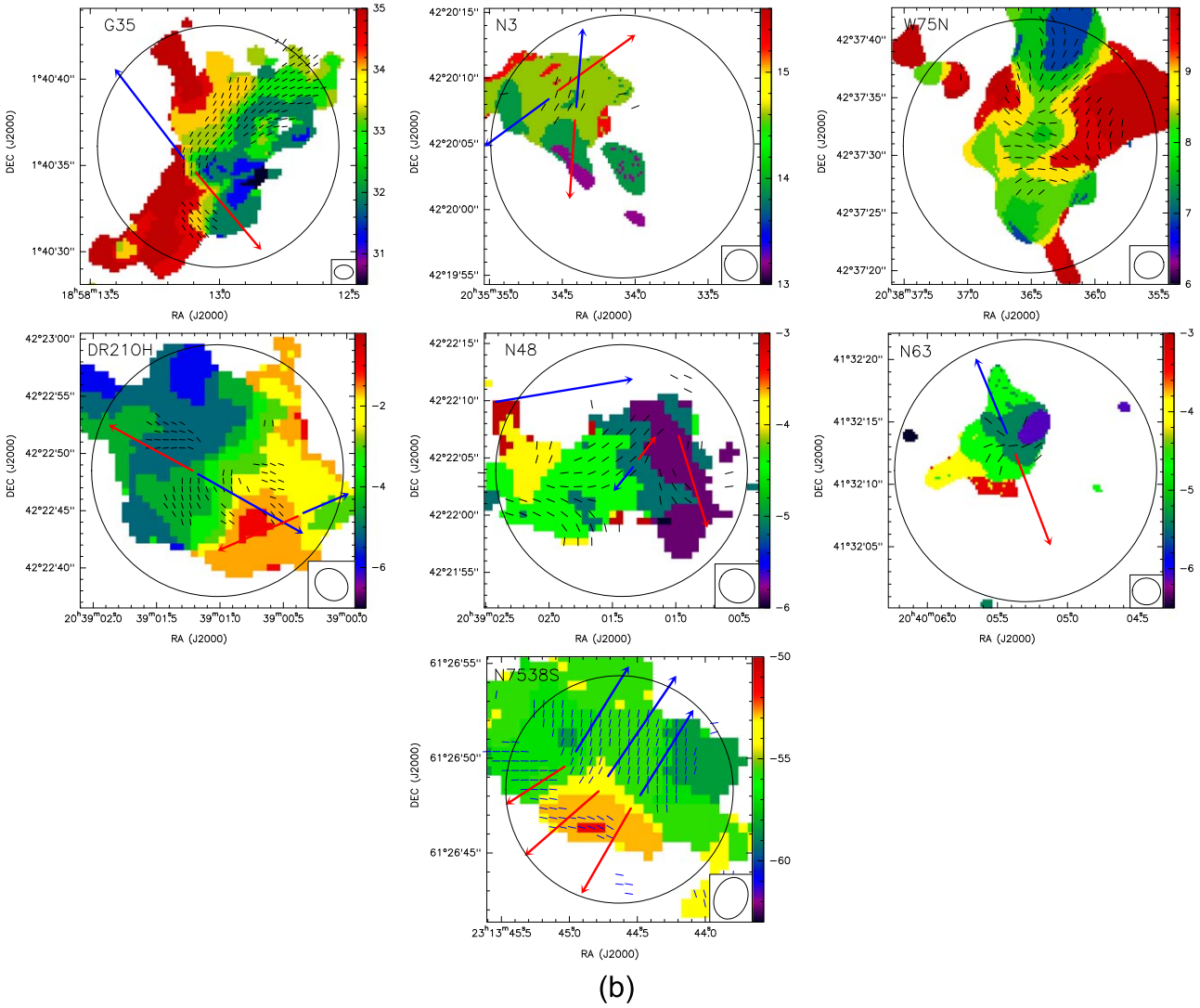

(b)

Figure 14. (Continued.)

Appendix C
Particular Cases in the Density and Temperature Structure Modeling of Section 4.1

In Section 4.1, a density and temperature structure model was fit to observational data for each region of our sample. The observational data consisted of radial intensity profiles and the spectral energy distribution, and the model allowed us to infer an average density within 0.15 pc for each region. We comment here on the particularities of some of the sources to perform the fit.

W3H2O—The model includes an optically thin radio source of 2.5 Jy at 30 GHz (Dreher & Welch 1981).

N6334A—The assumption of the core being centrally heated might not be fulfilled because there is a Herschel core (core number 38 from Tigé et al. 2017) that only lies about $\sim 13''$ from the SCUBA peak at 450 μm and for which the flux density at 70 μm is a factor of $\sim$20 larger than the flux at 70 μm for the core directly associated with the 450 μm peak. In this case, we did several tests to fit the model. First, to build the SED, we considered only the Herschel intensities associated with core number 41 (core associated with the 450 μm peak). This yielded an average density within 0.15 pc of 4.8×10^5 cm^{-3}. This should be a reasonable approach as long as we are considering only peak intensities of the core directly associated with the SCUBA peak, and the excess due to heating by core 38 (and 10) should not be strong because its effect should be only in specific directions compared to the entire radially averaged profile. Second, we considered only the contribution of core 41 and used peak intensities to build the SED, except for Herschel wavelengths where the beam cannot separate the different sources (i.e., 250, 350, and 500 μm, where the beam is $> 12''$). For these wavelengths, we included in the SED the flux density of all three cores and used the core size as the aperture radius for the model to compute the flux. This method yielded an average density within 0.15 pc of 3.8×10^5 cm^{-3}, and in Table 3 and Figure 11, we use the fitted values corresponding to this second method, to be conservative.

G35—The IRAS flux at 100 μm is a factor of 3 smaller than the Herschel-PACS measurements at 70 and 160 μm. We calculated the model including both Herschel and IRAS fluxes (best-fit values reported in Table 3, yielding an average density within 0.15 pc of 2.96×10^5 cm^{-3}).

Appendix D
Uncertainty Estimates Running Monte Carlo Simulations

One of the main uncertainties associated with the derivation of the magnetic field strength or μ from polarized submillimeter emission is the sparse sampling of the data. In order to have a first estimate of these uncertainties, Monte Carlo simulations were run as described in the appendix of Liu et al. (2019). For each region, we modeled the large-scale field as a parabola of the form $y = g + g\,C\,x^2$, with C being the curvature parameter set as $C = \sigma_{\rm PA,stdev}/3000$. A random dispersion equal to twice the average error in PA of each region was introduced. This was run 10 times for each region. In each run, two PA maps were produced: the unbiased (fully sampled) PA map and the sparsely sampled map specific to each region. Then, for each run and for each unbiased/sparsely sampled map, we applied our four approaches used in the analysis to estimate the PA dispersions (Sections 4.3.1, 4.3.2, 4.4.1, and 4.4.2) and measured the difference in the dispersion between the unbiased and the sparsely sampled images. This gave us an idea of how far the measured dispersion might be from the unbiased "real" dispersion. We then averaged these differences for the 10 runs (for each approach) and took this average difference as the uncertainty in each case. The uncertainties in dispersion were propagated to the magnetic field strength and mass-to-flux ratio. In general, we obtained larger uncertainties for the poorly sampled regions, as expected.

Appendix E
Magnetic Field Strength versus Density

In Figure 15, we present a plot of the magnetic field strength as calculated in Section 4.3.1, $B_{\rm stdev}$ (Table 5), versus density averaged within 0.15 pc in diameter (Table 3). The log–log plot shows a trend, with a slope of 1.1 ± 0.3.

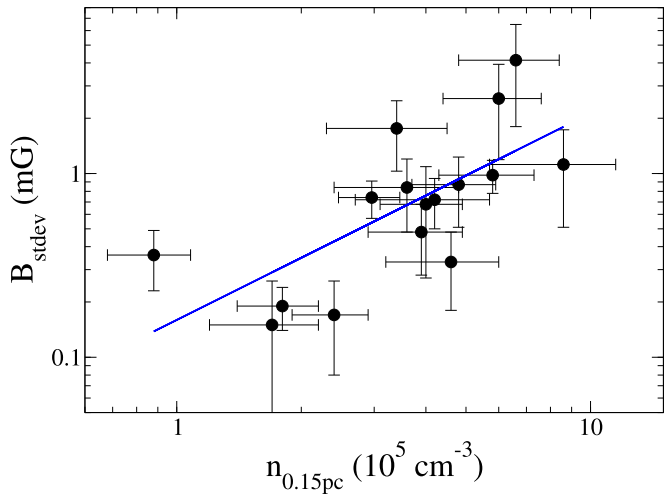

Figure 15. Magnetic field strength calculated with the "standard deviation" approach, $B_{\rm stdev}$, vs. density averaged within 0.15 pc. The blue line corresponds to a linear fit in logarithmic scales with a slope of 1.1 ± 0.3 and a correlation coefficient of 0.69.

Appendix F
Comparison of SMA and Single-dish Densities

In Section 4.1, the density structure for each massive dense core was inferred using data from single-dish telescopes, mainly the James Clerk Maxwell Telescope (with main beams of 19.″5 at 850 μm and 11.″0 at 450 μm) and the IRAM 30 m telescope (with a main beam of 11.″0 at 1.2 mm). From this model, the average density within 0.15 pc was derived. In order to assess if the different spatial filtering of the single-dish telescopes and the SMA is affecting our determination of the density and the magnetic field strength, we compare here how the inferred densities in Section 4.1 compare to the densities inferred using the SMA data.

The average density (within 0.15 pc in diameter) was estimated using the SMA continuum flux densities, including all of the configurations available as for the case of the $H^{13}CO^+$ and PA data. This includes in many cases the subcompact configuration and in all cases the compact configuration of the SMA. These configurations allow us to recover angular scales as large as 30″ and 14″, respectively (following the appendix of Palau et al. 2010). Therefore, using these SMA data, we are sensitive to scales comparable to the scales of the single-dish telescopes.

To infer the masses and densities from the SMA data, we measured the flux density within the region of 0.15 pc in diameter, and assumed the average temperature within the same diameter inferred from our modeling (given in Table 3), as well as the opacity law of Ossenkopf & Henning (1994) (grains covered by thin ice mantles at 10^6 cm^{-3}, 0.0175 cm^2 per gram of gas and dust at 870 μm). Figure 16 presents the relation between the SMA average density (within 0.15 pc in diameter) versus the average density inferred using the modeling of the single-dish data presented in Section 4.1. As can be seen from the figure, by doing this, we recover with the SMA ~75% of

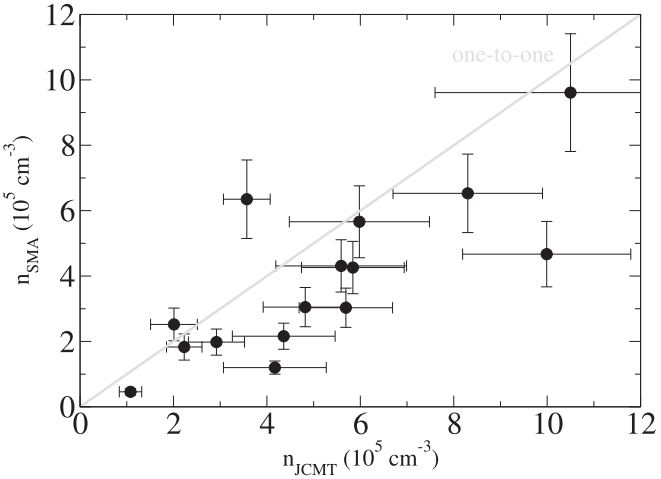

Figure 16. Plot of the SMA average density (within 0.15 pc in diameter) vs. the average density inferred using the modeling of the single-dish data presented in Section 4.1. The light gray line indicates the one-to-one relation to guide the eye. To make the comparison, we converted the densities reported in Table 3, $n_{0.15\ \rm pc}$, from the density of H_2 particles to the total density of particles. The uncertainties for the SMA average density have been adopted to be 20%, the typical uncertainty in the flux absolute scale.

the mass inferred from the modeling of the single-dish data presented in Section 4.1.

Appendix G
Comparison of Magnetic Field Strength Inferred from the Simulations of a Globally Collapsing and Hierarchical Cloud and One of the Cores Studied Here

We compared the magnetic field strength inferred in simulations dominated by gravity with the measured strength from observations for the particular case of N6334V, where simulations of a collapsing magnetized molecular cloud were specifically tuned to explain the magnetic field and dynamics of the region (Juárez et al. 2017). In these simulations, the gas flows from the large scales toward the center of the massive dense cores, and the magnetic field is dragged by the gas. The magnetic field in the simulations was measured within 0.15 pc of the massive dense core and a value of 0.94 mG was found (M. Zamora-Avilés 2021, private communication), very similar to the values obtained here for N6334V using the "standard deviation" or "ADF H09" approaches, of 0.6–0.7 mG, and only a factor of 2 smaller than the values obtained with the "multiple Gaussians" or "ADF beam" approaches. Thus, for the particular case of N6334V, the magnetic field measured in the simulations is very comparable to the magnetic field inferred in our work.

Appendix H
Comparison of Magnetic Field Strength Inferred in This Work and the Magnetic Field Strength in Other Works of the Literature

Here we provide details, for each region, of previous works reporting magnetic field strengths in regions of our sample.

DR21OH, N3, N53—Hezareh et al. (2010, 2013) estimated the magnetic field in the DR21 region, including DR21OH, N3, and N53, by comparing the velocity dispersions of ion and neutral pairs at different length scales and find values in the range 0.33–1.8 mG (for densities very similar to the ones we obtained here).

NGC 6334—Li et al. (2015) present evidence that magnetic fields regulate the dynamics in NGC 6334, based on their findings of hourglass-shaped field lines at gas column density peaks and from the fact that the field strength is found to be proportional to the 0.4-power of the density. They infer the magnetic field strength by assuming force equilibrium between gravity, magnetic tension, and magnetic pressure at different scales, and derive a relation between magnetic field strength and density. The value given in Table 5 for the magnetic field strength in N6334I and N6334In is the one corresponding to the density given in Table 3 and applies the aforementioned relation between field strength and density.

G34—Tang et al. (2019) report submillimeter polarization observations using the Caltech Submillimeter Observatory and infer the magnetic field strength using the "ADF beam" approach for both G34-0 and G34-1 (Table 5; Tang et al. 2019 report densities of 1.6×10^5 cm^{-3} for these two cores).

W3H2O—Chen et al. (2012a) estimate the magnetic field strength using the DCF method with a density of 1.5×10^7 cm^{-3} and obtained 17 mG. To compare this value to our measurement, we scaled the magnetic field strength assuming a dependence with density as a power law with index 0.4 (Li et al. 2015) and used our estimate for the density reported in Table 3, obtaining a value of 4.6 mG.

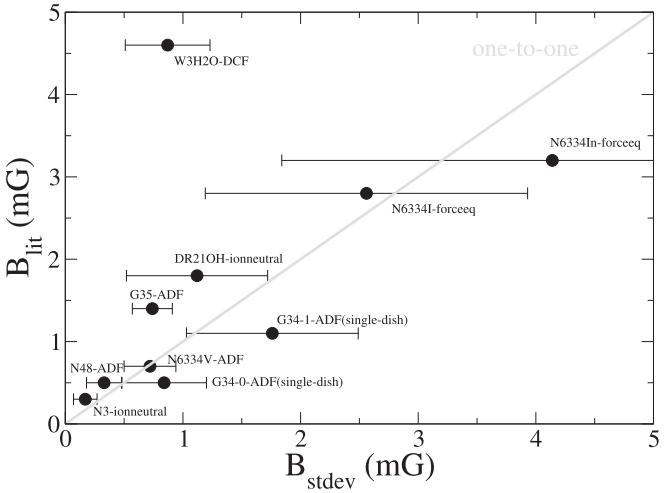

Figure 17. Comparison of the magnetic field determined in the literature and the magnetic field determined in this work using the "standard deviation" approach, $B_{\rm stdev}$. The light gray line corresponds to the one-to-one relation to guide the eye. Next to the name of each source, there is a short name for the method used to determine the magnetic field strength. See Table 5 for further details.

G35—Qiu et al. (2013) report a value of the magnetic field strength of 0.9–1.4 using the same SMA data set used in this work and the "ADF H09" method.

I20126—This region has been observed with the SMA in submillimeter polarization but no sufficient detections were found to estimate a reliable PA dispersion (H. Shinnaga et al. 2021, in preparation). However, Edris et al. (2005) perform estimates of the magnetic field at scales of ∼1000 au through Zeeman splitting of OH masers and obtain 11 mG within 0.″5. Assuming that the density at ∼1000 au is around 8.4×10^{-17} g cm^{-3} (Table 3), we estimate a magnetic field strength of 1.8 mG for the density we have calculated within 0.15 pc.

Figure 17 presents a plot comparing the magnetic field strength reported in the literature with the magnetic field strength derived in this work for the "standard deviation" approach.

ORCID iDs

Aina Palau https://orcid.org/0000-0002-9569-9234
Qizhou Zhang https://orcid.org/0000-0003-2384-6589
Josep M. Girart https://orcid.org/0000-0002-3829-5591
Junhao Liu https://orcid.org/0000-0002-4774-2998
Patrick M. Koch https://orcid.org/0000-0003-2777-5861
Robert Estalella https://orcid.org/0000-0001-7341-8641
Huei-Ru Vivien Chen https://orcid.org/0000-0002-9774-1846
Keping Qiu https://orcid.org/0000-0002-5093-5088
Luis A. Zapata https://orcid.org/0000-0003-2343-7937
Henrik Beuther https://orcid.org/0000-0002-1700-090X
Hiroko Shinnaga https://orcid.org/0000-0001-9407-6775

References

Adams, F. C. 1991, ApJ, 382, 544
Ahmadi, A., Beuther, H., Mottram, J. C., et al. 2018, A&A, 618, A46
Alfaro, E. J., & Román-Zúñiga, C. G. 2018, MNRAS, 478, L110
Añez-López, N., Busquet, G., Koch, P. M., et al. 2020a, A&A, 644, A52
Añez-López, N., Osorio, M., Busquet, G., et al. 2020b, ApJ, 888, 41
Arzoumanian, D., Furuya, R., Hasegawa, T., et al. 2021, A&A, 647, A78
Astropy Collaboration, Robitaille, T. P., Tollerud, E. J., et al. 2013, A&A, 558, A33

Astropy Collaboration, Price-Whelan, A. M., Sipőcz, B. M., et al. 2018, AJ, 156, 123
Bailey, N. D., & Basu, S. 2012, ApJ, 761, 67
Battisti, A. J., & Heyer, M. H. 2014, ApJ, 780, 173
Beuther, H., Linz, H., & Henning, Th. 2012, A&A, 543, A88
Beuther, H., Mottram, J. C., Ahmadi, A., et al. 2018, A&A, 617, A100
Beuther, H., Soler, J. D., Linz, H., et al. 2020, ApJ, 904, 168
Bontemps, S., Motte, F., Csengeri, T., & Schneider, N. 2010, A&A, 524, A18
Boss, A. P. 1999, ApJ, 520, 744
Boss, A. P. 2004, MNRAS, 350, L57
Boss, A. P., & Bodenheimer, P. 1979, ApJ, 234, 289
Boss, A. P., & Keiser, S. A. 2013, ApJ, 764, 136
Boss, A. P., & Keiser, S. A. 2014, ApJ, 794, 44
Burkert, A., Bate, M. R., & Bodenheimer, P. 1997, MNRAS, 289, 497
Burkhart, B. 2018, ApJ, 863, 118
Busquet, G., Estalella, R., Palau, A., et al. 2016, ApJ, 819, 139
Cesaroni, R., Galli, D., Neri, R., et al. 2014, A&A, 566, A73
Chandler, C. J., Barsony, M., & Moore, T. J. T. 1998, MNRAS, 299, 789
Chandrasekhar, S., & Fermi, E. 1953, ApJ, 118, 113
Chen, H. H.-H., Pineda, J. E., Offner, S. S. R., et al. 2019, ApJ, 886, 119
Chen, H.-R., Rao, R., Wilner, D. J., & Liu, S.-Y. 2012a, ApJL, 751, L13
Chen, X., Arce, H. G., Dunham, M. M., & Zhang, Q. 2012b, ApJL, 747, L43
Ching, T.-C., Lai, S.-P., Zhang, Q., et al. 2017, ApJ, 838, 121
Commerçon, B., Hennebelle, P., & Henning, T. 2011, ApJL, 742, L9
Cortes, P. C., Girart, J. M., Hull, C. L. H., et al. 2016, ApJL, 825, L15
Cortes, P. C., Hull, C. L. H., Girart, J. M., et al. 2019, ApJ, 884, 48
Crutcher, R. M., Hakobian, N., & Troland, T. H. 2009, ApJ, 692, 844
Crutcher, R. M., Nutter, D. J., Ward-Thompson, D., et al. 2004, ApJ, 600, 279
Csengeri, T., Bontemps, S., Schneider, N., et al. 2011, ApJL, 740, L5
Cunningham, A. J., Krumholz, M. R., McKee, C. F., et al. 2018, MNRAS, 476, 771
Davis, L. 1951, PhRv, 81, 890
Di Francesco, J., Johnstone, D., Kirk, H., MacKenzie, T., & Ledwosinska, E. 2008, ApJS, 175, 277
Dobbs, C. L., Rosolowsky, E., Pettitt, A. R., et al. 2019, MNRAS, 485, 4997
Dreher, J. W., & Welch, W. J. 1981, ApJ, 245, 857
Duarte-Cabral, A., Bontemps, S., Motte, F., et al. 2013, A&A, 558, A125
Duarte-Cabral, A., Bontemps, S., Motte, F., et al. 2014, A&A, 570, A1
Edris, K. A., Fuller, G. A., Cohen, R. J., et al. 2005, A&A, 434, 213
Falceta-Gonçalves, D., Lazarian, A., & Kowal, G. 2008, ApJ, 679, 537
Federrath, C., Klessen, R. S., & Schmidt, W. 2008, ApJL, 688, L79
Fontani, F., Commerçon, B., Giannetti, A., et al. 2016, A&A, 593, L14
Fontani, F., Commerçon, B., Giannetti, A., et al. 2018, A&A, 615, A94
Forgan, D., & Rice, K. 2012, MNRAS, 420, 299
Franco, G. A. P., Alves, F. O., & Girart, J. M. 2010, ApJ, 723, 146
Galametz, M., Maury, A., Girart, J. M., et al. 2018, A&A, 616, A139
Galametz, M., Maury, A., Girart, J. M., et al. 2020, A&A, 644, A47
Gieser, C., Beuther, H., & Semenov, D. 2021, A&A, 648, A66
Girart, J. M., Frau, P., Zhang, Q., et al. 2013, ApJ, 772, 69
Girichidis, P., Federrath, C., Banerjee, R., & Klessen, R. S. 2011, MNRAS, 413, 2741
Girichidis, P., Seifried, D., Naab, T., et al. 2018, MNRAS, 480, 3511
Gómez, G. C., Vázquez-Semadeni, E., & Palau, A. 2021, MNRAS, 502, 4963
Gooch, R. 1996, in ASP Conf. Ser. 101, Astronomical Data Analysis Softwareand Systems V, ed. G. H. Jacoby & J. Barnes (Tucson, AZ: ASP), 80
Guerrero-Gamboa, R., & Vázquez-Semadeni, E. 2020, ApJ, 903, 136
Guszejnov, D., Hopkins, P. F., Grudić, M. Y., et al. 2018, MNRAS, 480, 182
Gutermuth, R. A., Pipher, J. L., Megeath, S. T., et al. 2011, ApJ, 739, 84
Heitsch, F., Zweibel, E. G., Mac Low, M.-M., et al. 2001, ApJ, 561, 800
Hennebelle, P., Commerçon, B., Joos, M., et al. 2011, A&A, 528, A72
Hennebelle, P., & Inutsuka, S.-. i. 2019, FrASS, 6, 5
Hennebelle, P., Whitworth, A. P., Cha, S.-H., et al. 2004, MNRAS, 348, 687
Hezareh, T., Houde, M., McCoey, C., et al. 2010, ApJ, 720, 603
Hezareh, T., Wiesemeyer, H., Houde, M., et al. 2013, A&A, 558, A45
Hildebrand, R. H., Kirby, L., Dotson, J. L., et al. 2009, ApJ, 696, 567
Houde, M., Rao, R., Vaillancourt, J. E., et al. 2011, ApJ, 733, 109
Houde, M., Vaillancourt, J. E., Hildebrand, R. H., et al. 2009, ApJ, 706, 1504
Juárez, C., Girart, J. M., Zamora-Avilés, M., et al. 2017, ApJ, 844, 44
Keto, E., Field, G. B., & Blackman, E. G. 2020, MNRAS, 492, 5870
Koch, P. M., Tang, Y.-W., & Ho, P. T. P. 2010, ApJ, 721, 815
Koch, P. M., Tang, Y.-W., & Ho, P. T. P. 2012a, ApJ, 747, 79
Koch, P. M., Tang, Y.-W., & Ho, P. T. P. 2012b, ApJ, 747, 80
Krumholz, M. R., & Federrath, C. 2019, FrASS, 6, 7
Lazarian, A., & Vishniac, E. T. 1999, ApJ, 517, 700
Lee, K., Looney, L. W., Schnee, S., et al. 2013, ApJ, 772, 100
Lee, K. I., Dunham, M. M., Myers, P. C., et al. 2015, ApJ, 814, 114
Li, H.-B., Yuen, K. H., Otto, F., et al. 2015, Natur, 520, 518
Li, J., Myers, P. C., Kirk, H., et al. 2019, ApJ, 871, 163
Lin, Y., Csengeri, T., Wyrowski, F., et al. 2019, A&A, 631, A72
Liu, H. B., Galván-Madrid, R., Jiménez-Serra, I., et al. 2015, ApJ, 804, 37
Liu, H. B., Qiu, K., Zhang, Q., et al. 2013, ApJ, 771, 71
Liu, J., Qiu, K., Berry, D., et al. 2019, ApJ, 877, 43
Liu, J., Zhang, Q., Qiu, K., et al. 2020, ApJ, 895, 142
Liu, T., Kim, K.-T., Yoo, H., et al. 2016, ApJ, 829, 59
Machida, M. N., Matsumoto, T., Hanawa, T., et al. 2005, MNRAS, 362, 382
Maury, A. J., André, P., Hennebelle, P., et al. 2010, A&A, 512, A40
McKee, C. F., & Ostriker, E. C. 2007, ARA&A, 45, 565
Mendigutía, I., Lada, C. J., & Oudmaijer, R. D. 2018, A&A, 618, A119
Mercimek, S., Myers, P. C., Lee, K. I., et al. 2017, AJ, 153, 214
Molinari, S., Merello, M., Elia, D., et al. 2016, ApJL, 826, L8
Motte, F., Bontemps, S., & Louvet, F. 2018, ARA&A, 56, 41
Motte, F., Bontemps, S., Schilke, P., et al. 2007, A&A, 476, 1243
Murillo, N. M., van Dishoeck, E. F., Tobin, J. J., et al. 2018, A&A, 620, A30
Myers, A. T., McKee, C. F., Cunningham, A. J., et al. 2013, ApJ, 766, 97
Myhill, E. A., & Kaula, W. M. 1992, ApJ, 386, 578
Naranjo-Romero, R., Zapata, L. A., Vázquez-Semadeni, E., et al. 2012, ApJ, 757, 58
Nguyen-Luong, Q., Nguyen, H. V. V., Motte, F., et al. 2016, ApJ, 833, 23
Orkisz, J. H., Peretto, N., Pety, J., et al. 2019, A&A, 624, A113
Ossenkopf, V., & Henning, T. 1994, A&A, 291, 943
Ostriker, E. C., Stone, J. M., & Gammie, C. F. 2001, ApJ, 546, 980
Padoan, P., & Nordlund, Å. 2002, ApJ, 576, 870
Palau, A., Ballesteros-Paredes, J., Vázquez-Semadeni, E., et al. 2015, MNRAS, 453, 3785
Palau, A., Sánchez-Monge, Á., Busquet, G., et al. 2010, A&A, 510, A5
Palau, A., Estalella, R., Girart, J. M., et al. 2014, ApJ, 785, 42
Palau, A., Fuente, A., Girart, J. M., et al. 2013, ApJ, 762, 120
Peretto, N., Hennebelle, P., & André, P. 2007, A&A, 464, 983
Peters, T., Banerjee, R., Klessen, R. S., et al. 2011, ApJ, 729, 72
Pillai, T., Kauffmann, J., Tan, J. C., et al. 2015, ApJ, 799, 74
Pillai, T. G. S., Clemens, D. P., Reissl, S., et al. 2020, NatAs, 4, 1195
Pokhrel, R., Gutermuth, R., Ali, B., et al. 2016, MNRAS, 461, 22
Pokhrel, R., Gutermuth, R. A., & Betti, S. K. 2020, ApJ, 896, 60
Pokhrel, R., Myers, P. C., Dunham, M. M., et al. 2018, ApJ, 853, 5
Price, D. J., & Bate, M. R. 2007, MNRAS, 377, 77
Qiu, K., Zhang, Q., Menten, K. M., et al. 2013, ApJ, 779, 182
Sanhueza, P., Contreras, Y., Wu, B., et al. 2019, ApJ, 886, 102
Santos, F. P., Busquet, G., Franco, G. A. P., et al. 2016, ApJ, 832, 186
Santos-Lima, R., Lazarian, A., de Gouveia Dal Pino, E. M., et al. 2010, ApJ, 714, 442
Schmeja, S., & Klessen, R. S. 2004, A&A, 419, 405
Schwörer, A., Sánchez-Monge, Á., Schilke, P., et al. 2019, A&A, 628, A6
Scoville, N. Z., & Kwan, J. 1976, ApJ, 206, 718
Skalidis, R., & Tassis, K. 2021, A&A, 647, A186
Sokol, A. D., Gutermuth, R. A., Pokhrel, R., et al. 2019, MNRAS, 483, 407
Strittmatter, P. A. 1966, MNRAS, 132, 359
Svoboda, B. E., Shirley, Y. L., Traficante, A., et al. 2019, ApJ, 886, 36
Tang, Y.-W., Koch, P. M., Peretto, N., et al. 2019, ApJ, 878, 10
Tassis, K., & Mouschovias, T. C. 2007, ApJ, 660, 388
Tigé, J., Motte, F., Russeil, D., et al. 2017, A&A, 602, A77
van der Walt, S., Colbert, S. C., & Varoquaux, G. 2011, CSE, 13, 22
Vázquez-Semadeni, E., Banerjee, R., Gómez, G. C., et al. 2011, MNRAS, 414, 2511
Vázquez-Semadeni, E., Kim, J., & Ballesteros-Paredes, J. 2005, ApJL, 630, L49
Vázquez-Semadeni, E., Passot, T., & Pouquet, A. 1996, ApJ, 473, 881
Wang, J.-W., Koch, P. M., Galván-Madrid, R., et al. 2020, ApJ, 905, 158
Williams, J. P., Blitz, L., & McKee, C. F. 2000, in Protostars and Planets IV, ed. V. Mannings, A. P. Boss, & S. S. Russell (Tucson, AZ: Univ. Arizona Press), 97
Yen, H.-W., Zhao, B., Koch, P. M., et al. 2018, A&A, 615, A58
Zapata, L. A., Rodrı´guez-Garza, C., Rodrı´guez, L. F., Girart, J. M., & Chen, H.-R. 2011, ApJL, 740, L19
Zhang, M., Kainulainen, J., Mattern, M., et al. 2019, A&A, 622, A52
Zhang, Q., Hunter, T. R., & Sridharan, T. K. 1998, ApJL, 505, L151
Zhang, Q., Hunter, T. R., Sridharan, T. K., et al. 2002, ApJ, 566, 982
Zhang, Q., Qiu, K., Girart, J. M., et al. 2014, ApJ, 792, 116
Zhang, Q., Wang, K., Lu, X., et al. 2015, ApJ, 804, 141
Zhang, Q., Wang, Y., Pillai, T., & Rathborne, J. 2009, ApJ, 696, 268
Ziegler, U. 2005, A&A, 435, 385